STUDY OF DIPION PRODUCTION IN THE REACTION $\pi^- p \to \pi^0 \pi^0 n$ BETWEEN 1.6 AND 2.4 GeV/c

Andris Skuja
(Ph. D. Thesis)

February 25, 1972

AEC Contract No. W-7405-eng-48

LBL-378

DISCLAIMER

Contents

STUDY OF DIPION PRODUCTION IN THE REACTION $\pi^- p \rightarrow \pi^o \pi^o n$ BETWEEN 1.6 AND 2.4 GeV/c

Andris Skuja

Feb 25, 1972

Lawrence Berkeley Laboratory
University of California
Berkeley, California

ABSTRACT

An experiment was performed at the Berkeley Bevatron to study the $I = 0$, $J = 0$ π-π system in the reaction $\pi^- p \rightarrow n\pi^o\pi^o$, at beam momenta of 1.60 to 2.40 GeV/c in 0.20-GeV/c intervals. The reaction occurred in a 20-cm liquid hydrogen target and the final state was identified by detecting the neutron and the γ-rays from the π^o decays. The detection system consisted of (a) a large cubic array of lead-plate optical spark chambers surrounding the target for converting γ-rays and (b) a set of 20 plastic-scintillator neutron counters to measure time-of-flight and direction from the target, in the polar-lab-angle region of 12 to 72 degrees. The spark chambers were seven to eight radiation lengths thick and covered five sides of a cube, with the sixth side (beam entrance face) being nearly closed by lead-scintillator sandwich gamma counters. A sample of 5000 four-gamma events was obtained that passed the kinematic fit to the hypothesis $\pi^- p \rightarrow \pi^o\pi^o n$ with a 1% confidence level.

The total cross-sections for the production of $\pi^- p \rightarrow \pi^o\pi^o n$ at each incident momentum were obtained. The dipion production distribution was parametrized using a modified one pion exchange model with form factors, and the off-mass-shell $\pi\pi$ scattering matrix element extracted. It was found that the $\pi^o\pi^o$ production distribution was more peripheral than the OPE model predictions and that above 850 MeV of the dipion mass, the matrix element varied rapidly, indicating a rapid variation of the

$I = 0$, $J = 0$, phase shift in this region.

It was also found that at low t, the reaction had substantial Δ^0 production (~ 50%).

I. INTRODUCTION

The existence of a resonant π-π interaction was postulated by various physicists before 1960, to explain a number of effects in the then known scattering data. Takeda,[1] to explain the total cross-section in πp scattering for both the isospin 3/2 and 1/2 case, predicted a resonant amplitude for $I(J^P) = 1(1^-)$ at a mass of ~ 600 MeV and a width of ~ 100 MeV in the π-π system. A similar resonant state was predicted by Frazer and Fulco[2] to enable them to fit the known electron-nucleon scattering data. In addition, Nambu,[3] to explain the electromagnetic form factor of the nucleon, postulated an I = 0 resonant amplitude in the π-π system. The subsequent study of the π-π system, in production reactions of the type $\pi N \rightarrow \pi\pi N$ by a number of experimenters[4] revealed a large enhancement in the π-π invariant mass at 760 MeV. That this resonance, named the ρ meson, had three charged states, and no others, implied that it had isospin quantum number I = 1. Additional investigation revealed that indeed the ρ had the expected quantum numbers $J^P = 1^-$. Further resonances in the π-π system were also discovered at higher energies [e.g., the f(1260) meson $I(J^P) = 0(1^+)$][5].

A more detailed examination of the π-π angular distributions in the region of the ρ meson showed that noticeable asymmetries existed in the decay distribution of the $\pi^+\pi^-$ dipion, as the distributions were examined as a function of the π-π invariant mass. The asymmetry was attributed to the interference of the ρ with an I = 0, $J^P = 0^+$ resonance (often called the epsilon or sigma) of about the same mass as the ρ. Subsequent detailed examination of the π-π system, in the $\pi^+\pi^-$ mode (using mainly bubble chamber techniques) yielded data that was interpreted to be evidence for a resonance around the ρ mass, but the results were ambiguous and inconsistent.[6]

An extensive examination of the $\pi^o\pi^o$ state followed (in the reaction $\pi^- p \rightarrow \pi^o\pi^o n$)[7] in which the epsilon (or sigma) should have been seen unambiguously, since the $\pi^o\pi^o$ system, because of Bose statistics, cannot have amplitudes for which **I** = 1. Thus the ρ cannot be observed in this reaction, which simplifies the analysis considerably. In addition for invariant masses below 1 GeV, it has been assumed that only s-wave angular momentum amplitudes contribute significantly, so that the $J^P = 0^+$ state is well isolated (this last conjecture is not well founded, and indeed d-wave amplitudes may contribute to the $\pi^o\pi^o$ system). The resulting data of the various experimental investigations, however, were not conclusive, and, in addition, were somewhat contradictory.

To try to resolve these difficulties, an experiment was conducted at the Bevatron at the Lawrence Berkeley Laboratory, to study the reaction $\pi^- p \rightarrow \pi^o\pi^o n$ with high resolution and good statistics. In the course of this study a parametrization of the $\pi^o\pi^o$ final state was obtained.

A. Phenomenology of Dipion Production

1. π-π Scattering Amplitudes

Measurement of the S-matrix in formation experiments resulting from π-π scattering are of great interest in testing theoretical models of scattering of elementary particles. Because of the lack of complication introduced by spin or unequal masses, the parametrization of the scattering is especially simple. Assuming charge independence, we can write all the π-π scattering amplitudes, $A(\pi\pi \to \pi\pi)$, as linear combinations of three invariant amplitudes, $f^I(s,\theta)$, $I = 0, 1, 2$, where s is the square of the center of mass (c.m.) energy, θ, the scattering angle, and I, the isotopic spin.

$$A(\pi^+\pi^+ \to \pi^+\pi^+) = f^2(s, \theta)$$

$$A(\pi^+\pi^- \to \pi^+\pi^-) = \frac{1}{6}\left\{f^2(s, \theta) + 3f^1(s, \theta) + 2f^o(s, \theta)\right\}$$

$$A(\pi^\pm\pi^o \to \pi^\pm\pi^o) = \frac{1}{2}\left\{f^2(s, \theta) + f^1(s, \theta)\right\}$$

$$A(\pi^+\pi^- \to \pi^o\pi^o) = \frac{1}{3}\left\{f^2(s, \theta) - f^o(s, \theta)\right\}$$

The differential cross-section is then given in terms of these amplitudes by the expression

$$\frac{d\sigma}{d\Omega}(\pi\pi \to \pi\pi) = \frac{1}{K^2}\left|A(\pi\pi \to \pi\pi)\right|^2$$

In the $\pi\pi$ c.m. system each of the invariant amplitudes can be expanded in the usual partial wave decomposition

$$f^I(s, \theta) = \sum_{\ell=0}^{\infty}(2\ell + 1)P_\ell(\cos\theta)e^{i\delta_\ell^I(s)}\sin\delta_\ell^I(s)\left[1 + (-1)^{I+\ell}\right]$$

where δ_ℓ^I are the phase shifts for the ℓth angular momentum partial wave in the expansion of the amplitude f^I of isospin I. If we keep only s and p waves ($\ell = 0$, $\ell = 1$) as is usual for c.m. energies of the π-π system below 1 GeV, we obtain for the differential cross-sections

$$\frac{d\sigma}{d\Omega}(\pi^+\pi^+ \to \pi^+\pi^+) = \frac{4}{K^2}\sin^2\delta_0^2 \tag{1}$$

$$\frac{d\sigma}{d\Omega}(\pi^\pm\pi^0 \to \pi^\pm\pi^0) = \frac{1}{K^2}(F_1 + F_2\cos\theta + F_3\cos^2\theta) \tag{2}$$

$$F_1 = \sin^2\delta_0^2 \tag{2.1}$$

$$F_2 = 6\cos(\delta_0^2 - \delta_1^1)\sin^2\delta_0^2\sin\delta_1^1 \tag{2.2}$$

$$F_3 = 9\sin^2\delta_1^1 \tag{2.3}$$

$$\frac{d\sigma}{d\Omega}(\pi^+\pi^- \to \pi^+\pi^-) = \frac{1}{K^2}(D_1 + D_2\cos\theta + D_3\cos^2\theta) \tag{3}$$

$$D_1 = \frac{4}{9}\sin^2\delta_0^0 + \frac{1}{9}\sin^2\delta_0^2 + \frac{4}{9}\cos(\delta_0^0 - \delta_0^2)\sin\delta_0^0\sin\delta_0^2 \tag{3.1}$$

$$D_2 = 4\cos(\delta_0^0 - \delta_1^1)\sin\delta_0^0\sin\delta_1^1 + 2\cos(\delta_0^2 - \delta_1^1)\sin\delta_0^2\sin\delta_1^1 \tag{3.2}$$

$$D_3 = 9\sin^2\delta_1^1 \tag{3.3}$$

$$\frac{d\sigma}{d\Omega}(\pi^+\pi^- \to \pi^0\pi^0) = \frac{1}{K^2}\frac{4}{9}\sin^2(\delta_0^2 - \delta_0^0) \tag{4}$$

It should be noted that $\pi^+\pi^+$ elastic scattering [Eq. (1)] can be represented by a pure I = 2 state, while all the other amplitudes are a superposition of various isotopic spin states. The $\pi^+\pi^-$ elastic scattering amplitude [Eq. (3)] is a superposition of all three isotopic spin states, I = 0, 1, 2; $\pi^\pm\pi^0$ elastic scattering [Eq. (2)] is represented by a superposition of I = 1 and I = 2 states; while $\pi^+\pi^-$ charge exchange [Eq. (4)] is a superposition of I = 0 and I = 2 states.

Up to the present, pion targets of sufficient density to perform meaningful s-channel scattering experiments have not been constructed. Consequently, information on $\pi\pi$ scattering, and in particular the

resonance structure of the π-π system, must be obtained by other means.

2. Parametrization of Dipion Production

Much of our knowledge of π-π interactions is derived from production experiments of the form

$$\pi N \rightarrow \pi\pi N'$$

$$\pi N \rightarrow \pi\pi\pi N'$$

$$\pi d \rightarrow \pi\pi NN'$$

We consider only the first of these reactions and define the following variables (assuming charge independence):

p, p' = four momenta of the initial and final state nucleons

q = four momentum of the initial state pion

q', q'' = four momenta of the final state pions

$w = (p' + q' + q'')^2 = (p + q)^2$

$s = (q' + q'')^2$

$t = (p' - p)^2$

where w, s, and t are Lorentz invariants, while the frame or frames in which the momenta are to be measured will be specified as we proceed. Of course, in forming the invariants all momenta should be measured in the same frame. If we represent the masses of the baryons and the pions by M and μ respectively, we obtain in the overall c.m.

$$\cos\Theta = \frac{w^2 + 2w(t - \mu^2 - M^2) + (M^2 - \mu^2)(M^2 - s)}{\left[\left|w - \left|M + \sqrt{s}\right|^2\right|\left|w - \left|M - \sqrt{s}\right|^2\right|\left|w - \left|M + \mu\right|^2\right|\left|w - \left|M - \mu\right|^2\right|\right]^{1/2}}$$

where Θ is the dipion production angle. It should be noted that Θ is a function of w, t, and s.

The amplitude for the three body final state can be parameterized in terms of s-channel helicity amplitudes.[8]

$$A(\pi N \rightarrow \pi\pi N) = \sum_{j\ell\lambda\lambda'} (2j + 1) \langle \ell\lambda\lambda'' | T^j | \lambda' \rangle \times d^j_{-\lambda', \lambda - \lambda''}(\Theta)\, d^{\ell}_{\lambda 0}(\theta')\, e^{i\lambda\phi'} \qquad (5)$$

In this representation Θ is the production angle of the dipion system in the three body c.m. frame, while θ', ϕ' are the decay angles of the dipion system measured in the dipion rest frame with respect to an axis of quantization parallel to the direction of the dipion momentum in the three body c.m. system. The quantities λ' and λ'' are the helicities of the initial and final nucleon states, while λ is the helicity of the dipion system, all with respect to the beam direction. The symbol ℓ is the relative angular momentum of the two pions, while j is the relative angular momentum of the neutron-dipion system.

To express this amplitude so that the axis of quantization for the decay products of the dipion system lies parallel to the momentum of the initial pion, a rotation must be performed. We obtain

$$d^{\ell}_{\lambda o}(\theta')e^{i\lambda\phi'} = \sum_{m} d^{\ell}_{\lambda m}(-\beta(\Theta))d^{\ell}_{mo}(\theta)e^{im\phi}$$

where β is the production angle as measured in the dipion rest frame. It is preferable to express the amplitudes in terms of the rotated variables, since in the dipion rest frame the incident π^- momentum is equal and opposite to the momentum transfer three-vector, $(\underset{\sim}{p} - \underset{\sim}{p}')$, making the incident beam direction a convenient axis of quantization. This, in turn, will allow us later to express the three body amplitudes in terms of amplitudes which may be identified (taking into accounte certain assumptions) with π-π scattering amplitudes. We then have

$$A(\pi N \to \pi\pi N) = \sum_{j\ell\lambda\lambda' m} (2j + 1)\langle \ell\lambda\lambda'' | T^{j} | \lambda' \rangle \times d^{j}_{-\lambda', \lambda-\lambda''}(\Theta) d^{\ell}_{\lambda m}(-\beta)\, d^{\ell}_{mo}(\theta)e^{im\phi} \qquad (6)$$

where θ and ϕ are now the canonical scattering angles in the dipion c.m. system (see Fig. 1). We note that the

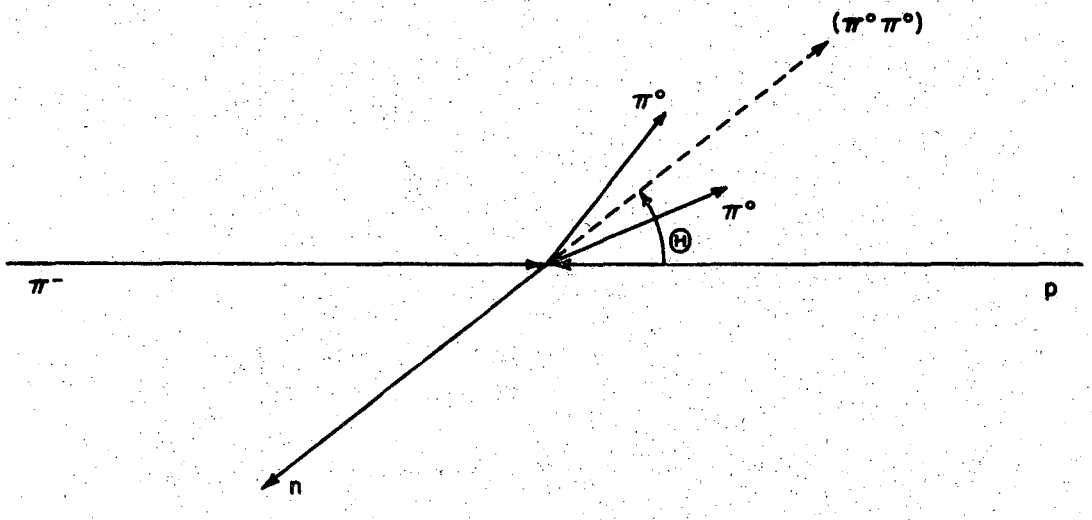

CM FRAME

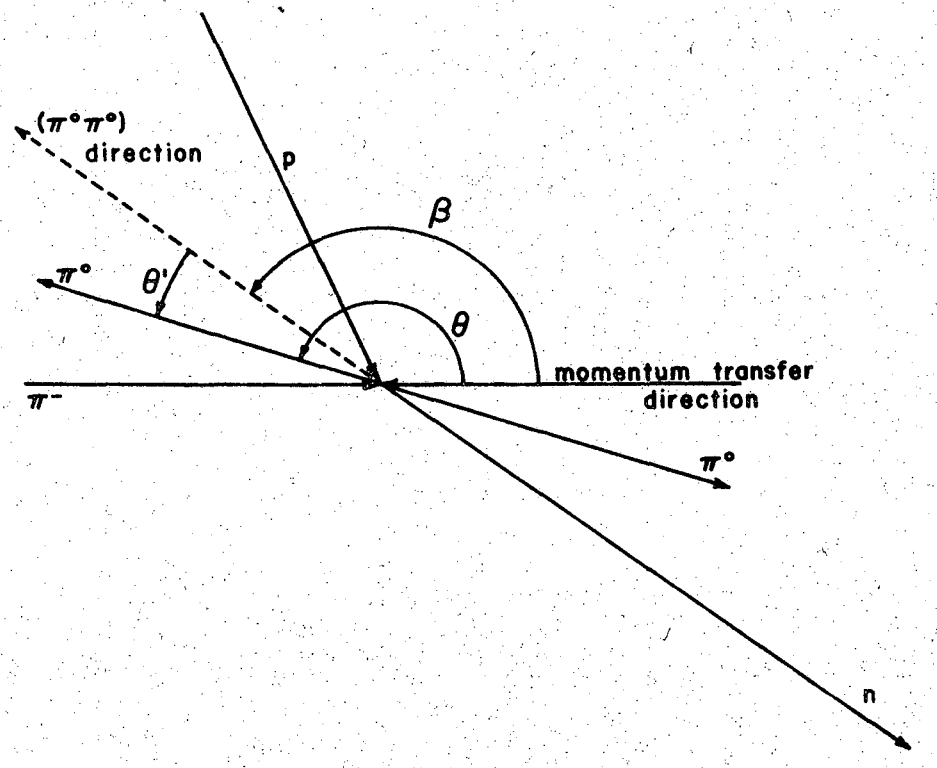

DIPION REST FRAME

XBL 7111-1631

Fig. 1. Dipion production and decay angles. The dipion decay is shown to occur in the production plane for convenience only--in practice, any rotation of the plane (in the cm frame) or the line (in the dipion rest frame) defined by the two π^o's around the dipion direction is allowed.

$$d^{\ell}_{oo}(\theta) = P_{\ell}(\cos\theta)$$

are the usual partial waves of π-π scattering, and that

$$T^{j\ell}_{\lambda\lambda'',\lambda'}(w,s) = \langle \ell\lambda\lambda'' | T^{j} | \lambda' \rangle$$

is a function of w and s only. Summing over j, λ, and λ', we may write

$$T^{\ell}_{m}(w,\ s,\ t) = \sum_{j\lambda'\lambda} (2j+1) T^{j\ell}_{\lambda\lambda'',\lambda'}(w,s)$$

$$\times\ d^{j}_{-\lambda',\lambda-\lambda''}(\Theta)\, d^{\ell}_{\lambda m}(-\beta(\Theta)) \qquad (7)$$

so that

$$A(\pi N \to \pi\pi N') = \sum_{\ell m} T^{\ell}_{m}(w,\ s,\ t) d^{\ell}_{mo}(\theta) e^{im\phi} \qquad (8)$$

If the form of the T^{ℓ}_{m}'s were known, it would be possible to extract the π-π scattering amplitudes and information could be obtained on π-π scattering from dipion production experiments.

3. The Chew-Low Conjecture

Some light was shed on the structure of the T^{ℓ}_{m}'s by G. Chew and F. Low.[9] They considered the possibility that the particle states represented by a production amplitude could be split into two groups, each of the groups having at least one complete set of quantum numbers in common. It was conjectured that if a physical particle existed with this set of complete quantum numbers, then the T^{ℓ}_{m}'s would have a pole term, at the mass of that particle, in the momentum transfer variable of the constituents of one of the groups.

Clearly one possible configuration of the groups in the case of the dipion production amplitude corresponds to an exchanged pion. This case is shown schematically in Fig. 2a. In terms of the T^{ℓ}_{m}'s we write

$$T^{\ell}_{m}(w,s,t) = \frac{B^{\ell}_{m}(w,s,t)}{(t - \mu^2)} + C^{\ell}_{m}(w,s,t) \qquad (9)$$

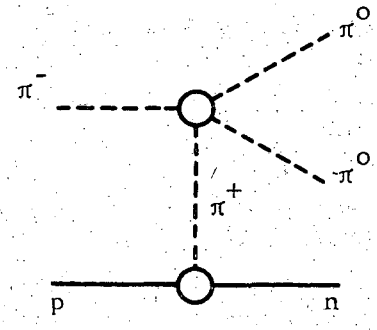

Fig. 2a. The one pion exchange diagram.

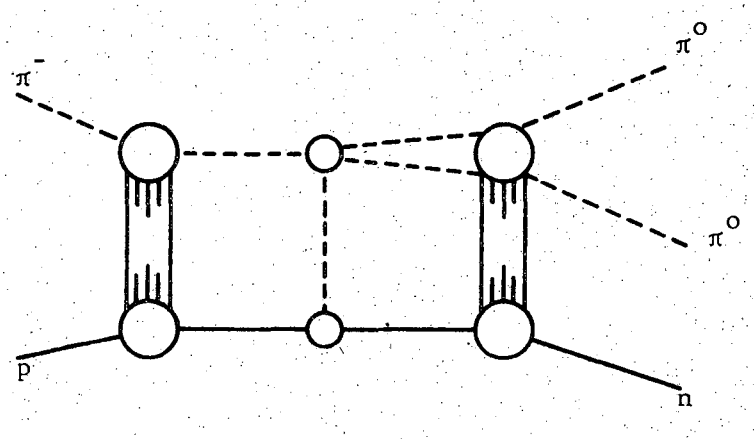

Fig. 2b. The one pion exchange modified by absorption.

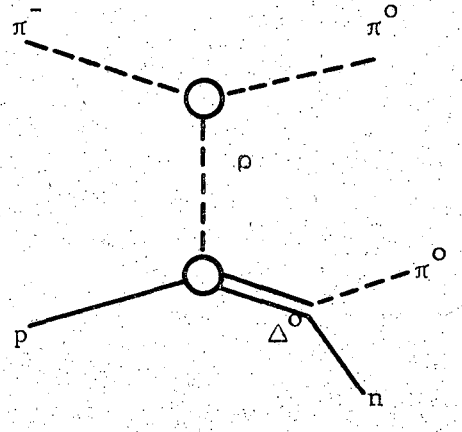

XBL 7110-1595

Fig. 2c. Other allowed exchanges in the reaction $\pi^- p \rightarrow \pi^o \pi^o n$.

where the B_m^ℓ's and C_m^ℓ's have no other poles in t near μ^2. Other poles in t may exist at the masses of other resonances, but there are further removed from the physical $t(< 0)$ region, and should not influence the observed T_m^ℓ's as much.

Other groupings of the particle states represented by the dipion production amplitudes are also possible leading to $\Delta(1238)$ production. These are indicated in Fig. 2c. Some of the possible exchanged particles are also indicated in this figure.

It is also assumed that at the pion pole

$$\lim(t \to u^2) T_m^\ell(w,s,t) = B_{N\pi N}(w, t = u^2) A_m^\ell(s)_{\pi\pi} \tag{10}$$

Thus the T_m^ℓ's factor at the pion pole into the $N\pi N$ vertex function and the π-π scattering amplitudes. It should be stressed that the existence of this limit does not imply that the $T_m^\ell(w,s,t)$'s factor everywhere. In particular we cannot necessarily assume that

$$T_m^\ell(w,s,t) = B(w,t) B_m^\ell(s) \tag{11}$$

for physical values of t. In practice, however, it is often necessary to make this assumption to obtain a reasonably simple parametrization of the data (see Sec. I. B.).

4. The One Pion Exchange Model with Absorption.[10]

If we assume the usual pseudoscalar point coupling at the $N\pi N$ vertex, we obtain near the pion pole

$$A(\pi N \to \pi\pi N) = \frac{ig\bar{u}\gamma_5 u}{(t - u^2)} B(s,\Omega) \tag{12}$$

where the coupling constant, g, can be written as

$$g_{p\pi p} = \frac{2M}{\mu} f(t) \qquad (\text{with } g_{n\pi p} = \sqrt{2}\ g_{p\pi p}) \tag{12.1}$$

with

$$\frac{f^2}{4\pi}(t = \mu^2) = 0.0822 \tag{12.2}$$

and μ and $\bar{u}$ are the Dirac spinors. Since we want to write the total cross-sections as

$$\sigma = \frac{1}{(2\pi)^5} \frac{1}{4p_o q_o v_{in}} \iiint \frac{d^3q'}{2q_o'} \frac{d^3q''}{2q_o''} \frac{d^3p'}{2p_o'} |A(s,t,w)|^2$$

the Dirac spinors must have the normalization $\bar{u}u = 2M$. The one pion exchange model assumes that this is the correct form of the amplitude for physical values of t as well. In this approximation we can write the differential cross-section of dipion production as

$$\frac{\partial^3\sigma}{\partial t \partial s \partial \Omega}_{\pi\pi} = \frac{1}{(4\pi)^4} \cdot \frac{1}{8} \cdot \frac{1}{M^2 P_{lab}^2} \cdot \frac{1}{\sqrt{s}} \cdot |q'|$$

$$\times \left\{ \sum_{\text{Spins}} \frac{1}{2} \left| \langle f|T|i\rangle \right|^2 \right\}$$

$$= \frac{1}{(4\pi)^4} \frac{1}{8} \cdot \frac{1}{M^2 P_{lab}^2} \frac{1}{\sqrt{s}} \cdot |q'| \frac{g^2(-t)}{(t-\mu^2)^2} |B(s,\Omega)_{\pi\pi}|^2$$

$$= \frac{1}{(4\pi)^2} \cdot \frac{1}{2} \cdot \frac{1}{M^2 P_{lab}^2} \cdot \sqrt{s}\,|q| \frac{g^2(-t)}{(t-\mu^2)^2} \frac{d\sigma_{\pi\pi}}{d\Omega_{\pi\pi}} \qquad (13)$$

where P_{lab} is the magnitude of the incident nucleon three momentum measured in the laboratory, while q and q' are the magnitudes of the three momenta of the initial and final pion, respectively, measured in the dipion rest frame.

It has been found experimentally, in those interactions in which one-pion exchange is allowed, that the differential cross-section, as a function of t, falls much more rapidly than is exhibited by the $t(t-\mu^2)^{-2}$ behavior of the one pion exchange equations. This can be rephrased to say that most of the dipions are produced more peripherally (that is, for smaller values of momentum transfer), than predicted by the one-pion exchange model.

To account for the discrepancy between observed data and the one

pion exchange model, it was suggested, since many final states are actually available to the initial state of the reaction, that the amplitude gets absorbed into competing channels, thus strongly attenuating the one pion exchange amplitude. This effect is schematically presented in Fig. 2b where the absorption is indicated by initial and final state interactions modifying the one pion exchange amplitude.

To obtain a semi-quantitative estimate of the effect of absorption we must expand the one pion exchange amplitude in terms of the helicity states. We have

$$A(\pi N \to \pi\pi N) = \sum_{\ell m} T^{\ell}_{m}(w,s,t) d^{\ell}_{mo}(\theta) e^{im\phi}$$

$$= \sum_{\ell m} \sum_{\lambda\lambda'} \frac{\bar{u}(p'\lambda'')\gamma_5 u(p,\lambda')}{(t-\mu^2)} \; d^{\ell}_{\lambda o} \left[-\beta(\Theta) \right] B^{\ell\lambda}_{\pi\pi}(s) d^{\ell}_{mo}(\theta) e^{im\phi} \qquad (14)$$

If we integrate out the ϕ dependence, we obtain

$$A(\pi N \to \pi\pi N) = \sum_{\ell} \sum_{\lambda\lambda'} A(w,t;\ell\lambda\lambda'',\lambda') d^{\ell}_{oo}(\theta)$$

where

$$A(w,t,\ell\lambda\lambda''\lambda') = \bar{u}(p',\lambda'') \frac{\lambda_5}{(t-\mu^2)} u(p,\lambda') d^{\ell}_{\lambda o}(-\beta) B^{\ell\lambda}_{\pi\pi}(s)$$

We note that

$$\bar{u}(p',\tfrac{1}{2})\gamma_5 u(p,\tfrac{1}{2}) = \left[(E+M)(E'+M)\right]^{\frac{1}{2}} \left(\frac{p}{E+M} - \frac{p'}{E'+M}\right) \cos\frac{\Theta}{2}$$

$$= \eta_- \cos\frac{\Theta}{2}$$

$$\bar{u}(p',\tfrac{1}{2})\gamma_5 u(p,-\tfrac{1}{2}) = \left[(E+M)(E'+M)\right]^{\frac{1}{2}} \left(\frac{p}{E+M} + \frac{p'}{E'+M}\right) \sin\frac{\Theta}{2}$$

$$= \eta_+ \sin\frac{\Theta}{2}$$

$$\bar{u}(p',-\tfrac{1}{2})\gamma_5 u(p,\tfrac{1}{2}) = \eta_+ \sin\frac{\Theta}{2}$$

$$\bar{u}(p',-\tfrac{1}{2})\gamma_5 u(p,-\tfrac{1}{2}) = -\eta_- \cos\frac{\Theta}{2}$$

We now expand the $A(w,t;\ell,\lambda\lambda'',\lambda')$ in terms of $d^{j}_{-\lambda,\lambda-\lambda''}(\Theta)$

$$A^{OPE}(w,t,;\ell\lambda\lambda'',\lambda') = \frac{1}{2\pi} \sum_{J} (J+\tfrac{1}{2}) a_J(w,s;\ell\lambda\lambda'',\lambda') d^{J}_{\lambda',\lambda-\lambda''}(\Theta) \qquad (15)$$

Absorption now modifies the a_J's by complex phase shifts representing the initial and final state interactions.

$$A^{ABS}(w,t;\ell\lambda\lambda'',\lambda') = \frac{1}{2\pi}\sum_J (J+\tfrac{1}{2}) e^{\delta_i^J(w,s)}$$

$$\times a_J(w,s;\ell\lambda\lambda'',\lambda') e^{\delta_f^J(w,s)} d^J_{\lambda',\lambda-\lambda''}(\Theta) \qquad (16)$$

In practice the e^{δ^J} are chosen to reproduce the observed exponential fall off of the data, a common choice being[11]

$$e^{\delta^J_{i,f}} = (1 - be^{-cJ^2})$$

This yields

$$A^{ABS}(w,t;\ell\lambda\lambda'',\lambda') = A^{OPE}(w,t;\ell\lambda\lambda'')$$

$$- \frac{1}{2\pi}\sum_J (2J+\tfrac{1}{2})\left(be^{-c'J^2} + b'e^{-cJ^2} - bb'e^{-(c+c')J^2}\right)$$

$$\times a_J d^J_{-\lambda',\lambda-\lambda''}(\Theta)$$

An even cruder approximation to absorption assumes that the $e^{\delta_i^J}e^{\delta_f^J}$ dependence is equivalent to multiplication by a factor $(a + b \cdot e^{ct})$. Hence

$$A^{ABS}(w,t;\ell\lambda\lambda'',\lambda') = (a + be^{ct})A^{OPE} \qquad (17)$$

where a, b, and c may be slowly varying functions of w, s, and t.

The main point to note in the absorption model is that the π-π scattering amplitudes are always factors of the three body production helicity amplitudes, although it does not mean that the functions modifying the one pion exchange amplitudes are independent of s. Thus we have

$$A^{ABS}(w,t,s) = A(w,s,t)B_{\pi\pi}(s)$$

However, in the limit

$$\lim t \to \mu^2 \quad (t - \mu^2)A^{ABS} = B(w)B_{\pi\pi}(s)$$

still must hold, and the only s dependence of the amplitudes at the pion pole is contained in the π-π scattering amplitudes.

5. Extrapolation

We note from the one pion exchange model, that

$$\frac{d\sigma}{d\Omega_{\pi\pi}} = \lim(t \to \mu^2)(4\pi)^2 \; 2M^2 p^2_{lab} \frac{1}{\sqrt{s}\,|q|} \times \frac{(t-\mu^2)^2}{g^2 t} \frac{\partial\sigma}{\partial t \partial s \partial\Omega_{\pi\pi}}$$

$$= (4\pi)^2 \; 2\,M^2 p^2_{lab} \frac{1}{\sqrt{s}\,|q|} \frac{1}{g^2\mu^2} \left\{ \lim\, t \to \mu^2 \; (t-\mu^2)^2 \frac{\partial^3\sigma}{\partial t \partial s \partial\Omega_{\pi\pi}} \right\} \quad (18)$$

If we now assume that the cross-section is analytic in t, we may write

$$(4\pi)^2 \; 2\,M^2 p^2_{lab} \frac{1}{\sqrt{s}\,|q|} \frac{|q'|}{g^2 t} \frac{\partial^3\sigma}{\partial t \partial s \partial\Omega_{\pi\pi}}$$

$$= \frac{a_{-2}(w,s,\Omega)}{(t-\mu^2)^2} + \frac{a_{-1}(w,s,\Omega)}{(t-\mu^2)} + a_o(w,s,\Omega)$$

$$+ \sum_{n=1}^{\infty} a_n(w,s,\Omega)(t-\mu^2)^n \quad (19)$$

Then multiplying both sides of the previous equation by $(t-\mu^2)^2$ and taking the limit as $t \to \mu^2$ we obtain

$$|B_{\pi\pi}|^2 = a_{-2}(w,s,\Omega)$$

Except for the factor of $1/t$, this method of obtaining the $|B_{\pi\pi}|^2$ is independent of the one pion exchange model and only depends on how accurately we can obtain the expansion of $\frac{\partial^3\sigma}{\partial t \partial s \partial\Omega_{\pi\pi}}$ in terms of a power series in $(t-\mu^2)$ from the data. However many terms may have to be kept in the expansion yielding many parameters $a_n(w,s,\Omega)$. In addition possible experimental values of t may be far removed from the pion pole, making the fit rather ambiguous. Since we want $a_{-2}(w,s,\Omega)$ at the pole, this may introduce large errors in $|B_{\pi\pi}|^2$. In particular, in the reaction $\pi^- p \to \pi^o \pi^o n$, the physical final state may be dominated by

$\Delta(1238)$ production, which may obscure the correct expansion of the π-π cross-section as a function of t.

Recently it has been suggested that instead of using $(t - \mu^2)$ as the expansion variable, a conformal mapping of the cross-section should be made which would emphasize the small t values of the data, making the convergence more rapid.[12]

6. Form Factors

We may write the differential cross-section for dipion production as

$$\frac{\partial^3\sigma}{\partial t \partial s \partial \Omega_{\pi\pi}} = \frac{1}{(4\pi)^4} \cdot \frac{1}{8} \cdot \frac{1}{M^2 p_{1ab}^2} \cdot \frac{1}{\sqrt{s}} \cdot |q'| |A(\pi N \to \pi\pi N)|^2 \qquad (20)$$

We have observed that using the Chew-Low conjecture the amplitude may be written as

$$A(\pi N \to \pi\pi N) = \sum_{\ell m} \frac{B^{\ell}_{m}(w,s,t)}{(t - \mu^2)} d^{\ell}_{mo}(\theta) e^{im\phi}$$

$$= \sum_{\ell m} \sum_{\lambda\lambda'} B^{\ell}_{m,\lambda\lambda'}(w,s,t) \frac{d^{\ell}_{mo}(\theta) e^{im\phi}}{(t - \mu^2)} \qquad (21)$$

near the pion pole. If the strong variation of the amplitude in t (for physical t) can be represented by a set of functions $F^{\ell}_{\lambda\lambda' m}(s,t)$, called form factors, then we may write

$$(t - \mu^2)A(\pi N \to \pi\pi N) = \sum_{\ell m} \left\{ \sum_{\lambda\lambda'} F^{\ell}_{\lambda\lambda' m}(s,t) S^{\ell}_{\lambda\lambda' m}(w,s,t) \right\}$$

$$\times d^{\ell}_{mo}(\theta) e^{im\phi} \qquad (22)$$

where $S^{\ell}_{\lambda\lambda' m}(w,s,t)$ is now only a slowly varying function of t. It is the functions $S^{\ell}_{\lambda\lambda' m}$ that we now expand in a power series

$$S^{\ell}_{\lambda\lambda' m}(w,s,t) = a_o(w,s;\ell m,\lambda\lambda') + a_1(w,s;\ell m,\lambda\lambda')(t - \mu^2) + \ldots$$

If we further insist that $F^{\ell}_{\lambda\lambda' m}(t = \mu^2) = 1$, then the coefficients

$$b^{\ell}_{m}(w,s) = \sum_{\lambda\lambda'} a_o(w,s;\ell m,\lambda\lambda')$$

are the appropriate partial wave amplitudes for π-π scattering.

It is assumed that by introducing the functions $F^{\ell}_{\lambda\lambda' m}(s,t)$, the power series expansion of $S^{\ell}_{\lambda\lambda' m}$ will converge very rapidly, so that only a few terms must be kept in the expansion. This is a considerable advantage, when extrapolation techniques are to be used to obtain the π-π phase shifts from dipion production data.

It is, of course, the square of the amplitude that is obtained from the data, so that we have

$$(t-\mu^2)^2\left|A(\pi N \to \pi\pi N)\right|^2 = \sum_{\substack{\ell m \\ \ell' m' K K'}} \sum_{\lambda\lambda'} F^{*\ell'}_{KK' m'} F^{\ell}_{\lambda\lambda' m}$$

$$\times\ S^{*\ell'}_{KK' m'} S^{\ell}_{\lambda\lambda' m} d^{*\ell'}_{m' o}(\theta) d^{\ell}_{mo} e^{i(m-m')\phi} \qquad (23)$$

Writing

$$F(s,t;\ell m\lambda\lambda';\ell' m' KK') = F^{*\ell'}_{KK' m'} F^{\ell}_{\lambda\lambda' m}$$

and

$$S(w,s,t;\ell m\lambda\lambda';\ell' m' KK') = S^{*\ell'}_{KK' m'} S^{\ell}_{\lambda\lambda' m}$$

we now form the expansion

$$S(w,s,t;\ell m\lambda\lambda';\ell' m' KK') = \sum_{m=0}^{\infty} a_n(w,s;\ell m\lambda\lambda';\ell' m' KK')(t-\mu^2)^n \qquad (24)$$

This expansion also will converge rapidly, if the power series expansion of $S^{\ell}_{\lambda\lambda' m}$ did so. [In practice, the expansion is truncated for some $\ell = \ell_{max}$, so that we obtain only a finite number of functions $F(\ell m\lambda\lambda';\ell' m' KK')$.] We then obtain

$$(t-\mu^2)^2\left|A(\pi N \to \pi\pi N)\right|^2 = \sum_{\substack{\ell m \ell' m' \\ \lambda\lambda' KK'}} \sum_{n=0}^{\infty} F(s,t;\ell m\lambda\lambda';\ell' m' KK')$$

$$\times\ a_n(w,s;\ell\ell n\lambda\lambda';\ell' m' KK')(t-\mu^2)^n$$

$$\times\ d^{*\ell'}_{mo}(\theta) d^{\ell}_{mo}(\theta) e^{i(m-m')\phi} \qquad (25)$$

Additional simplifying assumptions are often made. Usually, when the

functions $F(s,t;\ell m\lambda\lambda';\ell' m'\kappa\kappa')$ are chosen to fit the data, one sets

$$F(s,t;\ell m\lambda\lambda';\ell' m'\kappa\kappa') = f(w,s,t)$$

for all the angular momentum quantum numbers. We then have

$$\begin{aligned}
&(t-\mu^2)^2|A(\pi N\to\pi\pi N)|^2 \\
&= f(w,s,t)\sum_{n=0}^{\infty}\sum_{\substack{\ell m\\ \ell' m'}}\left\{\sum_{\lambda\lambda'\ \kappa\kappa'} a_n(w,s;\ell m\lambda\lambda';\ell' m'\kappa\kappa')\right\}(t-\mu^2)^n \\
&\times d^{*\ell'}_{m'o}(\theta)d^{\ell}_{mo}(\theta)e^{i(m-m')\phi} \\
&= f(w,s,t)\sum_{m=0}^{\infty}\sum_{\substack{\ell m\\ \ell' m'}} a_n^{\ell m,\ell' m'}(w,s)d^{*\ell'}_{m'o}(\theta)d^{\ell}_{mo}(\theta) \\
&\qquad\times\left\{e^{i(m-m')\phi}(t-\mu^2)^n\right\} \qquad (26)
\end{aligned}$$

If we now assume that we can truncate the expansion in $(t-\mu^2)$ after $n=0$, we obtain

$$\begin{aligned}
&(t-\mu^2)^2|A(\pi N\to\pi\pi N)|^2 \\
&= f(w,s,t)\sum_{\substack{\ell m\\ \ell' m'}} a_o^{\ell m,\ell' m'}(w,s)\,d^{*\ell'}_{m'o}(\theta)d^{\ell}_{mo}(\theta)e^{i(m-m')\phi} \\
&= f(w,s,t)\left|B_{\pi\pi}(s,\Omega)\right|^2 \qquad (27)
\end{aligned}$$

and we see that the π-π scattering amplitudes differ from the production amplitudes by a factor $f(w,s,t)$. In this case, we may write

$$\begin{aligned}
\frac{\partial^3\sigma}{\partial t\partial s\partial\Omega_{\pi\pi}} &= \frac{1}{(4\pi)^4}\cdot\frac{1}{8}\cdot\frac{1}{M^2P_{1ab}^2}\cdot\frac{1}{\sqrt{s}}\cdot|q'|g^2\mu^2\qquad\frac{f(t,s,w)}{(t-\mu^2)^2}\left|B_{\pi\pi}(s,\Omega)\right|^2 \\
&= \frac{\mu^2}{(-t)}\frac{1}{f(t,s,w)}\left.\frac{\partial^3\sigma}{\partial t\partial s\partial\Omega\pi\pi}\right|_{OPE}
\end{aligned}$$

and

$$\frac{\partial\sigma}{\partial\Omega_{\pi\pi}}(s,\Omega) = (4\pi)^2\cdot 2\cdot\frac{M^2P_{1ab}^2}{\sqrt{s}\,|q|}\frac{1}{g^2\mu^2}\qquad\frac{(t-\mu^2)^2}{f(t,s,w)}\frac{\partial^3\sigma}{\partial t\partial s\partial\Omega\pi\pi} \qquad (28)$$

so that the π-π scattering cross-sections can be obtained directly from the dipion production cross-sections.

It is with these very particular assumptions, that the method of form factors has achieved its widest use. The prescription, followed by most data analyses of production cross-sections, parametrizes a function $f(w,s,t)$, such that $f(w,s,t = \mu^2) = 1$, which approximates the projected t distributions quite well. Then the deviation away from this distribution of the remaining projections of the Dalitz plot is attributed to pure π-π scattering. It should be noted that the form factors can be different for each cofficient modifying the helicity amplitudes, as displayed expliciting in Eq. (25). A number of collaborations have also attempted to parametrize the $\pi^+\pi^-$ final state in this manner.[13]

A commonly used form factor for dipion production cross-sections has the form

$$f(w,s,t) = e^{a(s)(t - \mu^2)} \cdot \frac{t}{\mu^2} \tag{29}$$

where a is usually chosen to be a constant over the energy range of the fitted data. It is, of course, not necessary for a to be constant for the form factor method to be valid. It should be noted, that this functional form, in a crude sense, attempts to take into account deviations away from the one-pion exchange model by representing absorption by the exponential fall-off of the form factor.

A form factor that often fits the data well, has the form

$$f(t,s) = \frac{t}{\mu^2} e^{a(t - t_{min})} = \frac{t}{\mu^2} e^{a(t - \mu^2) - a(t_{min} - \mu^2)} \tag{30}$$

where $t_{min} = t_{min}^{(s)}$ is the minimum momentum transfer possible for a given value of s. In this case

$$\frac{\partial^3\sigma}{\partial t \partial s \partial \Omega_{\pi\pi}} = \frac{1}{(4\pi)^4} \cdot \frac{1}{2} \frac{1}{M^2 P_{lab}^2} \frac{1}{\sqrt{s}} |q'| \, g^2\mu^2 \frac{t}{\mu^2} \frac{e^{a(t - t_{min})}}{(t - \mu^2)^2} f(s)$$

and going to the pion pole we have

$$|B_{\pi\pi}|^2 = e^{-a\left|t_{min}^{(s)} - \mu^2\right|} f(s)$$

but not

$$|B_{\pi\pi}|^2 \neq f(s)$$

as might be expected.

More complicated form factors have been introduced by Dürr and Pilkuhn,[14] Kane and Ross,[15] and others, to take into account threshold effects, angular momentum barriers, and kinematic singularities in the t-channel. For a description of these particular types of form factors, one should refer to the literature.

7. Parametrization of Dipion Production in the Reaction $\pi^- p \to \pi^o \pi^o n$

Following the previous section, we write

$$(t - \mu^2)^2 |A(\pi^- p \to \pi^o \pi^o n)|^2 = \sum_{\substack{\ell m \ell' m' \\ \lambda\lambda' KK'}} \sum_{n=0}^{\infty} F(s,t;\ell m \lambda\lambda';\ell' m' KK')$$

$$\times a_n(s,w;\ell m\lambda\lambda';\ell' m' KK')(t - \mu^2)^n$$

$$\times d^{*\ell'}_{m'o}(\theta) d^{\ell}_{mo}(\theta) e^{i(m - m')\phi}$$

For c.m. energies in the dipion rest fram below 1 GeV, we may truncate the series after $\ell = 0$ (since odd ℓ states cannot contribute to the $\pi^o\pi^o n$ final state and we have assumed that only $\ell = 0$ and $\ell = 1$ partial wave amplitudes contribute in this energy range). We then obtain

$$(t - \mu^2)^2 |A(\pi^- p \to \pi^o \pi^o n)|^2 = \sum_{n=0}^{\infty} \sum_{\substack{\lambda\lambda' \\ KK'}} F(s,t;\lambda\lambda',KK')$$

$$\times a_n(w,s'\lambda\lambda',KK')(t - \mu^2)^n$$

Performing the summation over the nucleon helicity states, we may recast this equation in the form (by redefining variables if necessary)

$$(t - \mu^2)^2 |A(\pi^- p \to \pi^o \pi^o n)|^2 = \sum_{n=0}^{\infty} f(t,s) a_n(w,s)(t - \mu^2)^n$$

(where $f(t,s) \neq \sum_{\substack{\lambda\lambda' \\ KK'}} F(t,s;\lambda\lambda';KK')$ necessarily).

It should be noted that the only assumption we have introduced so far is the one that only $\ell = 0$ states contribute to the final state. Hence

$$(4\pi)^4 \cdot 8 \cdot M^2 P_{lab}^2 \frac{\sqrt{s}}{g^2\mu^2} \frac{1}{|q|} \frac{(t-\mu^2)^2}{f(t,s)} \frac{\partial^3\sigma}{\partial t \partial s \partial \Omega_{\pi\pi}}$$

$$= |B_{\pi\pi}(s,\Omega)|^2 + \sum_{n=1}^{\infty} a_n(w,s)(t-\mu^2)^n \qquad (31)$$

If we also assume that the series terminates after n = 0, we immediately obtain $|B_{\pi\pi}(s,\Omega)|^2$ from the data, provided we can obtain a parameterization of f(w,s,t). In this case, we have

$$\frac{\partial^3\sigma(\pi^- p \to \pi^o\pi^o n)}{\partial t \partial s \partial \Omega_{\pi\pi}} = \frac{1}{(4\pi)^2} \cdot \frac{1}{2} \cdot \frac{1}{M^2 P_{lab}^2} \sqrt{s}\ |q|\ g^2\mu^2$$

$$\times \frac{f(t,s)}{(t-\mu^2)^2} \frac{1}{|q'|^2} \frac{4}{9} \sin^2(\delta_o^o - \delta_o^2) \qquad (32)$$

where

$$\frac{1}{|q'|^2} |A(\pi^+\pi^- \to \pi^o\pi^o)|^2 = \frac{|q'|}{(8\pi)^2 s\,|q|} |B_{\pi\pi}(s,\Omega)|^2$$

B. Experimental Status of π-π Scattering Amplitudes

The invariant isotopic spin amplitudes $f^I(s,\theta)$ of π-π scattering are usually represented, below 1 GeV of the dipion mass, by the first term in the partial wave expansion, yielding

$$f^o = 2e^{i\delta_o^o} \sin \delta_o^o$$
$$f^1 = 6e^{i\delta_1^1} \sin \delta_1^1 \cos \theta$$
$$f^2 = 2e^{i\delta_o^2} \sin \delta_o^2$$

so that each of the amplitudes is completely specified by a single phase shift δ_ℓ^I. Considerable effort has been expanded over a ten year period to measure the δ_ℓ^I's as a function of the invariant dipion mass, these measurements being mainly derived from production experiments.

Examination of Eqs. (1) - (4) of Sec. I. A. 1. shows that δ_o^2 can be unambiguously obtained from $\pi^+\pi^+$ elastic scattering experiments. Unfortunately, no experimental determination of δ_o^2 using this interaction, or the corresponding production reaction $\pi^+ p \rightarrow \pi^+\pi^+ n$, has been done. On the other hand, Baton et al.[16] have recently extracted the $I = 2$, $\ell = 0$ phase shifts as a function of the $\pi^o\pi^-$ mass (see Fig. 3) from the production reaction $\pi^- p \rightarrow \pi^o\pi^- p$. It is relatively flat and structureless and also negative in the dipion mass region below 1 GeV.

From the same equations, it can be seen that δ_1^1 can be obtained from $\pi^\pm\pi^o$ elastic scattering by a partial wave analysis of the angular distribution of the final state (the corresponding production experiments being $\pi^\pm p \rightarrow \pi^+\pi^o p$). It has been easily observed that $\pi^\pm\pi^o$ production is dominated by a resonant state of mass 760 MeV, subsequently named the ρ, even without using the more sophisticated extrapolation or form factor techniques. An examination of the pion angular distribution in the dipion rest frame revealed a forward-backward asymmetry that changed

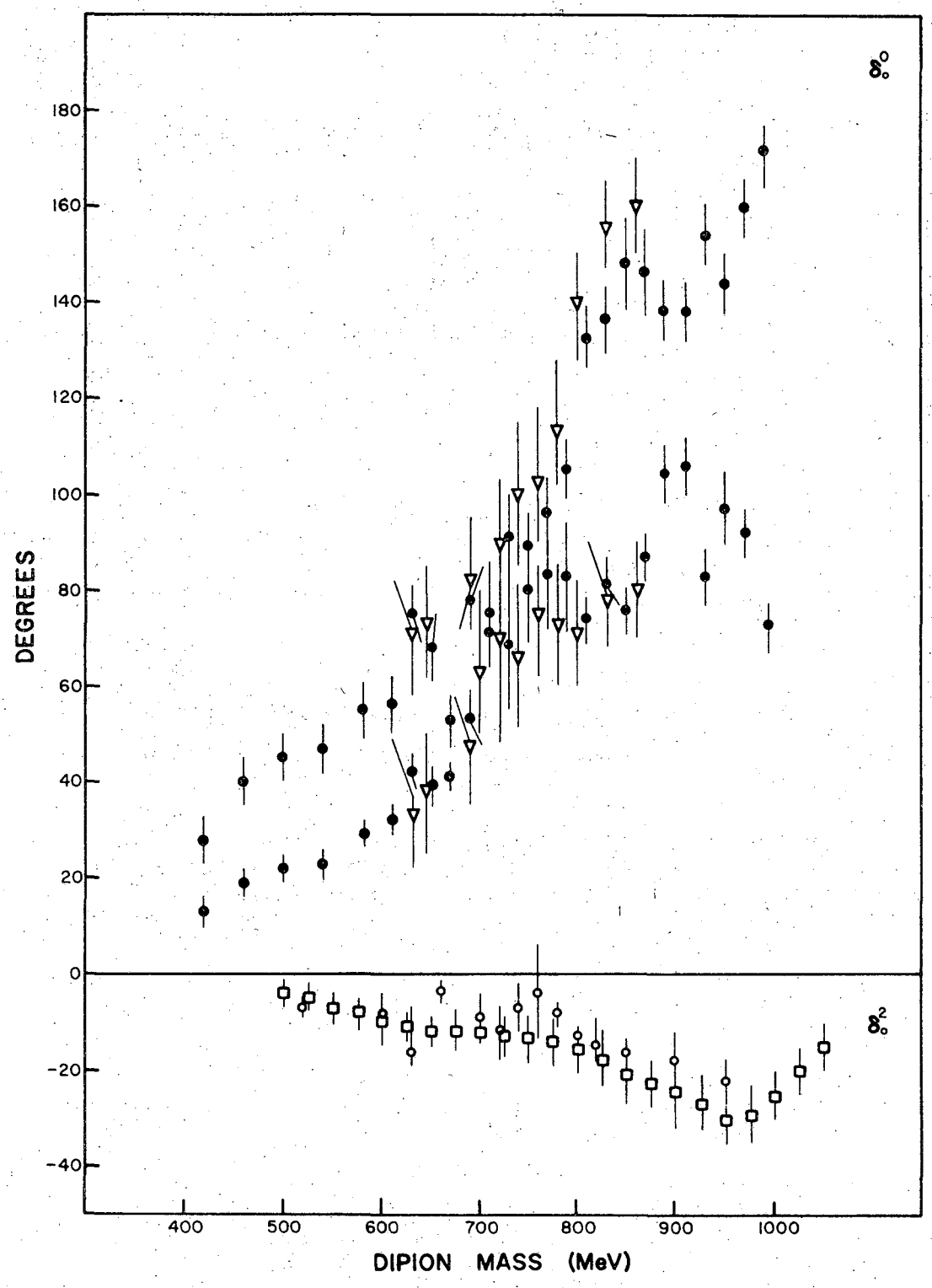

Fig. 3. The s-wave phase shifts. The down-up and up-down solutions of Schlein et al. (♦) and the solutions of Gutay et al. (▽) are shown for $\delta_0{}^0$. The two solutions of Baton et al. for $\delta_0{}^2$ are also shown (◊,▽).

sign as it passed through the ρ region. This asymmetry has been attributed to the interference of the f^1 with the f^2 amplitudes in the $\pi^{\pm}\pi^o$ scattering. The ρ parameters (mass and width) obtained using extrapolation and form factor techniques on the production amplitudes can be directly compared to those obtained in ρ photoproduction ($e^+e^- \rightarrow \rho \rightarrow \pi^+\pi^-$) thus yielding a measure of the effectiveness of obtaining π-π scattering information from production experiments. The results are in reasonable agreement.[17]

The ρ meson can also be observed to dominate $\pi^+\pi^-$ elastic scattering [Eq. (3)] as observed in production experiments of the type $\pi^- p \rightarrow \pi^+\pi^- n$. In this case the pion decay distributions in the dipion rest frame show a persistent forward-backward asymmetry that retains the same sign as it passes through the ρ region. This asymmetry has been attributed to a resonant f^0 amplitude, interfering with the f^1 amplitude in the proximity of the ρ mass.

It has been the f^0 amplitude, and consequently δ_o^o, that has been the most difficult to extract from the experimental data. The phase shift δ_o^o can be measured in $\pi^+\pi^-$ elastic scattering (in the production experiments $\pi^- p \rightarrow \pi^+\pi^- n$, $\pi^+ n \rightarrow \pi^+\pi^- p$) and charge exchange (in the corresponding experiments $\pi^- p \rightarrow \pi^o\pi^o n$, $\pi^+ n \rightarrow \pi^o\pi^o p$). Since the elastic scattering has charged pions in the final state, it has been more amenable for bubble chamber analysis than has been charge exchange scattering. A number of groups have collaborated to analyze the world's sample of $\pi^+\pi^-$ bubble chamber data. All these analyses, however, have been plagued by a number of problems.

Upon examination of Eq. (3) again,

$$\frac{d\sigma}{d\Omega}(\pi^+\pi^- \rightarrow \pi^+\pi^-) = \frac{1}{K^2}(D_1 + D_2 \cos\theta + D_3 \cos^2\theta) \qquad (3)$$

$$D_1 = \frac{4}{9}\sin^2\delta_o^o + \frac{1}{9}\sin^2\delta_o^2 + \frac{4}{9}\cos(\delta_o^o - \delta_o^2)\sin\delta_o^o \sin\delta_o^2 \qquad (3.1)$$

$$D_2 = 4\cos(\delta_o^o - \delta_1^1)\sin\delta_o^o \sin\delta_1^1 + 2\cos(\delta_o^2 - \delta_1^1)\sin\delta_o^2 \sin\delta_1^1 \qquad (3.2)$$

$$D_3 = 9\sin^2\delta_1^1 \qquad (3.3)$$

we observe that the cross-section is dominated by the ρ meson in the p-wave (D_3). The s-p interference term, D_2, however, can be used to obtain $\delta_o^o(s)$, if we assume that $\delta_1^1(s)$ is adequately represented by the ρ resonance Breit-Wigner and that $\delta_o^2(s)$ is correctly represented by the data of Baton et al. This proceedure, however, yields two ambiguities.

(a) If we set $\delta_o^{o''} = \delta_o^o + \pi$, then D_2 is invariant under this substitution. The correct choice of δ_o^o in this case can be made by a careful study of the $\pi^o\pi^o/\pi^+\pi^+$ intensity ratio for low ππ masses. Cline et al.[18] have studied this problem and have shown that δ_o^o is initially positive and remains positive if we assume the $\delta_o^2(s)$ phase shift of Baton et al.

(b) If we make the substitution

$$\delta_o^{o''} = \frac{\pi}{2} - (\delta_o^o - \delta_1^1) \qquad (33)$$

in Eq. (3.2), we obtain

$$D_2 = 4\cos\left(\frac{\pi}{2} - (\delta_o^{o''} - \delta_1^1) - \delta_1^1\right)\sin\left(\frac{\pi}{2} - (\delta_o^{o''} - \delta_1^1)\right)\sin\delta_1^1 + 2\cos(\delta_o^2 - \delta_1^1)\sin\delta_o^2 \sin\delta_1^1$$

$$= 4\sin\delta_o^{o''}\cos(\delta_o^{o''} - \delta_1^1)\sin\delta_1^1 + 2\cos(\delta_o^2 - \delta_1^1)\sin\delta_o^2 \sin\delta_1^1$$

and we see that D_2 is invariant under the transformation. D_1, of course, is not invariant under this substitution of variables. It has been argued by Gutay et al.[19] and generally accepted by others, however, that the observed D_1 is strongly affected by incoherent background and the depolarization of the ρ due to absorption. Hence, it cannot be used to resolve reliably the ambiguity inherently present in D_2.

From Eq. (33), we see that for $\delta_1^1(s) = \frac{\pi}{2}$ (at $s = m_\rho^2$)

$$\delta_o^o(s = m_\rho^2) + \delta_o^{o''}(s = m_\rho^2) = \pi$$

If, in addition, $\delta_o^o = \delta_o^{o''}$, then $\delta_o^o = \frac{\pi}{2}$, and we have a resonance in $f^o(s,\theta)$ at m_ρ^2 as well. In fact the $\pi^+\pi^-$ data indicate that the various solutions for δ_o^o do cross at approximately the mass of the ρ meson and hence f^o does resonate at this mass. Figure 3 illustrates the experimental situation for the measurement of δ_o^o (as obtained from $\pi^+\pi^-$ data), showing explicitly the various possible solutions. Since the various solution curves cross at $\delta_o^o \approx \frac{\pi}{2}$, within experimental error, they cannot be connected unambiguously (using continuity arguments) above and below the crossing point. Thus there are four possible solutions in all for the $I = 0$, $\ell = 0$, phase shift, picturesquely called the up-up, up-down, down-up, and down-down solutions. Furthermore if the solutions are interpreted to represent a resonant state at the mass of the meson, the width of the resonance depends on which of the four possible solutions is favored to be correct. Despite many attempts, at present the $\pi^+\pi^-$ data has not yielded a convincing unique solution for the δ_o^o phase shift.

Two major compilations of the world's $\pi^+\pi^-$ bubble chamber data have been analyzed by Gutay et al.[20] and Schlein et al.[21] The two analyses differ in their method of extracting the π-π scattering amplitudes from the production interaction data, and subsequently differ in their four possible solutions for δ_o^o. Thus there exists, not only a fourfold ambiguity due to the functional form of the $\pi^+\pi^-$ scattering cross-section, but also, a discrepancy in the results of the fits to the data (in many cases, the same data), yielding different results for the four possible solutions.

Gutay et al.[20] calculate their π-π scattering amplitude in the Born

approximation (one pion exchange model) and apply absorption corrections as outlined in Sec. I.A.4 to take into account the t dependence of the observed cross-sections. Keeping only s and p waves and using the dipion decay distribution for only small t values (on the assumption that these amplitudes extrapolate correctly to the π-π scattering amplitudes in the limit of $t = m^2_\pi$), they fit their data to the ratio D_2/D_3. They use a Breit-Wigner resonance corresponding to the ρ to represent the δ^1_1 phase shift. Obtaining δ^2_o from other experiments (or neglecting it entirely) they are then able to get δ^o_o from the ratio D_2/D_3.

Schlein and Malamud,[21] on the other hand, assume that the helicity amplitudes of Eq. (8) factor, so that writing

$$A(\pi N \to \pi\pi N) = \sum_{\ell m} T^\ell_m(w,s;t)Y^\ell_m(\Omega)$$

they obtain

$$A(\pi N \to \pi\pi N) = \sum_\ell B^\ell_{\pi\pi}(s)\left(\sum_m \frac{B^\ell_m(w,t)Y^\ell_m(\Omega)}{(t-\mu^2)}\right)$$

They then set $B^\ell_m = (a(t) + b(t)e^{ct})$ where $a(t)$ and $b(t)$ are polynomials in t, while c is a constant (it may be zero) and extract the $|B^\ell_{\pi\pi}(s)|^2$ from the moments $\langle Y^\ell_m(\Omega)\rangle$ of the π-π decay distributions.

Gutay et al. favor their down-up solution for δ^o_o while Schlein et al. favor their up-up solution. It should be pointed out that the up-up solution of Schlein et al. is consistently 15 to 20 deg greater than the down-up solution of Gutay et al. in the dipion region below the ρ mass. The two solutions appear to agree in the region from 750 to 1000 MeV. It should be emphasized that all these analyses assume negligible contributions from $\pi p \to \Delta\pi$ to the data. An analysis similar to the one outlined has been carried out by Schlein et al.[22] for the reaction $\pi^- p \to \Delta\pi^+\pi^-$ with similar results.

In summary, all these efforts have had to contend with the funda-

mental ambiguity of the fourfold solution for δ_o^o as obtained from $\pi^+\pi^-$ scattering data, and while the various analyses have favored various solutions (not necessarily the same), none has provided a convincing unique solution. To overcome this problem one must isolate the f^o from the f^1 amplitude, by studying a π-π reaction in which the ρ does not occur, namely $\pi^+\pi^- \to \pi^o\pi^o$. Because the final state pions are identical, the dipion can only have the quantum numbers I = 0, or 2. Thus

$$\frac{d\sigma}{d\Omega}(\pi^+\pi^- \to \pi^o\pi^o) = \frac{1}{K^2} \cdot \frac{4}{9} \cdot \sin^2(\delta_o^2 - \delta_o^o)$$

for events below 1 GeV in the dipion mass. The corresponding production reaction is $\pi^- p \to n\pi^o\pi^o$, having a completely neutral final state. Each of the π^o's decays into two gamma rays with a mean life of 0.76×10^{-16} seconds in its own rest frame. Thus, to observe the reaction unambiguously we have to detect a neutron and four gamma rays.

A number of experiments have been done to observe the reaction $\times^- p \to \pi^o\pi^o n$ (or $\pi^+ n \to \pi^o\pi^o p$). These can be grouped into three categories.

(a) Only the gamma rays arising from the $\pi^o\pi^o$ final state are detected in the course of data taking. If both energy and direction of all four photons can be measured, then it is possible to reconstruct the entire final state. Usually, it is difficult to measure the gamma ray energies very accurately and at the same time obtain good angular resolution on the gamma ray directions. It is, however, possible to reconstruct the final state without obtaining the photon energies (and hence, the entire final state).

If a particle, like the π^o, decays isotropically into two massless particles in its own rest frame, then from kinematics, it is possible to show that in any other reference frame in which the particle moves with a velocity β there is a minimum opening angle between the decay products.

It is a function only of the rest mass of the particle and its velocity in the given reference frame. Furthermore, the probability distribution of opening angles peaks sharply at minimum opening angle. In addition, at minimum opening angle, the direction and energy of the parent particle can be uniquely determined from the direction of the decay products.[23] Thus, if it is assumed that all opening angles are minimum opening angles, in the c.m. frame, say, then it is possible to reconstruct the π^o four momentum by using only the gamma ray directions.

In the case of the $\pi^o\pi^o$ final state, there are in fact two π^o's that have to be reconstructed from the gamma ray directional information, so that three possible pairings of the four gamma rays exist, which will yield different momenta for the final state π^o's, and hence, different dipion invariant masses. A criterion must be established, in this case, to choose which of the pairings is appropriate (the requirement that the neutron energy, by momentum conservation, be positive, is usually not enough). The criteria are all, more or less, arbitrary. A choice that is sometimes made requires one to select that pairing of the gamma rays which will yield a dipion having its momentum as similar to that of the incident π^- as possible. This choice reflects the peripheral nature of the interaction (but may tend to force the data to appear more peripheral than it actually was, in fact).

The pairing ambiguity can still exist if the gamma ray energies are measured with large errors, although in this case the ambiguity should not occur as often.

In addition, the method of detecting only four gamma rays cannot distinguish those events which have six gammas, say, in the final state, only four of which are observed. (This process we will call feed-down.) Thus the final results depend heavily on Monte Carlo calculations

yielding the correct background distributions for multi-gamma events that are detected as four gamma events (or ignore this possibility entirely).

(b) The gamma rays as well as the neutron are detected, but only the neutron time of flight and direction are measured. This type of experiment is, in essence, a missing mass experiment for four photon events. It cannot reconstruct the entire final state, and, in particular, cannot estimate the amount of $\Delta(1238)$ background that may be present. It also suffers from the problem that multi-photon events that are detected as four gamma events will be treated identically to the legitimate data, yielding a (possibly) large and usually unknown background.

(c) All four gammas and the neutron are detected and measured yielding a complete measurement of the final state. Unfortunately, all experiments that have attempted to measure the total final state suffer from limited statistics (a few hundred events).

The experiment of Wahlig et al.,[24] Corbett et al.[25] and the first experiment of Sonderegger et al.[26] fall within category (a).

Wahlig et al.[24] observed the gammas of the final state using brass plate spark chambers, but did not observe the recoil neutron. Using a form factor of the type of Eq. (29), and assuming that the production amplitudes factor, they were able to determine a broad resonance in the $\pi^o\pi^o$ mass spectrum centered at 600 ± 100 MeV with a full width of 400 ± 100 MeV. Their mass resolution was of the order of 100 MeV. The data was taken at an incident beam momentum of 10 GeV/c, and because of their restricted geometrical acceptance they could not observe the $n\pi$ channel below 1.5 GeV thus limiting any $\Delta(1238)$ events.

Corbet et al.[25] had incident π^- beam momenta of 1.7, 1.88, 2.1, 2.3 and 2.46 GeV/c in their experiment. They observed the four gamms of the

final state in a cubical array of thin plate spark chambers, but did not detect the recoil neutron. The final state was reconstructed using the minimum opening angle assumption, giving a $(\pi^o\pi^o)$ mass resolution of 100 MeV. Rejecting all events in the $\Delta(1238)$ region $(1.2 < m_{N\pi}^2 < 1.7)$, their data was consistent with a broad resonance at 600 MeV with a full width of 400 MeV. Although it was never stated, the statistics of the fit is consistent with a total sample of 100 events.

Sonderegger et al.[26] have observed the $n\pi^o\pi^o$ final state in two different experiments using a single stack of lead plate spark chambers exposed to a beam momentum ranging from 3 to 18 GeV/c. They did not observe the recoil neutron in the first of their experiments, but obtained an estimate of the gamma ray energies by counting the number of sparks in each shower. Obtaining a three constraint fit to the kinematics (they assume that the particle recoiling against the $\pi^o\pi^o$ system is a neutron), they saw no $\Delta(1238)$ contribution in their final state, but did find that their estimate of δ_o^o is consistent with the up-down solution of Schlein et al. They assumed that the form of the cross-section was the same as that used by Wahlig et al.

The experiment of Deinet et al.[27] and the first experiment of Feldman et al.[28] fall within the second category.

Feldman et al.[28] have done two experiments to look at the $n\pi^o\pi^o$ final state at incident π^- momenta of 1.52, 1.53, and 1.27 GeV/c. They used spark chambers consisting of four radiation lengths of lead and an annular ring of neutron detection counters at a laboratory angle of 24 deg with respect to the beam line. In their first experiment they measured the time of flight of the neutron, but did not fit the entire final state. Instead, they observed if they had a four gamma event in the spark chambers and then looked at the time of flight distribution of

the neutrons, in essence doing a missing mass experiment for four gamma events. This prevented them from observing $\Delta(1238)$ background. They did observe a narrow resonance at a dipion mass of 700 MeV and a width of 50 MeV. They did not observe it in their subsequent experiment.

Deinet et al.[27] observed the $n\pi^o\pi^o$ final state in a cubical array of spark chambers and a system of neutron detection counters, monitoring the neutron time of flight as well. However, they did not fit the entire final state doing only a missing mass experiment for four gamma events. Again, as in the case of the first experiment of Feldman et al., this prevented them from observing the $\Delta(1238)$ content of the final state. Their data was consistent with a resonance near the ρ mass with a width of 300 MeV.

In the third category fall the second experiments of Feldman et al.[28] and Sonderegger et al.[26] and a bubble chamber experiment of Besinger et al.[29] studying the interaction $\pi^+ n \rightarrow \pi^o\pi^o\rho$.

Feldman et al.[28] repeated their first experiment but added more neutron counters so that the neutron detection system consisted of two annular rings at 20 and 40 deg. They then did a kinematic fit of the entire final state with two constraints (not measuring the energies of the gamma rays). They found that their distributions were consistent with a large $\Delta(1238)$ contribution and a $(\pi^o\pi^o)$ resonance centered at 715 ± 3 MeV with a width of 150 ± 150 MeV. However, this fit was based on only 250 events that passed the two constraint fits, out of an initial 113,000 triggers.

Sonderegger et al. repeated their first experiment, adding a set of 32 neutron counters and an LMN polarized target. They then attempted a 6C fit to the data, assuming the target to be a stationary proton. Because of large background effects, they analyzed the $n\pi^o\pi^o$ state for

asymmetry due to the polarization of the target only.

An experiment using tantalum plates in a hydrogen bubble chamber for gamma conversion has been done by Besinger et al.[29] in an attempt to observe the $p\pi^o\pi^o$ final state. They however were unable to extract phase shifts successfully from their data because of low statistics and poor gamma detection efficiency. In addition they observed only a small contribution of $\Delta(1238)$ to the final state.

In summary, there exists disagreement on the measured values for $\delta_o^o(s)$ in the region below 1 GeV of the dipion mass, and there is a large discrepancy as to the amount of $\Delta(1238)$ present in the $n\pi^o\pi^o$ final state. It would appear that an experiment observing the interaction $\pi^- p \rightarrow \pi^o\pi^o n$ with high statistics and good resolution would resolve these problems.

II. DESCRIPTION OF EXPERIMENT

A. General

The production reaction $\pi^- p \rightarrow n\pi^o\pi^o$ was studied at the Bevatron of the Lawrence Radiation Laboratory at Berkeley. A π^- beam varying in momentum from 1.6 to 2.4 GeV/c in 0.2 GeV/c steps was incident on a liquid hydrogen target 20 cm long. The beam cross-section was defined by a three counter beam telescope, while the direction of each incident beam particle was defined by a set of scintillation counter beam hodoscopes. Beam contamination of μ^-'s and e^-'s was monitored by a threshold Cerenkov counter (see Fig. 4).

A neutral final state was assured by anticoincidence counters surrounding the hydrogen target that vetoed any interaction in which charged particles were observed.

The gamma rays from the decays of the two π^o's were detected by photographing the showers produced by their conversion into electron-positron pairs in the lead plates of the spark chambers. The spark chambers contained seven to eight radiation lengths of lead and formed five faces of a cube surrounding the hydrogen target. The non-interacting beam particles and the neutrons had to pass through the spark chambers. Gamma detection counters, constructed of lead scintillator sandwiches, and placed in the upstream face of the cube, detected gamma rays escaping the spark chamber volume in this direction. In this manner 3.7 π steredians were sensitive to gamma detection. The energies of the gamma rays were estimated by counting the number of sparks observed in each chamber and comparing this number with empirically determined curves.

The neutron was detected by 20 large scintillation counters, and its time of flight measured, the first beam counter defining the timing origin. The neutron detection counters were placed roughly in a semicircle 15 ft

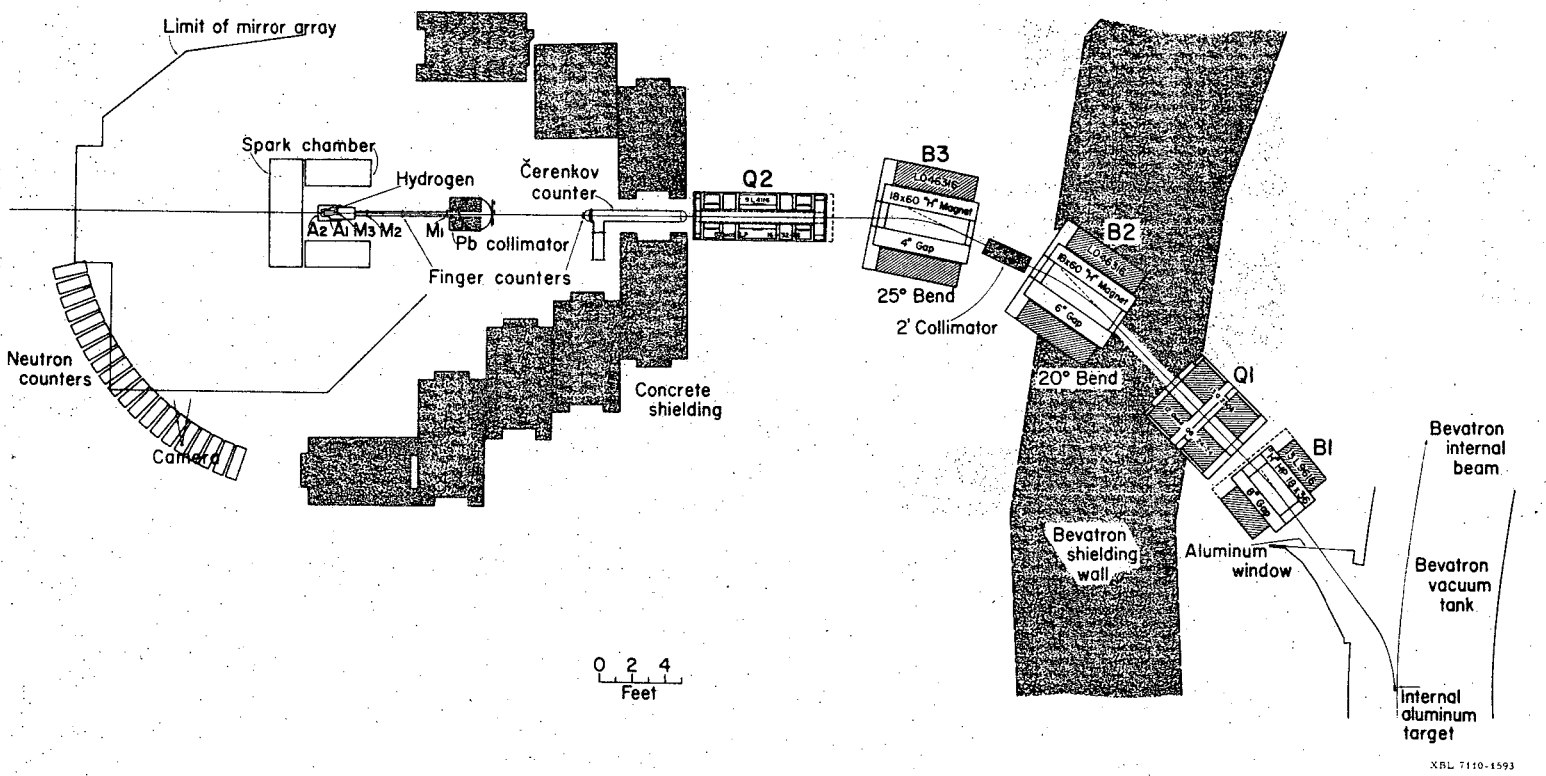

Fig. 4. The experimental setup for the investigation of the reactions $\pi^- p \rightarrow n + (\text{neutrals})$.

from the center of the target, such that they covered a region of 12 to 72 deg of the neutron production angle in the laboratory.

Each of the neutron counters had a veto counter in anticoincidence in front of it to prevent any charged particle triggers that could result from electron production by gamma ray conversion in the spark chambers surrounding the target. The veto counters also prevented charged particle triggers in the more unlikely case of neutron interactions in the lead plate spark chambers producing charged particles that could escape the chamber volume.

An acceptable event which triggered the spark chambers consisted of the beam counters in coincidence with the neutron counter signal, and no count in either the target or neutron counter antis. The neutron time of flight also had to lie within a predetermined timing gate approximately 100 nsec wide.

Possible neutral final states which have sufficient cross-section to be non-negligible at these π^- energies are

$$\pi^- p \rightarrow \pi^o n$$
$$\eta n$$
$$\omega n$$
$$\eta'(960) n \quad \text{(if the } \eta' \rightarrow \gamma\gamma \text{ decay mode exists)}$$
$$\pi^o \pi^o n$$
$$\pi^o \pi^o \pi^o n$$
$$\pi^o \pi^o \pi^o n$$

All the mesons in these final states decay so rapidly that they do not emerge from the target and only the reaction

$$\pi^- p \rightarrow n + \gamma\text{'s}$$

can be observed. Thus an $n\pi^o\pi^o$ final state was observed as a neutron and four gammas in the final state. Background events to the $n\pi^o\pi^o$

final state arise if not all the γ's from the events that have more than four gamma rays in their final state are observed ($3\pi^o$'s, $4\pi^o$'s, etc.) or if a single shower is counted as more than one shower in events that have fewer than four gamma rays in the final state (ω, π^o, η).

In this experiment all the four gamma events at all momenta were kinematically fitted to the hypotheses $\pi^- p \rightarrow \pi^o\pi^o n$ using the kinematic fitting program SQAW.[30] Since the four momenta of all the particles in both the initial and final state are known, a six constraint fit was obtained. The resulting kinematically fitted events were then fit to various theoretical models using the maximum-likelihood maximization program OPTIME.[31]

1. Feasibility Studies

The deployment of the neutron counters was motivated by the desire to get as large a spread of the invariant mass of the dipion system around a central value of 700 MeV as possible. Also it was desired to get as high a mass of the dipion system as possible. This meant that at least 60 deg of the polar angle had to be subtended by the neutron counters in the laboratory, and that the first neutron counter should be placed as close to zero degrees as practical. It was decided that 20 cylindrical neutron counters 8-in. in diameter placed at 15 ft from the hydrogen target would satisfy the requirements (with this geometry each neutron counter subtended approximately three degrees in the lab with a timing resolution of 2/3 nsec). The relative timing error, $\Delta t/t$, would have been improved by increasing the distance of the counters from the target, but this lowered both the solid angle subtended and polar angle subtended in the lab by a single counter necessitating a larger number of counters to cover the same kinematic region. The kinematics of dipion production in the reaction $\pi p \rightarrow \pi^o\pi^o n$, for a beam momentum of

2.4 GeV/c, have been displayed in Fig. 17a (page 85a) both as a function of laboratory production angle and c.m. production angle. The neutron counter cylindrical geometry was chosen because of the existence of well-tested programs to calculate their detection efficiency for this geometry.

The size of the hydrogen target was chosen to maximize the interaction rate along with good resolution of the interaction point. It was found by Monte Carlo studies that, given the directional resolution of the neutron counters and the showers in the spark chambers, an 8-in. long target did not significiantly alter this resolution when compared to that obtained for a 4-in. target. However, when even larger targets were contemplated (12-in. for example) it was found that the resolution did get substantially worse. Hence an 8-in. long cylindrical target, 4-in. in diameter, was chosen.

The maximum beam momentum, and hence obtainable dipion mass, was dictated by the physical layout of the experiment. The large lead plate spark chambers were already in position when the experiment was being planned, and hence the beam line had to be such that beam could be brought to the chamber volume from the Bevatron. It was found that with the beam elements available at the Bevatron, 2.4 GeV/c was the highest beam momentum that could be obtained.

It was decided to conduct the experiment at five different beam momenta to investigate the possibility that the dipion amplitude was a function of the three body final state center of mass energy. It usually had been assumed in most theoretical discussions that this was not the case.

B. Apparatus

Much of the detailed description of the apparatus employed in this experiment has already been presented elsewhere.[32] It is included in this write-up for completeness.

1. The Beam

The π^- secondary beam was collected from an aluminum internal travel target in the Bevatron of dimensions 1/4-in. vertically, 1/2-in. horizontally, and 10-in. along the internal circulating proton beam direction. Aluminum was selected as the target material to try to minimize the electron contamination of the beam resulting from gamma ray conversion within the target which resulted from the decay of π^o's produced within the target. In addition aluminum has a high cross-section for π^- production for the purposes of this experiment. The field values of the beam elements (see Fig. 5) were predetermined using the program OPTIK[33] and were within the expected errors of the final settings.

The beam line could be divided into two halves at the momentum defining slit (S1). The beam was taken from the target at zero degrees, was steered into the first quadrupole doublet (Q1) by a bending magnet (B1). The quadrupole doublet focussed the beam on the momentum defining slit, located between two H magnets (bending magnets). The first of these H magnets (B2), run with a 6-in. gap, did some momentum selection before the momentum slit, and bent the beam onto the brass collimating slit. The second H magnet (B3), which had a 4-in. gap, completed the momentum selection. The final focus on the hydrogen target was achieved by a quadrupole triplet (Q2).

The beam line through the second and third bending magnets, defined upstream of the H magnets by the axis of the quadrupole doublet and

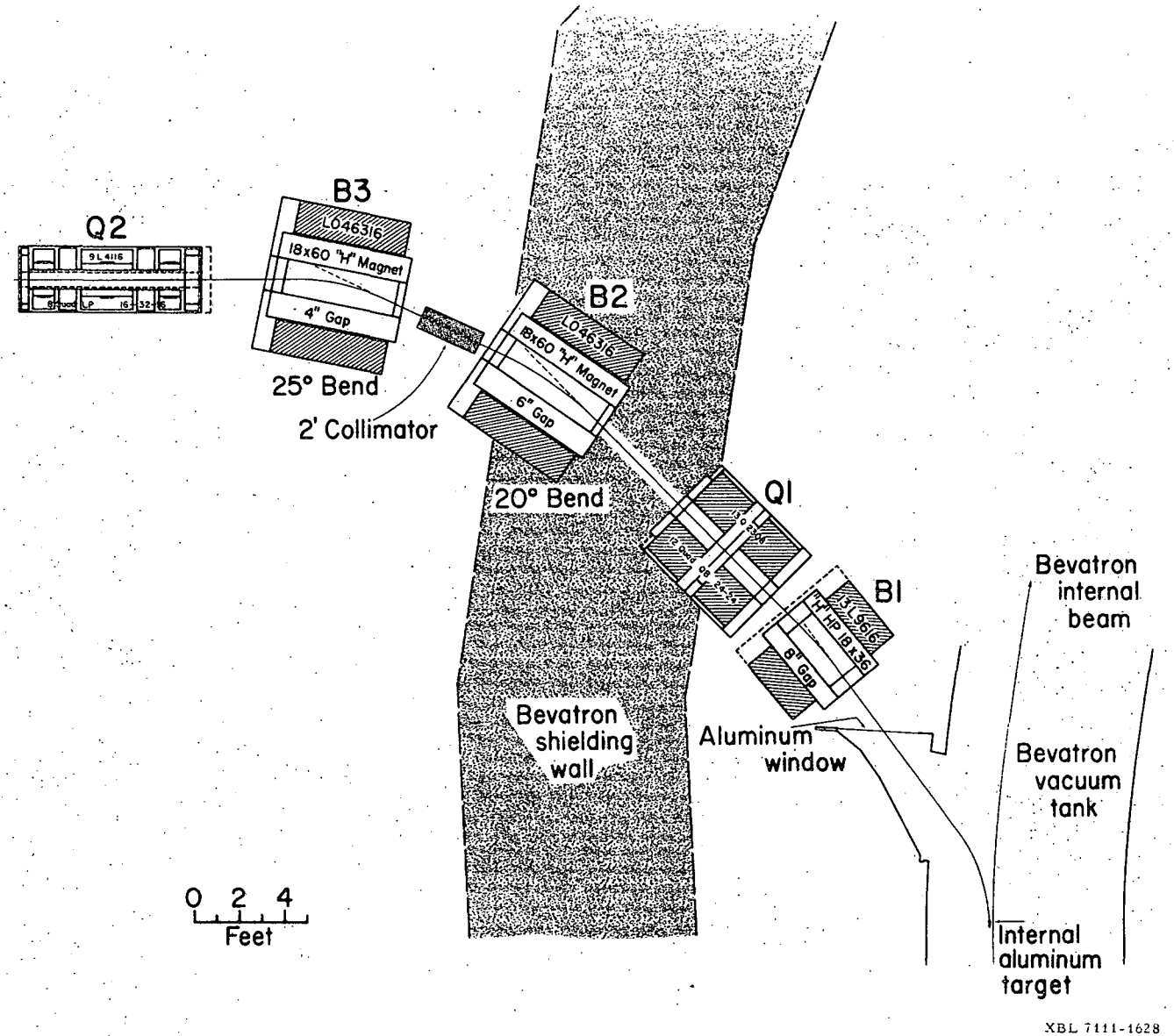

Fig. 5. The π^- beam line.

downstream by the axis of the quadrupole triplet was wire orbited for the five central momenta of the experiment, such that the beam line passed through the center of the momentum defining slit. Each of the H magnets was wire orbited individually, this measurement agreeing very well with that obtained when the two magnets were wire orbited in tandem. A 4 by 4 in. lead collimator was placed downstream of the final triplet but well before the hydrogen target to minimize the beam halo.

The μ^- and e^- beam contamination was monitored through out the experiment by a threshold Cerenkov counter. The complete beam composition was also measured at the outset and the finish of the experiment. It was found that the electron contamination was 8.5%, 5.6%, 4.6%, 3.0%, 2.3% while the μ contamination was 2.6%, 2.0%, 1.0%, 0.8%, 0.5%, at 1.6, 1.8, 2.0, 2.2, and 2.4 GeV/c respectively.

Beam profile studies indicated that the angular divergence of the beam was less than $\pm$ 1 degree. The momentum dispersion was $\Delta p/p = \pm 0.015$. To minimize small angle multiple scattering the beam was run through a helium bag system for most of the beam path. The final beam cross-section at the target was roughly elliptical in shape, such that the area, within which the beam intensity was half of its maximum value or greater, had a major axis, horizontally, of 3 in., and a minor axis, vertically, of 1/2 in.

The average beam intensity was 250×10^3 pions per second during a Bevatron spill ranging from 0.8 to 1.2 seconds. Roughly 25% of the beam particles were vetoed by electronics designed to render the data collection independent of the beam rate (see the section on electronics). As a result the net useable flux was of the order of 190×10^3 pions per pulse. The data taking rate was about two pictures per Bevatron pulse.

2. The Cerenkov Counter

The Cerenkov counter consisted of an aluminum cylinder 72-in long and 8-in. in diameter, with explosively formed domed aluminum entrance and exit windows 3/64-in. thick. Inside the cylinder, at a distance of about 12-in. from the downstream face of the counter was placed an aluminized Mylar mirror, 1/4-mil in thickness and inclined 45 deg to the axis of the tube. The Cerenkov light produced by an incident beam particle would be reflected by the aluminized Mylar mirror through a 3/4-in. thick quartz pressure window into a single Amperex XP1040 5-in. photomultiplier tube placed in contact with the window and run at a positive high voltage. The counter, except for the domed windows, was completely lined with Alzac to aid in the light collection efficiency of the counter. It was filled with Freon 12 (CCl_2F_2) and was run at pressures ranging from 0 to 50 psig. During data taking the Cerenkov counter was run at pressures of 32, 22, 18, 14, and 6 psig for a beam momentum of 1.6, 1.8, 2.0, 2.2, and 2.4 GeV/c respectively.

A schematic of the Cerenkov counter has been displayed in Fig. 6.

3. Liquid Hydrogen Target

The liquid hydrogen target was a cylinder of 0.0075 in. Mylar, 8.0 in. long and 4.0 in. in diameter. The flask was placed in an evacuated jacket of 0.030 in. spun aluminum, the beam passing through entrance and exit windows of 0.01 in. Mylar. A long pipe was connected to the re-enforced upstream end of the aluminum jacket. It served to support the target and the counters surrounding it, as well as containing the delivery lines of liquid hydrogen to and from the Mylar flask.

The re-enforced section of the aluminum jacket had a re-entrant hole of 4-in. diameter, allowing the placement of the last beam counter unusually near the liquid hydrogen flask. This counter (M3) consisted of

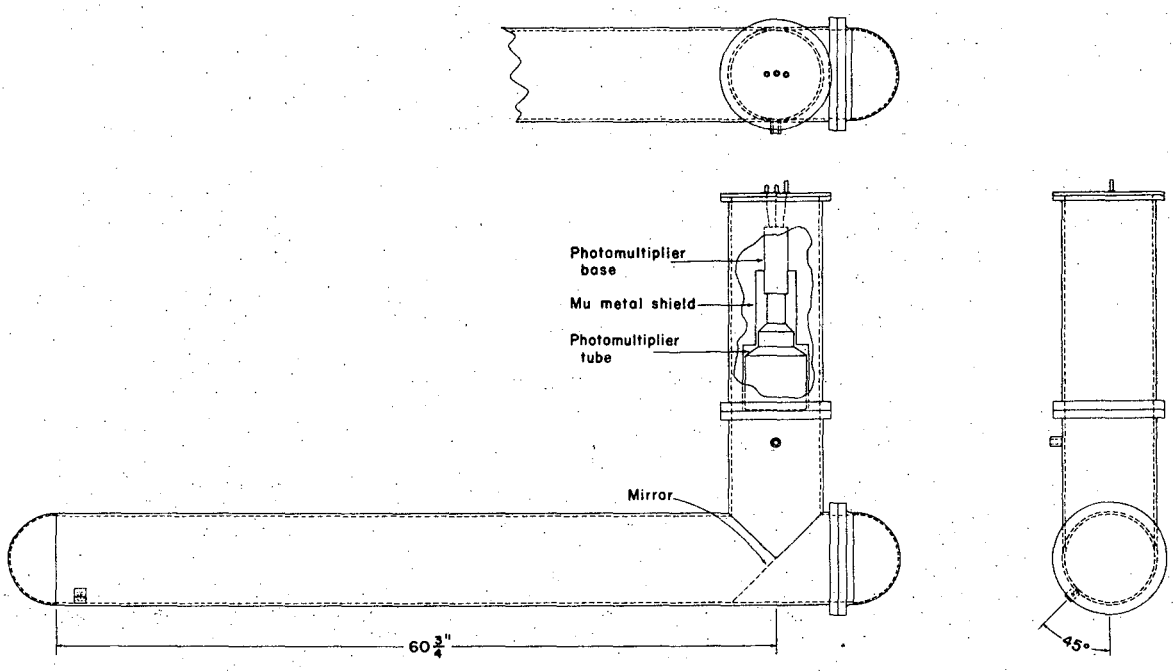

Fig. 6. Schematic of the Cerenkov counter.

a scintillator mounted 1.7-in. from the flask and an air light pipe through which the beam passed. (See Fig. 7.)

Beam particles could scatter in the last beam counter, the Mylar walls of the hydrogen flask, and the Mylar windows of the aluminum jacket, as well as the hydrogen contained in the flask. Counting rates with and without hydrogen in the flask were measured. Defining the ratio R

$$R = \frac{(\text{Counting rate without hydrogen})}{(\text{Counting rate with hydrogen})}$$

it was found that for the process $\pi^- p \rightarrow$ (neutrals), R ranged from 0.11 to 0.12. If it was required that a neutron was detected as well, this ratio increased, presumably, because of room background, and ranged from 0.13 to 0.16 as the incident π^- momentum changed from 2.4 GeV/c to 1.6 GeV/c.

4. Spark Chambers and Optics

The spark chambers and optics were constructed for a prior experiment. A complete description of the physical layout can be found in the published reports on that experiment.[34] The spark chamber pulser and discharge gaps have also been described elsewhere.[35]

There were five spark chambers, each forming one face of a cube, which enclosed a free volume of approximately one cubic meter and which contained the liquid hydrogen target. Each spark chamber was viewed in orthogonal stereo. A system of 46 mirrors brought all 10 views to a single Flight Research camera. An array of data lights and a clock recording PST were also included in the photograph.

Each of the four side chambers contained 42 lead and 12 aluminum plates of dimension 4 by 5 ft. The back chamber contained 48 lead and 13 aluminum plates 6.5 ft. square. These plates were separated by

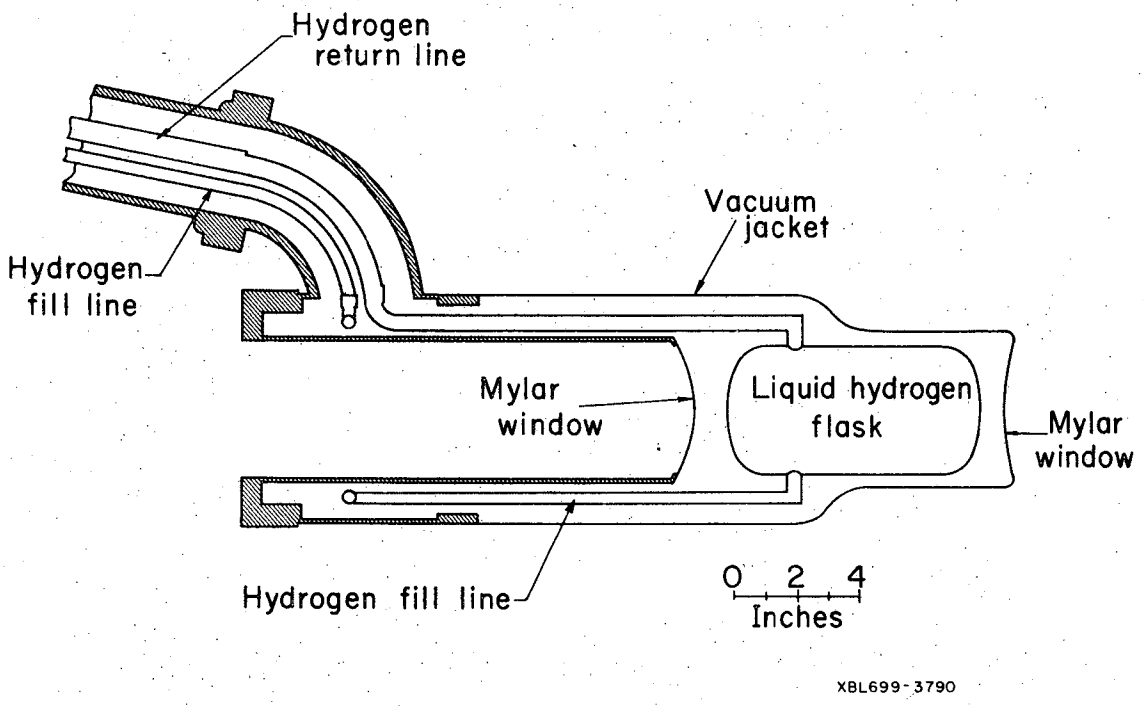

Fig. 7. The hydrogen target.

optically clear Lucite frames with a gap spacing of 5/16-in. The lead plates were in reality a lamination of 1/32-in. lead between two sheets of 1/64-in. aluminum. Because of the use of such very thin lead plates, the detection efficiency for low energy showers was quite high. The threshold for detection was $E_\gamma \approx 10$ MeV, while the probability of detection for E_γ of 20, 40, 60 and 80 MeV was 0.35, 0.75, 0.90, and 0.95 respectively. However the use of such thin plates meant that a large number had to be used to achieve the desired radiation length of ~ 7 in the side chambers, and ~ 8 in the back chamber.

Because the detection efficiency for a single photon was high, the number of photon events having j-gammas in the final state that would be observed as k-gamma events, where k was less than j (because the missing gamms failed to convert in the lead plates of the spark chambers), was relatively small. (The process of a j-gamma event being detected as a k-gamma event, $k < j$, because some of the photons failed to convert will be called feed-down.)

The first five plates of each chamber were 3/64-in. aluminum. The probability of gamma rays converting in this region was very small, since it constituted a total thickness of only 0.07 radiation lengths. It was thus possible to assure that a particle with a visible track in the first four gaps of the chamber was charged. Especially in the back chamber, this aided in the elimination of electron showers produced by the electron contamination in the beam. It also aided in the identification of old non-interacting beam tracks passing through the back chamber.

Figure 8 shows the arrangement of the five spark chambers in space and on film, while Figs. 14a,b (pages 56a,b) show an actual photograph of a good four shower event.

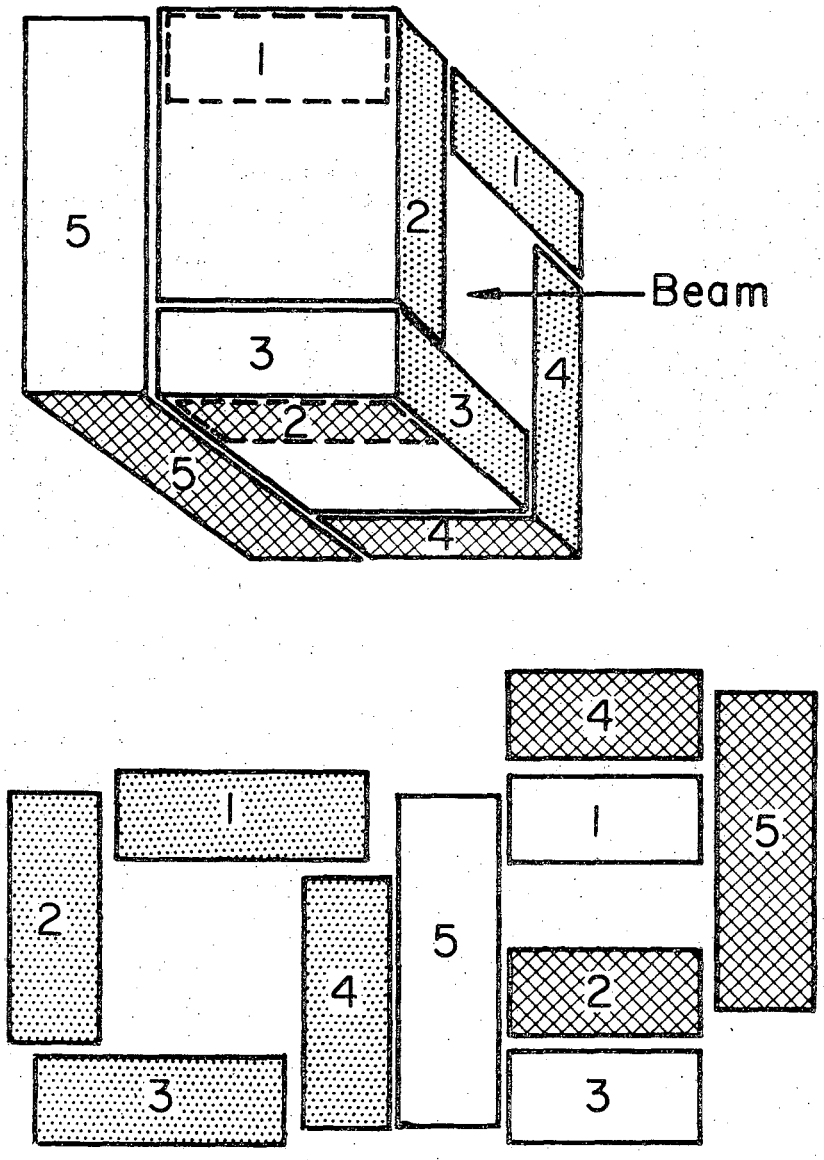

XBL699-3788

Fig. 8. The arrangement of spark chambers in space (top) and the arrangement of the spark chamber views on film (bottom).

5. Scintillation Counters

All scintillation counters were made from "Pilot B" scintillator consisting of polyvinyltoluene doped with p-terphenyl and p, p'-diphenylstibene.

The beam defining counters (M1, M2, M3) and the anti-coincidence counters surrounding the hydrogen target (A1, A2) were all viewed by RCA8575 photomultiplier tubes, and, all, except for M3, had twisted Lucite strip light guides. Since M3 was very close to the hydrogen target, being physically buried in the target jacket structure, the pion beam had to pass through its lightguide. For this reason, the light guide was an air filled cylinder of aluminized Mylar, with thin (0.0005 in.) 45-deg mirrors, also of aluminized Mylar, reflecting the light to a photomultiplier tube outside the beam region (Figs. 9, 10).

Each of the three beam defining counters was a plane disc of descending size, defining the convergence of the beam onto the target. The counters M1, M2, and M3 were 4.0, 3.5, and 3.0 in. in diameter respectively. M1 was 1/2-in. thick producing a pulse of good stability for timing purposes, while M2 and M3 were each 1/16-in. in thickness to minimize scattering.

A beam hodoscope system of two arrays of eight scintillators each, arranged in four by four banks, was also included. The eight scintillators were 1/8-in. thick, the dimensions of the upstream counters being 1.5×6 in. while those of the downstream counters $3/4 \times 3$ in. They were used to define the direction of the beam, but were not required in the beam trigger. Physically they straddled the beam counter M1.

The veto counter surrounding the hydrogen target (A1) was a 1/4-in. thick hexagonal cylinder viewed by three tubes (Fig. 10), while the

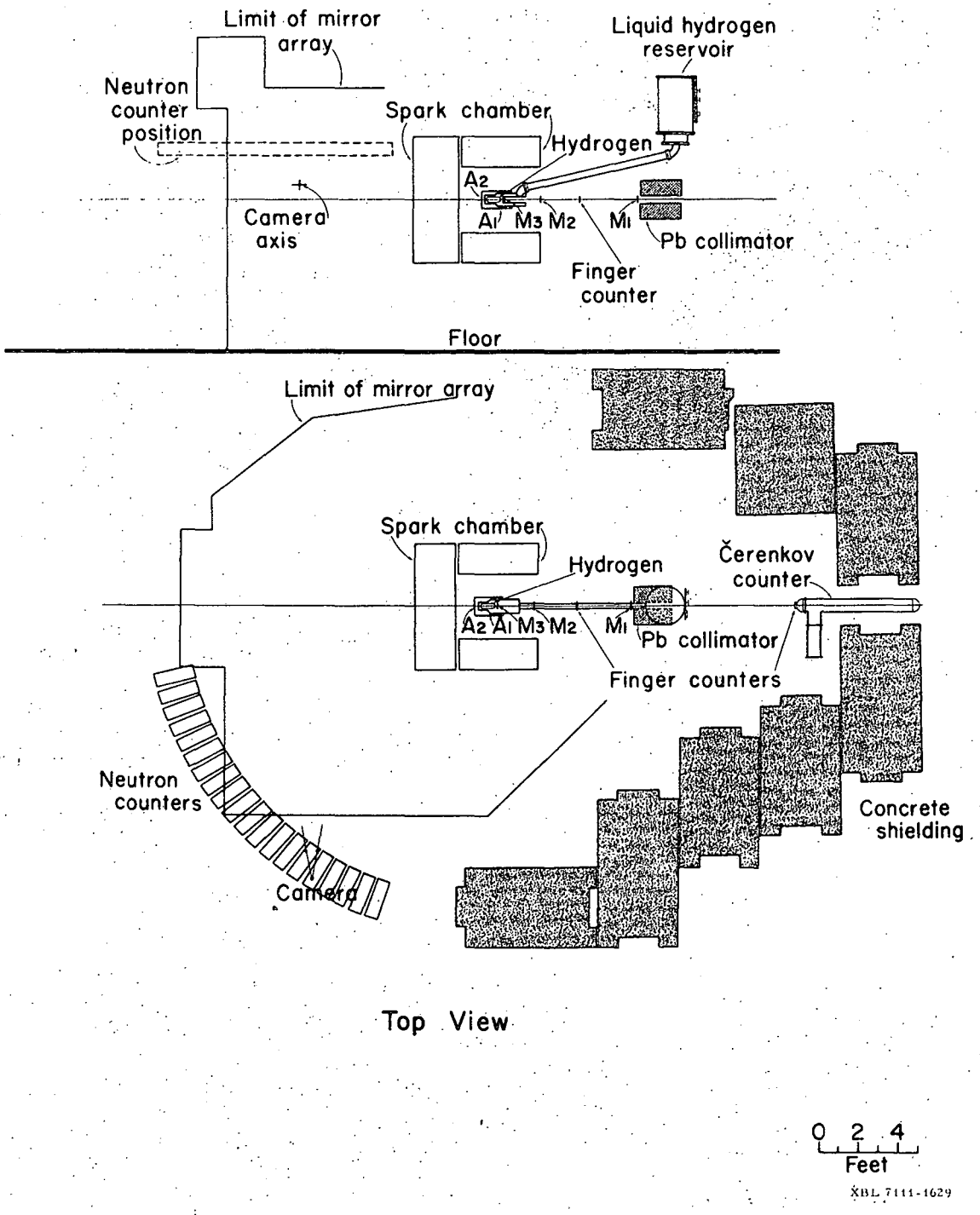

Fig. 9. The experimental layout.

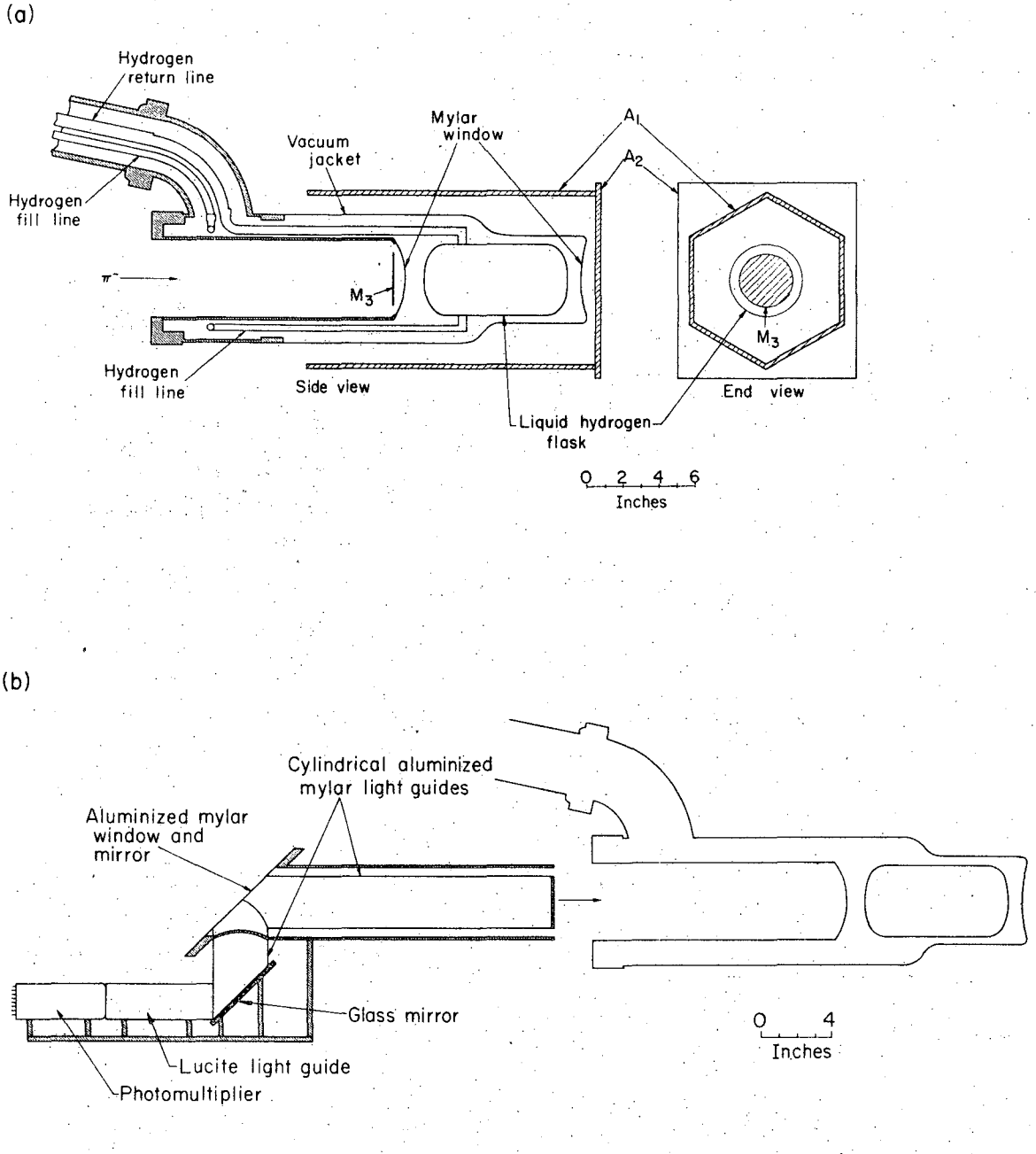

Fig. 10. The hydrogen target, veto counters, and the beam defining counter M3.

veto counter downstream of the target (A2) was an i-in., 1/4-in. thick, square. The veto system was more than 99.9% efficient since the neutral counting rate with the target empty was of the order of 0.03% of the beam rate.

The neutron counters (N_i) were cylinders of scintillator 8-in. in diameter and 8-in. long. Amperex XP1040 photomultiplier tubes (5-in. in diameter) viewed the scintillator through truncated cones of Lucite Fig. 13a, page 45a). The entrant face of each neutron counter was covered by a 10-in. square scintillation counter (V_i) viewed by twisted light pipes and either Amperex 56 AVP's or RCA 6810A's.

Four gamma ray detection counters, partially covered the open upstream face of the spark chamber system (G1 - G4). Each was a multi-layer sandwich of 1/4-in. sheets of scintillator alternating with 1/8-in. sheets of lead. There were eight such rectangular sheets of each material. The dimensions of each of the counters were G1 = 5.5 × 20 in.; G2 = 26 × 12.5 in.; G3 = 7 × 20 in.; G4 = 25.5 × 12 in. G2, G3, and G4 were each viewed by two Amperex 58 AVP's placed directly in contact with the smallest side of the sandwich, while G1 used a single photomultiplier similarly mounted. These tubes were 5-in. in diameter. The exact position of each of these counters has been shown in Fig. 11.

The gamma ray detection counters were calibrated to respond to a minimum ionizing particle passing through any one of the eight sheets of scintillator. During the calibration proceedure, each of the four counters was placed in the pion beam so that the pions were normally incident on each of the scintillator sheets. The counter was then plateaued with the signal attenuated by a factor of eight at the discriminator input. In normal operation the attenuation was discarded and the counter responded to 1/8 of the energy deposited by a minimum

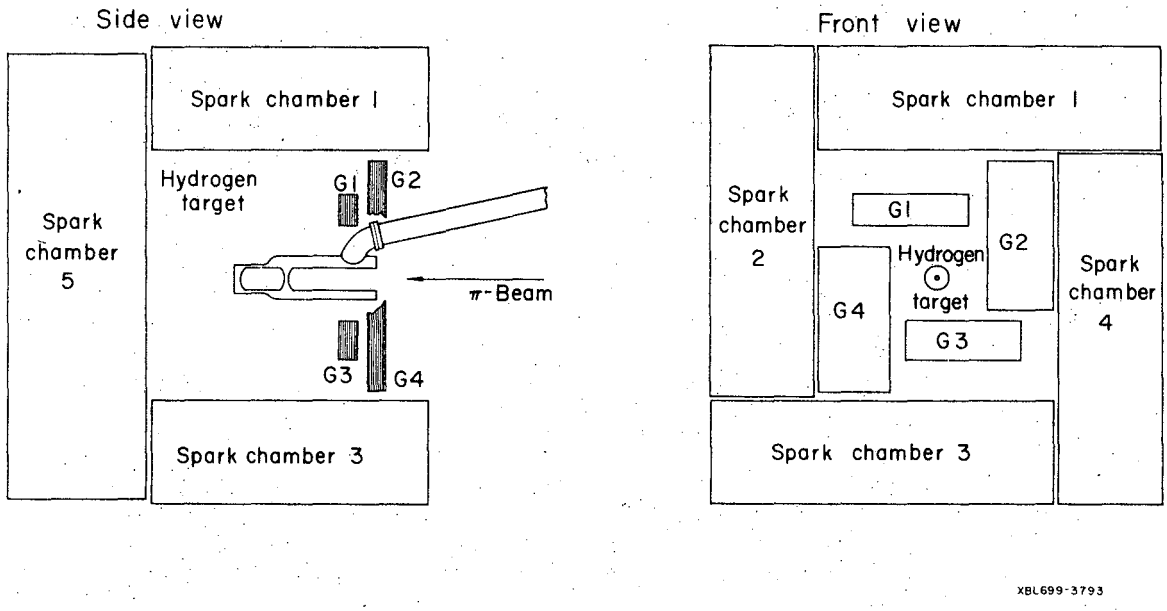

Fig. 11. The arrangement of spark chambers, hydrogen target, and gamma ray detection counters G_i.

ionizing particle travelling through eight sheets of scintillator.

6. Electronics and Trigger Logic

The first coincidence required was denoted by B (for beam) in Fig. 12 and was a simple triple coincidence between M1, M2, and M3. The timing was such that the output of the coincidence unit was determined by M1 and the beam particle timing was as accurate as the timing of M1 ($\pm$ 0.25 nsec).

The signal from B was then fed into a second coincidence unit M (for monitor) where it could be vetoed by a DT (for dead time) pulse. The DT signal was generated from the M1 output pulse and was designed to prevent jamming of the system by beam particles too closely spaced in time. To accomplish this, M1 generated a pulse in a special no dead-time discriminator, DT1, 52 nsec earlier than in the regular M1 discriminator. One output of DT1 was delayed and then used to trigger a similar unit DT2. The outputs of DT1 and DT2 were then added, and when appearing at the input of M, they constituted the DT signal. This pulse began 67 nsec before M1 (at M), ends 2 nsec before M1, resumes 2 nsec after M1 has terminated, and persists for another 600 nsec. Each B signal was thus accompanied by its own early and late DT signal which was used as a veto at the M coincidence unit. It could not eliminate itself, but it would veto beam particles nearly coincident in time. This arrangement prevented the jamming of electronics at the experimental beam rates, reduced the possibility of finding beam tracks in the back chambers, and lowered the rate of accidental triggering.

The rate independent output of M was fed into another coincidence unit, G0, where the target veto counters were in anticoincidence (A = A1 + A2). The output of this unit represented a "neutral final state"--a reaction in which a beam particle, suitably spaced in time,

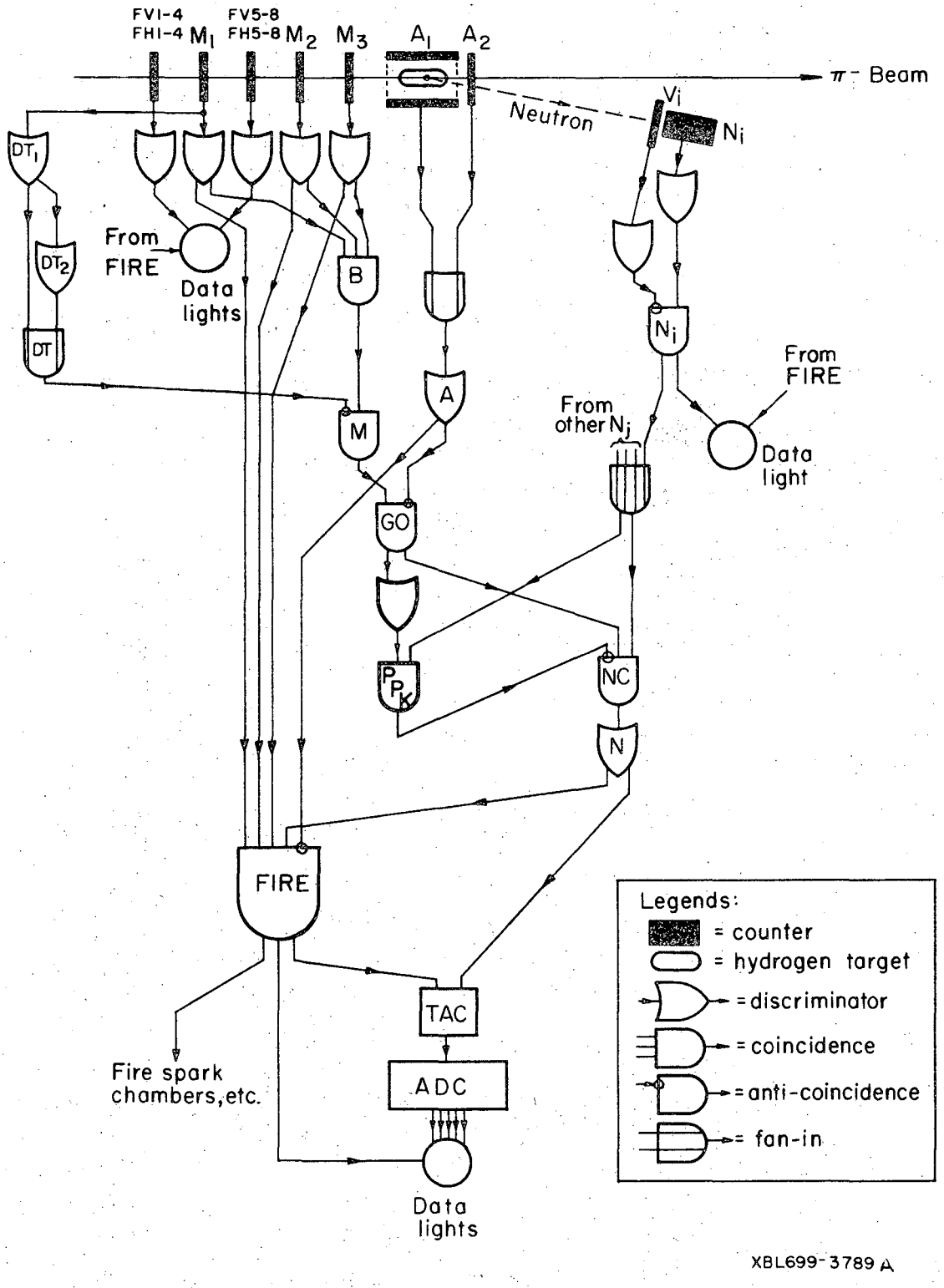

Fig. 12. The electronics.

entered the target region and no charged particles emerged.

In addition to the "neutral final state" signal, a signal from at least one of the neutron counters in anti-coincidence with its own veto counter was necessary to trigger the spark chambers. The neutron counter signal had to satisfy certain timing criteria as well. The coincidence between GO and the neutron counter signal was labelled NC (for neutron counter). The GO pulse was 140 nsec wide at this unit and arrived well before the neutron signal, thus preserving the neutron timing at the output of NC.

Another signal, logically equivalent to GO, was clipped to a width of four nsec, and suitably delayed, was used in coincidence with (ΣN_i) at PPK. The 27 nsec wide PPK output pulse was then used in anticoincidence at NC to veto events for which $\beta = 1$ particles (gamma rays) may have triggered the neutron counters. The use of the coincidence-anti-coincidence combination ensured that no slewing in timing would be observed. The PPK (for Prompt Peak Killer) was effectively used to reduce the number of background events. The time region of the time of flight spectrum before the prompt peak represented neutron events having $\beta > 1$, and, consequently, had to be accidental background. These events were recorded and photographed for possible use in data analysis.

The output pulse from NC was all that was logically required for triggering the spark chambers. In practice, however, the signal from NC went to another discriminator, N, (for neutron) to be stretched into a signal of length suitable for time-to-amplitude converter (TAC). The TAC determined the timing from the overlap of two long ($\geq$ 100 nsec) pulses. In addition to N it had to receive a signal, such as B, representing the timing of the beam. For this purpose, a circuit paralleling B and called FIRE was used. FIRE consisted of a fourfold coincidence between M1, M2, M3, and N, with A in anti-coincidence. It

had its timing determined by M1 and was logically equivalent to N or NC. FIRE, rather than B, was used for the beam timing in order to avoid extraneous "start" pulses to the TAC. The TAC determined the timing difference between FIRE, which preserved the timing of M1, and N, which preserved the timing of the individual neutron counter.

The FIRE unit performed a variety of tasks: (1) it fired the spark chambers, the fiducial lights, the event number lights, and the data light array, (2) it advanced the camera, (3) it provided one signal to the TAC, and (4) it initiated an 80 msec gate to shut the whole system down during pulsing and recovery of the spark chambers, (5) it provided interrogate pulses for various bits of information to be displayed on the data light array.

The TAC output went to an analog-to-digital converter (ADC) where it was transformed into a binary number appearing on the data light array. The TAC and ADC had a minimum time resolution of $\pm$ 0.17 nsec.

The data light array displayed the frame number in binary form, which neutron counter fired, the ADC number (the time of flight of the neutron in arbitrary units), which gamma detection counter had fired (if any), which beam hodoscope counters had fired, as well as an indicator, if a FIRE signal had been given to the chambers, if the frame in question was the first of a series of events for a particular beam spill, and a parity light (to maintain the parity of the data light array always even). The data lights were Xenon flash lamps. When a counter or some other informational signal was in coincidence with FIRE the pertinent light was enabled. Each time the spark chambers were fired, all the enabled lights would receive a high voltage pulse and were flashed, thus recording them on film.

7. The Neutron Counters

The neutron counters detected the neutrons indirectly--scintillation light being produced only when the neutron interacted with a nucleus in the scintillator and produced a charged recoil. Such recoils varied greatly in energy and hence the amplitudes of the photomultiplier pulses had a broad range. A description of the physical construction of the counters has been presented in the section on scintillation counters.

In this experiment, pulse shape stability of the neutron recoils was achieved by providing a tapered voltage divider in the photomultiplier base, thus avoiding space charge shielding with the growing electron cloud as it cascaded from dynode to dynode. There then was little distortion of the pulse shape.

The concept of "zero crossing" was used to obtain accurate neutron timing, independent of the amplitude of the photomultiplier pulse. The anode signal was delayed by 6 nsec and was added to an inverted and attenuated (6 db) signal from the 14th dynode of the photomultiplier. The addition was done by a passive mixer composed of 24 ohm resistors and HP2303 hot carrier diodes, the latter being present to limit the position and negative excursion of the pulse without affecting the slope near zero. At the point of anode-dynode mixing, there was also added a -100 mV bias pulse from a THRESHOLD discriminator triggered by a second pulse from the 14th dynode. This combined pulse was fed into a second discriminator, the TIMING discriminator whose threshold was set at -120 mV, so that as the bipolar pulse, biased by a -100 mV, passed through - 120 mV, the second discriminator was triggered. The trigger point was 20 mV below the point of zero crossing, so that if the crossing slope was steep enough, it was independent of the amplitude of of the pulse.

The output of the THRESHOLD discriminator was also required in coincidence with the TIMING discriminator and anticoincidence with the neutron veto counter signal to constitute a valid neutron counter signal. The signals from the 20 neutron counters were then fanned in by a series of OR circuits to constitute a single input to the coincidence unit NC. (See Figs. 12 and 13b.)

In the experimental setup, the neutron counters were placed roughly in a plane 30 in. above the beam line, such that each of the neutron counters pointed towards the center of the target. Each counter was approximately 15 ft from target center and subtended and angle of 3 degrees. The neutron production angles covered by the neutron counters ranged from 12° to 72 deg in the laboratory.

Special care was taken to ensure uniform efficiency for neutron detection fro all neutron counters and to maintain this detection efficiency constant for the duration of the experiment.[32] The efficiencies were calculated using the program TOTEFF,[36] the calculation depending on the counter dimensions, the mean threshold for the detection of a neutron of minimum kinetic energy T_o, and the fractional resolution $J = \sigma/T_o$, where σ was the standard deviation of the minimum threshold setting. The calculated efficiencies were of the order of 20% $\pm$ 2% and did not depend on J very sensitively (see Fig.16b for the neutron counter efficiency as a function of the neutron kinetic energy).

The mean threshold was set uniformly for all counters to twice the maximum energy of the recoil electron (2.37 MeV) from the Compton scattering of 2.62 MeV gamma rays (obtained from the decay of an excited state of Pb^{208}, the end product of α and β decays beginning with the parent nucleus Th^{238}). The threshold setting was achieved by setting the THRESHOLD discriminator at the Compton edge of the 2.62 MeV gamma

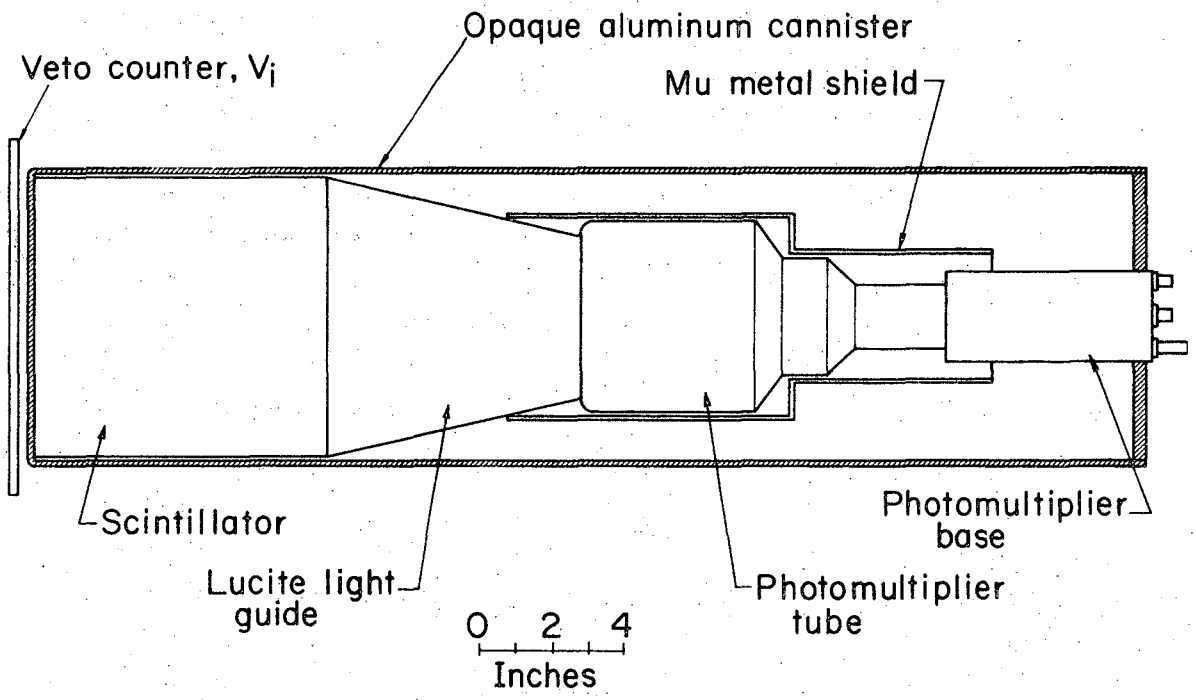

Fig. 13a. A neutron counter N_i.

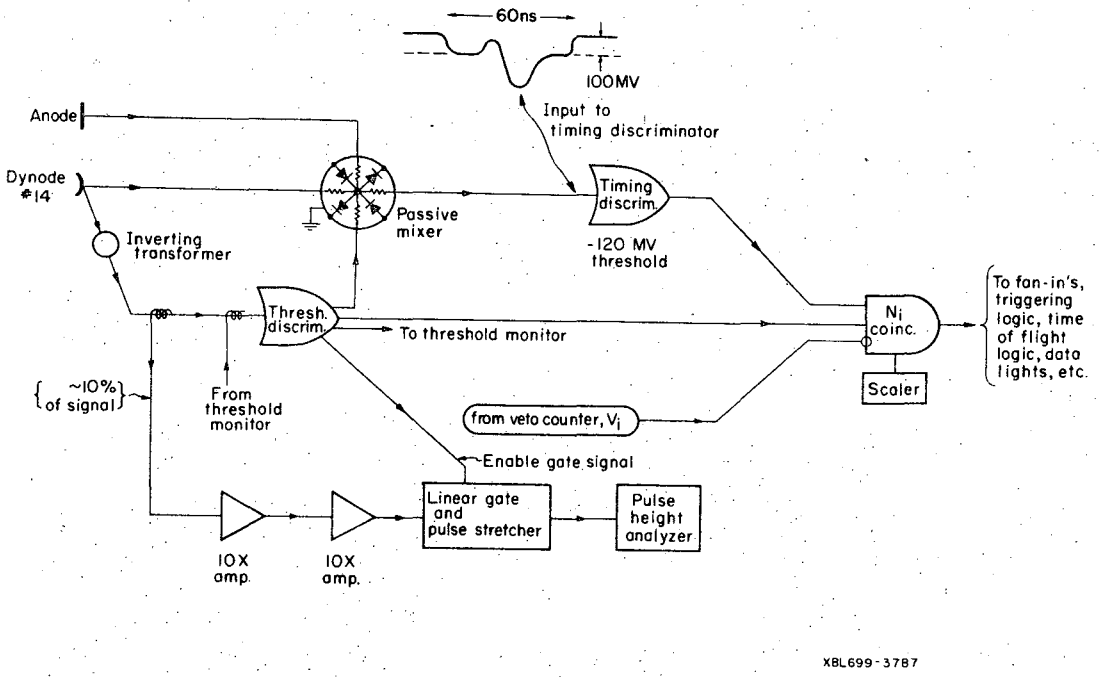

Fig. 13b. The neutron counter timing and calibration electronics.

rays and then attenuating the signal by 6 db at the discriminator output to raise the corresponding neutron detection threshold by a factor of two. It was found that the threshold had to be set at this level to prevent the accidental triggering of the neutron counters by low energy gamma rays.

Once the thresholds had been set for all counters, a secondary calibration was obtained by monitoring the counting rate when all counters were exposed simultaneously to a standard Th^{238} source. These counting rates were monitored at least once a day to compensate for fluctuations in the gain of the photomultipliers. These counting rates were then maintained at a constant level by slightly adjusting the threshold settings of the discriminators. This daily recalibration appeared to keep the thresholds to within $\pm$ 2% of their nominal values.

III. DATA COLLECTION

The experiment to investigate the reaction $\pi^- p \rightarrow$ (neutrals) was conducted at the Bevatron of the Lawrence Berkeley Laboratory. Data of the interaction were collected from October 29, 1969 to February 25, 1970. This period included approximately three weeks of shutdown of the Bevatron at the end of December of 1969 and at the beginning of January of 1970. Set-up time, before actual data collection commenced, took a period of two and a half months.

Data were taken with and without the neutron counter coincidence in the spark chamber trigger. The data without the neutron counter coincidence in the trigger were taken to obtain a complete sample of $n\pi^o$ final state events, which were mainly eliminated by the angular and PPk-timing cuts in the normal trigger mode. The comparison of the data for the two trigger modes in the case of the charge exchange interaction proved to be a very sensitive method for the calibration of systematic effects in the normal trigger mode data. The data without the neutron counter in coincidence in the trigger were also used to obtain the total $n\pi^o\pi^o$ cross-section to eliminate the angular cuts and timing cuts introduced by the neutron counter trigger requirements.

The amount of data accumulated at each momentum, with and without the neutron counter coincidence in the spark chamber trigger has been tabulated in Table 1. A total of 496×10^3 pictures were taken in this experiment, with 281×10^3 of the pictures being taken in the normal running mode and 215×10^3 of the pictures being taken in the neutral final state trigger mode (no neutron counter coincidence in the spark chamber trigger). The amount of data taken at each beam momentum, and the relevant normalization to the incident beam has been displayed in Table Ia. The amount of data that has been analyzed is presented in

Table Ia. Data accumulated.

	Normal				Neutral Final States			
	Target Full		Target Empty		Target Full		Target Empty	
	# of pictures	# of incident beam particles	# of pictures	# of incident beam particles	# of pictures	# of incident beam particles	# of pictures	# of incident beam particles
2.4	77.7×10^3	14.9×10^9	2.3×10^3	2.9×10^9	43.3×10^3	18.7×10^6	1.8×10^3	6.5×10^6
2.2	51.4×10^3	9.3×10^9	2.2×10^3	3.0×10^9	40.8×10^3	15.3×10^6	1.7×10^3	5.5×10^6
2.0	55.8×10^3	10.2×10^9	1.8×10^3	2.4×10^9	45.1×10^3	15.4×10^6	1.8×10^3	5.5×10^6
1.8	56.7×10^3	9.6×10^9	1.7×10^3	1.7×10^9	38.5×10^3	12.3×10^6	3.5×10^3	8.9×10^6
1.6	30.0×10^3	4.2×10^9	1.3×10^3	1.2×10^9	37.6×10^3	10.7×10^6	0.8×10^3	1.8×10^6
Total	271.6×10^3		9.3×10^3		205.4×10^3		9.6×10^3	

Table Ib. Data analyzed.

	Normal				Neutral Final States			
	Target Full		Target Empty		Target Full		Target Empty	
	# of pictures	# of incident beam particles	# of pictures	# of Incident beam particles	# of pictures	# of Incident beam particles	# of pictures	# of Incident beam particles
2.4	62.0×10^3	12.0×10^9	1.7×10^3	3.1×10^9	18.0×10^3	7.8×10^6	1.8×10^3	6.5×10^6
2.2	37.3×10^3	7.2×10^9	0.9×10^3	1.2×10^9	19.2×10^3	7.2×10^6	1.7×10^3	5.5×10^6
2.0	32.8×10^3	6.1×10^9			17.9×10^3	6.2×10^6	1.8×10^3	5.5×10^6
1.8	31.7×10^3	5.6×10^9	0.8×10^3	0.8×10^9	17.9×10^3	5.7×10^6	1.3×10^3	5.5×10^6
1.6	26.9×10^3	3.8×10^9	1.2×10^3	1.1×10^9	17.7×10^3	5.0×10^6	0.8×10^3	1.8×10^6
Total	190.7×10^3		4.6×10^3		90.7×10^3		7.4×10^3	

Table Ib. It should be noted that data was obtained both with the target flask filled with hydrogen (477×10^3 pictures) and also with the target flask empty (18.9×10^3 pictures).

Tables Ia and Ib showed that 70% of the normal trigger data and 41% of the neutral final state trigger film had been analyzed.

A. Data Analysis

The film taken during the Bevatron experimental run of $\pi^- p \rightarrow$ (neutrals) was scanned and measured by the LBL Group A scanning and measuring staff. The data from the film that was taken without the neutron coincidence in the spark chamber trigger were used to obtain the total cross-sections for the reaction $\pi^- p \rightarrow \pi^o \pi^o n$. The normal trigger data (i.e. with the neutron counter coincidence in the trigger) were kinematically fitted and those events satisfying the $n\pi^o\pi^o$ final state hypothesis were examined and then utilized to obtain various parametrizations of the $n\pi^o\pi^o$ production amplitudes. The normal trigger data Dalitz plot was also compared to that of the neutral final state trigger data for consistency both in the case of the reaction $\pi^- p \rightarrow n\pi^o$ and $\pi^- p \rightarrow n\pi^o\pi^o$. This comparison represented a sensitive calibration of possible systematic effects which could affect the results, and yielded an empirical test of these effects as compared to the more usual approach of relying solely on Monte Carlo simulation.

The data on film were scanned by scanners who recorded the numbers of observed gammas in each frame (the number of showers in the chambers plus the number of gamma detection counters triggered). In addition, the scanners recorded the initial point of each shower in the spark chambers in terms of a coarse grid corresponding to a spatial resolution of 3 in. by 2 in. as well as the appropriate pairing of showers in the two stereo views of each chamber. The film was also processed automatically by the SASS system,[37] a precision cathode ray tube and photomultiplier system linked to a DDP-24 computer. SASS digitized the position of all sparks, fiducial lights, and data box lights for each frame and stored this information on tape via the program FLICKERS.[38]

The FLICKERS output tape information, in principle, could have

been used to reconstruct the showers in three dimensional space without any of the scanning information having been used. In practice, however, it was found, because of the very complex geometric configurations of multi-shower events (in the energy range of the experiment), that it was difficult to filter the FLICKERS output tape information to obtain sufficient accuracy in grouping the observed sparks into their corresponding showers without any additional information. However, by adding the scanning information on the grid parameter of the initial spark of each shower (appropriately specifying the pairing of the two stereo views), along with the total number of showers in each frame, it became relatively easy to reconstruct the gamma ray directions in three space. The LBL program DHARMA-HS[39] was developed for this purpose. This program, utilizing the scanning information, found the shower directions with an average error of $\pm$ 3 deg, as well as the location of the first spark of each shower with an error average error of $\pm$ 1 inch. The angular error arose mainly from the lateral spread of the shower, while the first spark error was due to an ambiguity in the selection of one of the sparks within the grid zone identifying the shower as the first one. Usually the spark closest to the target of the densest cluster of sparks within the grid zone was chosen. Some of the error also could be attributed to local optical distortions.

DHARMA-HS included a first order trapezoidal optical correction to take into account distortions due to the mirror-lens system in the final shower coordinates. The number of sparks in each shower, later used for energy estimates, was also obtained.

The geometric reconstruction and kinematic fitting of events from DHARMA-HS output was then performed by the LBL Group A bubble-chamber fitting program SIOUX,[40] suitably modified for the use in spark chamber-

counter experiments.

The status of each event was stored on tape, called the Master List, using the program SCALP.[41] On the SCALP output was recorded the progress of each event as it was scanned, digitized by SASS, measured by DHARMA-HS, and kinematically fitted by SIOUX. The SCALP tape also contained the data box information as obtained from the FLICKERS tape, as well as the scanning information. From the Master List one could also determine, for each frame number, the beam momentum, whether or not the hydrogen target was full, and whether or not the picture was taken with all the apparatus functioning properly.

It was the SCALP output tape that was used to obtain the total $\pi^o\pi^o n$ cross-section from the sample of data which was obtained without a neutron counter coincidence in the spark chamber trigger. From this data, for which the neutrons were produced for all azimuthal angles, the total cross-sections were obtained by counting the number of gamma rays (showers and gamma counters triggered) for each event.

On the other hand, it was the SIOUX output for the four shower events in the normal trigger data, that was used to obtain the parametrization of the $n\pi^o\pi^o$ final state. The parametrization was obtained utilizing the maximum likelihood fitting program OPTIME.[42]

The kinematically fitted data were observed to have peripheral behaviour, as would be expected if the reaction proceeded by simple exchange mechanisms.

The Dalitz plot projections, in addition, showed a large Δ (1238) contribution to the final state.

The analysis of the $\pi^o\pi^o n$ final state was first done with a cut in the invariant mass of the pi-neutron system corresponding to the $\Delta(1238)$ region (1100 MeV to 1300 MeV). This cut ensured that the final state

would contain a clean sample of $(\pi^o\pi^o)$ events which could easily be related to π-π scattering amplitudes. Fits to the observed final state data were then performed using one of the theoretical models discussed in Sec. I.A.7 which seemed to fit the data well.

The corresponding π-π phase shifts were extracted (this, by no means, ensured that the π-π phase shifts were meaningful but that, if the data was to be interpreted in terms of π-π scattering, they were the best parametrization of the data).

Finally the relative amount of $\Delta(1238)$ present in the final state was obtained. The $\Delta(1238)$ amplitudes and the π-π scattering amplitudes were assumed to add incoherently.

1. Film Scanning[43]

Each frame of film displayed two views of each of the spark chambers in orthogonal stereo as well as the data light array in the upper left hand corner. The orientation of the chambers in space and on the film has been shown in Fig. 8.

The scanner first recorded the gamma detection counter information (from the data light array) and extraneous charged track information (e.g. beam tracks or neutron recoils). He then scanned the frame for showers, pairing the two views of the same physical shower appropriately, and recording the coarse grid information for both views. Each shower record was annotated by one of the following coded statements (yielding more information about the shower):

a. The shower was "normal." That is, it began in the active region of the chamber (but not in the first four gaps defined by the aluminum chamber plates), had more than two sparks, and pointed towards the hydrogen target.

b. The shower converted in the corners between two chambers. Such

a shower could originate in the dead extremities of one chamber and first appear in another chamber (in this case there could be sparks in the first four gaps of the second chamber and the shower still be a valid one).

c. The shower had only two sparks.

d. The shower did not point to the hydrogen target.

e. The shower was probably a fragment of another shower rather than an independent one.

f. The shower was probably an old beam track fragment.

g. The shower was probably produced by the same photon which triggered a gamma counter.

In cases a, b, and g we would call the track observed a valid shower, the number of triggered gamma counters being added to the number of showers to obtain the total number of detected gamma rays for that event. In the special case of showers of type g the gamma detection counter responsible for producing the showers was not counted.

On the average the scanners showed good judgement in separating the showers into the seven categories, most events falling into categories a and b. Some difficulty in scanning was encountered, however, in the relatively unusual cases listed as d and g.

In particular, in the case of category d, too stringent a criteria was generally exercised in labelling showers as having "vertex problems," that is, not pointing towards the hydrogen target. Showers that first materialized in dead spaces of the chambers could have only a partial branch in an adjacent chamber which would not necessarily point towards the hydrogen target. Also showers that first materialized in gamma counters would not point towards the target for the same reasons. In addition the gamma detection counters themselves consisted of dead

regions (the support brackets) in which showers could have converted without triggering the gamma counters themselves, but would then enter the chambers, the observed sparks pointing towards the counters and not the target.

In the relatively rare case of showers triggering both the gamma counters and being observed in the chambers (3% of the data), it was found that if the gamma event was labelled as a "doubly-detected gamma," it was done so reliably. However, not many showers were thus labelled. It appeared that the scanners often failed to recognize cases where the gamma counter was triggered and that a shower detected in a chamber adjacent to the counter was associated with it.

In the case of f, the beam track was not, of course, associated with the event. Since the active time of the spark chambers was approximately 2.5 μsec, a beam pion (or muon), passing through the downstream chambers up to one μsec before the occurence of the event triggering the spark chambers, would appear as a very straight track with sparks in every gap. If such a beam particle passed 1.0 to 2.5 μsec before the triggering event, it would appear disjointed and dispersed, and could be interpreted as a forward produced gamma ray shower.

Thirty-five percent of the scanned film had a beam track passing through chamber five [~ 14% of the film having a "new" track (less than 1 μsec old), and 21% of the frames having an old track (1 to 2.5 μsec old)]. Three types of beam tracks were observed--non-interacting pions or muons (~ 52%), electrons (~ 22%), and pions which interacted in the spark chamber plates (~ 26%).

The non-interacting pions and muons produced straight well-defined tracks and were easily distinguishable from showers. The beam electrons caused showers in chamber five, these being well-collimated and passing

completely through the chamber for "new" tracks, but, again, being dispersed for "old" tracks. Here, the criterion, that valid showers could not materialize in the first four gaps of the chamber, proved quite valuable in discarding electron showers.

Approximately 60% of the interacting pions scattered elastically, the remaining 40% charge-exchanged. The latter events often consisted of a beam track abruptly ending in the chamber, with the resulting showers pointing back to the endpoint of the beam track. New charge-exchange tracks were easily recognized, while old and dispersed ones were harder to distinguish from target associated showers.

It was the old charge-exchange and electron shower tracks that caused the most difficulty in scanning, the only special feature of the tracks being the large splotchy and disjointed appearance of the sparks that constituted the tracks. Since old beam tracks occurred in a localized region in chamber five, they were well isolated by the scanners who exercised special care when scanning this region.

Showers with only two sparks (category c) were not counted. This meant that some genuine low energy gamma rays were not recorded; on the other hand, it prevented brehmsstrahlung produced gammas associated with the conversion of high energy photons from being considered as separate showers (often having "vertex problems"). The fact that true two spark showers were dropped could adequately be compensated by the feed-down corrections applied to the data.

Figure 14 shows a typical four shower event. Figure 14a shows it as it was recorded on film, while Fig. 14b had the spark chamber boundaries superimposed. The shower labelled as (2) in Fig. 14b converted in the lucite between chambers 3 and 4 and was a good example of a corner shower.

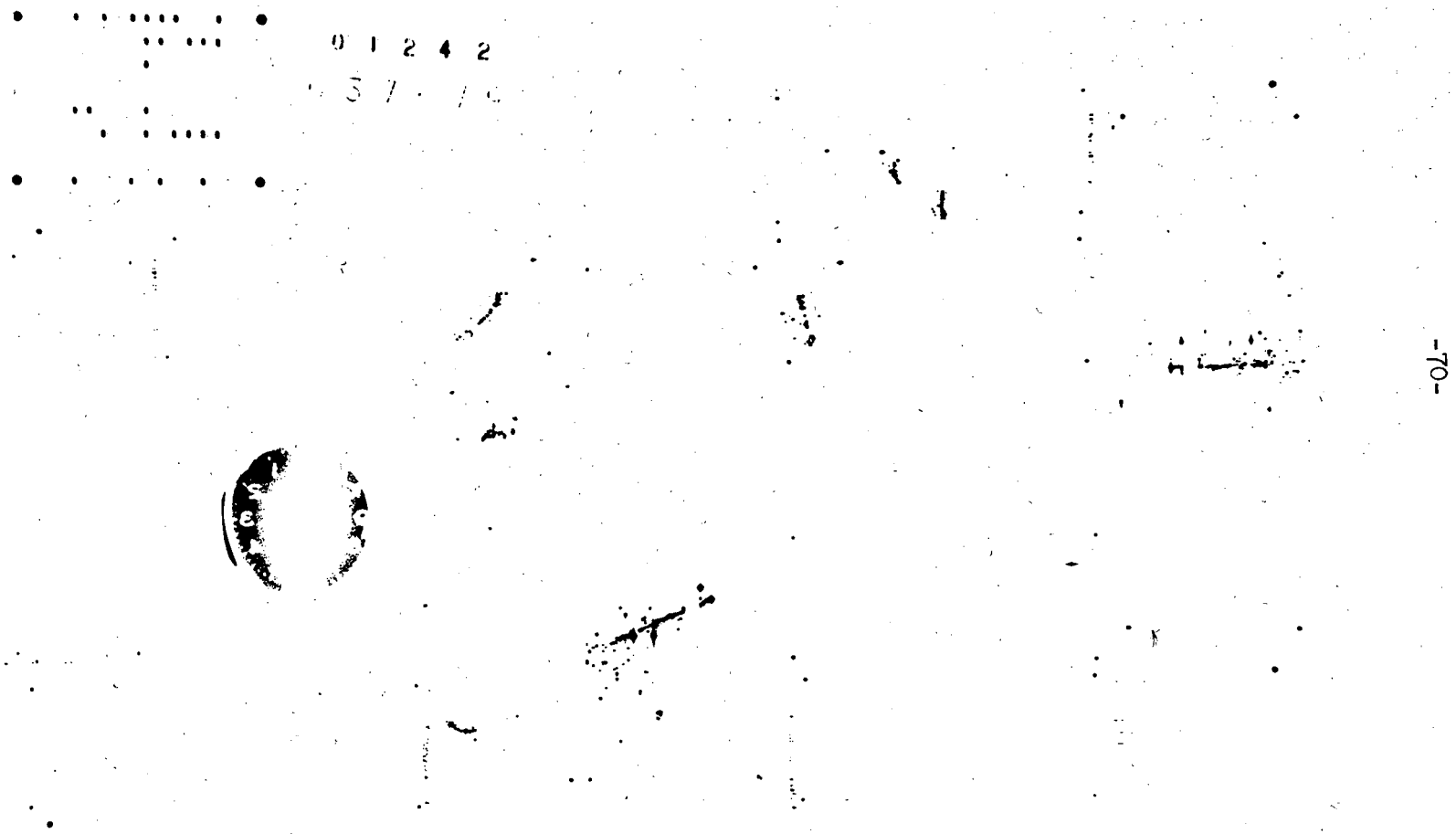

Fig. 14a. A typical four shower event as recorded on film.

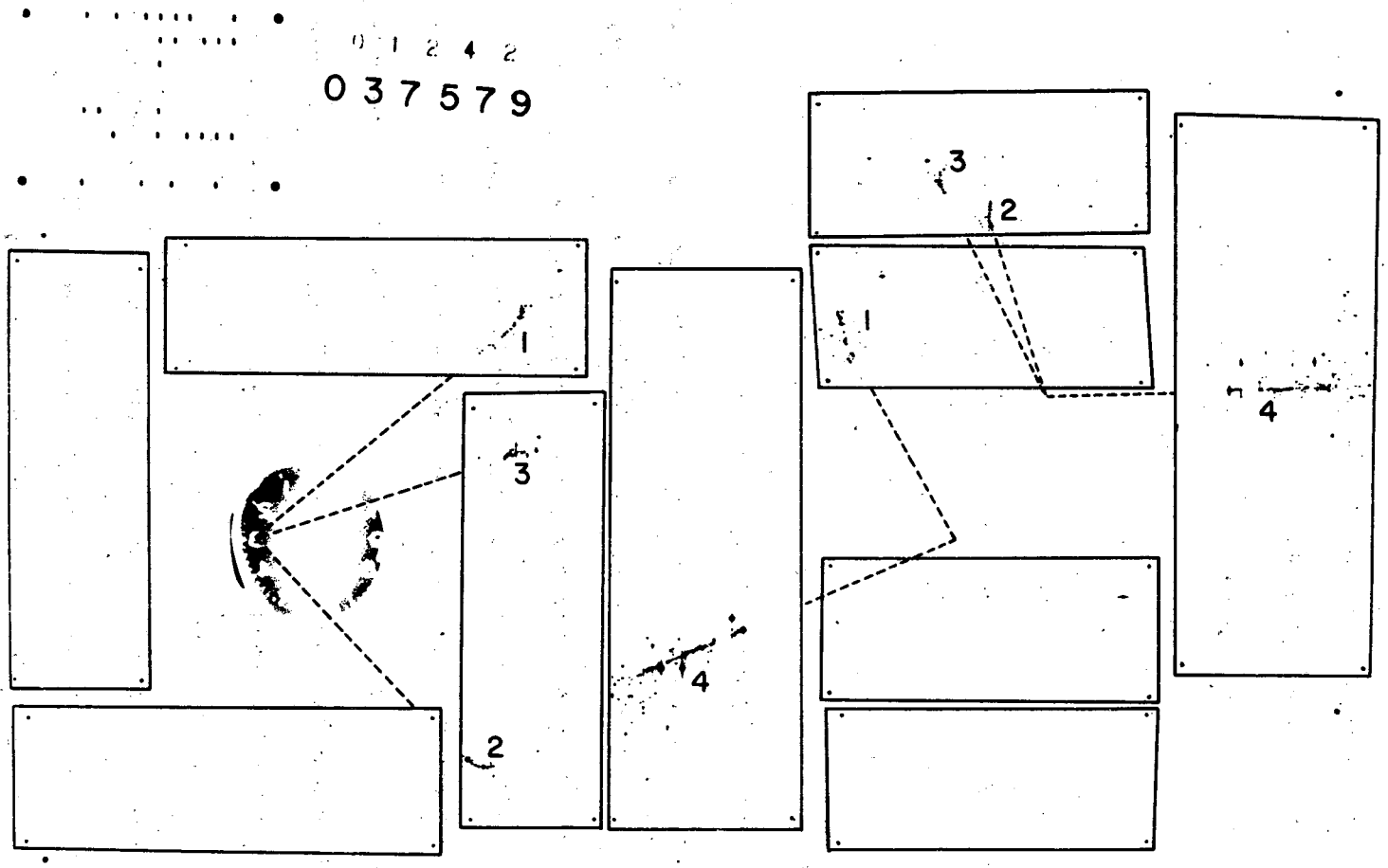

Fig. 14b. The same four shower event as in Fig. 14a with the spark chamber boundaries superimposed. The interaction point and gamma ray trajectories have also been displayed in each view.

2. Scanning Efficiency and Corrections

Two rolls at each of the incident momenta were independently triple scanned. To determine the scanning efficiency for the experiment, three of these triple scanned rolls were also scanned by the most competent of the scanners as well as a sample cross-checked by a physicist in an attempt to resolve the discrepancies among the three sans. (This so-called conflict scan was done for normally triggered data and data without the neutron counter coincidence requirement.) If all three scans (excluding the conflict scan) agreed on the number of showers, their type, and their grid locations, the event was considered to have been correctly scanned. If a conflict appeared between any two of the three scans for a given event, that event was scanned for the fourth time and an attempt was made to resolve the discrepancy among the previous three scans and to define, within the scanning criterion, a correct scan.

It was found that the largest discrepancies in scanning arose in mislabelled grid zones (adjacent ones being confused) and, less often, mislabelled chamber number. As long as the grid labels were not incorrect by more than a zone, the measuring program DHARMA-HS could still locate the shower correctly in the chambers, thus introducing little error in the analysis in this case. Mislabelled chamber number, however, lost the event completely.

A much more important discrepancy arose if the triple scans disagreed on the number of gamma rays present. This disagreement occurred at the 10% level for the low multiplicity showers but became as high as 35% for events having six or more showers in the final state. In scanning a true j-gamma event (i.e. an event with (j-g) showers in the chambers and g triggered gamma counters) the scanner would generally observe the proper number of gamma rays. If he failed to observe the

correct number of gamma counters that had triggered, the SASS system would invariably pick them up from the film, so that in all cases it was in the shower misidentification that the wrong number of gamma events would be entered on the Master List. Some fraction of the time the scanner would fail to notice one or two showers and the event would appear as a (j-1) or (j-2) gamma event on the Master List. Similarly, the scanner could mistake one or two old beam track remnants as showers and the Master List would show a (j + 1) or (j + 2) gamma event. Thus, given a true j-gamma event, there was a probability E_{ij} that, after scanning, it would be recorded on the Master List as an i-gamma event. Hence

$$S_i = E_{ij}T_j$$

where S_i was the recorded number of i-gamma events on the Master List, while T_j was the true number of j-gamma events. It was the matrix E_{ij} that was obtained from the conflict scan.

Defining n_{ij} to be the number of true j-gamma events as established by the conflict scan which had been recorded by the scanner as an i-gamma event, one obtained

$$S_i = \frac{n_{ij}}{\sum_i n_{ij}} T_j$$

so that

$$E_{ij} = \frac{n_{ij}}{\sum_i n_{ij}}$$

It should be observed that the columns of E_{ij} were normalized to 1. The normalization could be easily understood if it were realized that if there were T_j true j-gamma events, the number of j-gamma mis-scanned events plus the number of j-gamma correctly scanned events had to add up to T_j. In addition

$$\Sigma S_i = E_{ij}T_j = \sum_j (\sum_i E_{ij})T_j = \Sigma T_j$$

and the total number of observed events equalled the total number of true events. This equality expresses mathematically the fact that in this experiment every event was scanned, and there was no possibility of losing an event, only misreporting it.

The scanning efficiency matrix has been displayed in Table II.

The event matrix, n_{ij}, from which the scanning efficiency matrix was obtained has been displayed in Table III. It proved useful in the estimation of possible background for the fitted data as well as for the calculation of the scanning efficiency.

To obtain the true number of j-gamma events, one solved the matrix equation

$$T_j = E_{ji}^{-1} Si$$

To obtain the error in the estimation of T_j, one wrote

$$S_i = E_{ij} T_j$$

and differentiated

$$\delta S_i = \delta E_{ij} T_j + E_{ij} \delta T_j$$

yielding $$E_{ij} \delta T_j = \delta S_i - S E_{ij} T_j$$

Making the assumption $$\langle \delta S_i \delta E_{jK} \rangle = 0$$

One finally obtained

$$\langle \delta T_K \delta T_j \rangle = E_{iK}^{-1} \langle \delta S_K \delta S_\ell \rangle + Tm^2 \langle \delta E_{Km} \delta E_{\ell m} \rangle E_{j\ell}^{-1}$$

The error in S_K was assumed to be purely statistical, so that

$$\langle \delta S_K \delta S_\ell \rangle = S_K \delta_{K\ell}$$

To obtain the error $\langle \delta E_{Km} \delta E_{\ell m} \rangle$ one considered n_m true events being distributed with some probability e_{Km} into a finite number of bins. One standard deviation away from having $e_{Km} n_m$ events (no summation over m) in bin K was then given by $e_{Km}(1 - e_{Km})/n_m$. This was taken to be the

Table II. The scanning probability matrix E

Observed number of gamma rays	True number of gamma rays									
	0	1	2	3	4	5	6	7	8	9
0	.944	.066	.003	.002	.002	.003	.002	.005	.003	.005
1	.040	.871	.033	.007		.001	.001			
2	.001	.056	.939	.124	.012	.005				
3		.004	.024	.820	.099	.024	.006		.008	
4		.003	.002	.042	.857	.243	.056	.023	.005	
5	.007			.003	.026	.675	.196	.088	.018	
6	.003			.001	.003	.047	.696	.327	.120	.033
7						.003	.037	.509	.272	.087
8							.006	.050	.533	.273
9							.001		.041	.601

Table III. The event matrix n_{ij}. (Note that the average of three scans was used for the observed number of gammas.)

Observed number of gamma rays	True number of gamma rays									
	0	1	2	3	4	5	6	7	8	≥ 9
0	61.0	8.7	3.3	1.3	2.3	1.0	1.3	0.7	.3	.3
1	1.3	160.7	52.0	.3	.3	.3	.3			
2	.7	13.0	1631.3	121.6	18.0	2.7	.7			
3		.7	41.7	755.3	148.7	14.0	2.3		1.0	
4			3.0	41.0	1382.0	133.3	23.3	.3	.7	
5	.7		.7	2.7	43.7	377.0	94.3	14.3	3.3	
6	.3			.7	5.7	29.3	331.0	50.3	17.0	1.7
7					.3	1.3	20.7	83.0	36.7	6.0
8							2.3	7.3	76.7	22.0
≥ 9							.7	.3	6.3	51.0

error for bin K. To obtain the correlation terms between e_{Km} and $e_{\ell m}$ one considered the sum

$$e_{Km} + e_{\ell m} + e = 1$$

Following the usual techniques of differentiation, squaring, and averaging one could obtain

$$\langle \delta e_{Km} \delta e_{\ell m} \rangle = - \frac{e_{Km} e_{\ell m}}{n_m}$$

So that finally

$$\langle \delta E_{Km} \delta E_{\ell m} \rangle = \frac{1}{n_m} \langle e_{Km} \delta_{K\ell} - e_{Km} e_{\ell m} \rangle$$

This calculation yielded errors for the diagonal terms of the efficiency matrix between 1 and 2%.

3. Gamma Ray Detection Efficiency and Corrections

Once the scanning efficiency correction had been obtained the sample T_j of true j-gamma events did not necessarily represent the true number of j-gamma events produced by the beam in the target.

There was still a possibility that some individual gamma rays could have been counted as two gammas (legitimately within the scanning criteria) as well as that there were present a number of non-event associated (real) tracks in the chamber that looked like showers. Thus more gammas could be present after the scanning efficiency correction than were actually produced by the particular π-p interaction in the target. This process of observing extraneous gamma rays was termed feedup.

In addition, not all gamma rays produced in the interaction converted in the chambers or gamma detection counters. Thus a four shower event could be observed as a three shower event because one of the gammas failed to convert or was lost through the upstream opening in the gamma

detection equipment. The process of observing less gamma rays than produced by the beam particle interacting in the target was termed feed-down.

The feedup processes were considered first. There was a small but non-zero probability that showers could be observed from a previous event because of the long active time of the chambers (2.5 μsec). A study of this possibility had been made in a previous experiment with the same apparatus,[32] triggering the spark chambers randomly and normalizing this data by counting the number of accidental beam tracks. At the momentum and intensity of that experiment (716 MeV/c) it was found that there was a single shower in 2% of the frames, two showers in 0.5% of the frames, and three showers in 0.2% of the frames. Thus there was an accidentals feedup at the level of 2.7%. This effect, however, should have been beam energy and beam intensity dependent and therefore different at higher beam intensities and energies. Unfortunately, no film was taken in this mode at the higher beam momenta, preventing a study of the possible change in the number of observed showers in the chambers due to non-event associated tracks. The absolute number of extraneous tracks should have increased with the higher beam intensity, but decreased with the total scattering cross-section at the higher beam energies. Also the multiplicity ratios should have tended to favor larger numbers of extraneous showers in the chambers at the higher beam energies.

There was also the probability that within the defined scanning criteria there was room for misidentification of a j-gamma event as a $(j + 1)$-gamma event or $(j + 2)$-gamma event. These could result from a gamma ray triggering a gamma counter as well as being observed as a shower in the chamber and not being properly associated with the gamma

detection counter; a double gamma counter trigger--a gamma ray triggering two gamma counters; shower fragmentation--one "real" shower being considered as two showers; and, misidentification of old beam tracks at a level higher than could be corrected by the conflict scan. It was found impossible to correct any of these cases adequately, for, if they escaped detection in the conflict scan, it meant that they satisfied any reasonable criteria for a j-gamma event.

To further study the feed-up process the three and four gamma events were fit to the hypothesis $\pi^- p \rightarrow n\gamma\gamma$ and the π^o region studied in the $\gamma\gamma$ opening angle distribution. It was found that there was an enhancement above background in the three gamma events (see Fig. 15a) at the π^o opening angle, which also corresponded to the correct π^o mass and timing distributions. For four gamma events no such enhancement was found. The total number of events above background in the three gamma data was estimated to be 16% of the two shower events in the same region. The scanning efficiency event matrix showed that only 3% of the two shower events were mis-scanned as three showers (this ratio could be obtained from the fraction n_{32}/n_{22} of the event matrix n_{ij}) so that a large fraction of the three gamma events in the opening angle region were still unaccounted for. These events were rescanned and it was found that indeed, in most cases one of the showers appeared of dubious nature (an old track, a two spark shower, or possibly a charged track) which within the scanning criteria constituted a legitimate shower. This feed-up, however, appeared to be beam associated and hence a function of the beam intensity. It could not be interpreted to be a single shower appearing as two showers. Hence most of the events above background were attributed to constant feed-up per event. It was expected that this large feed-up would not be seen in the data taken without the

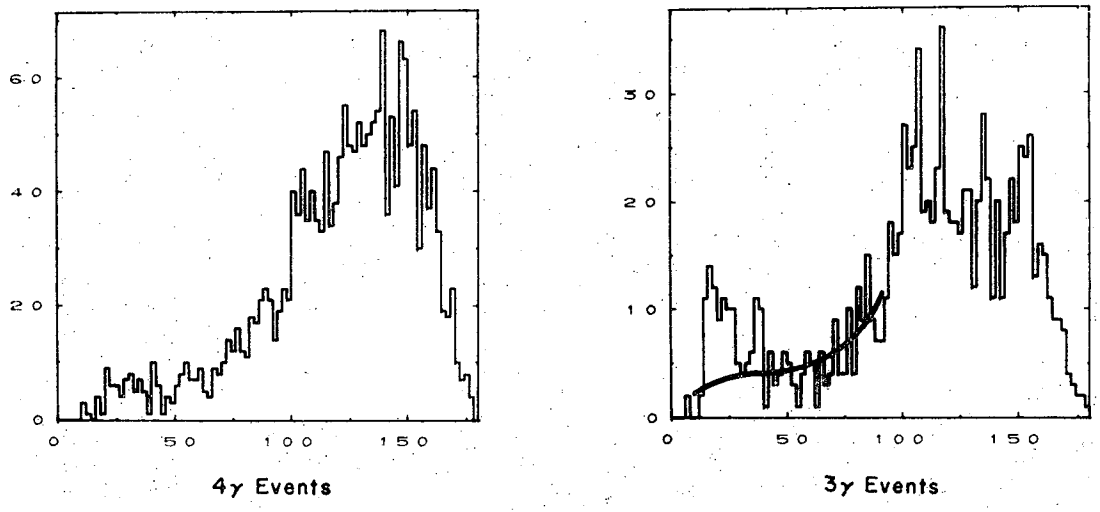

Fig. 15a.

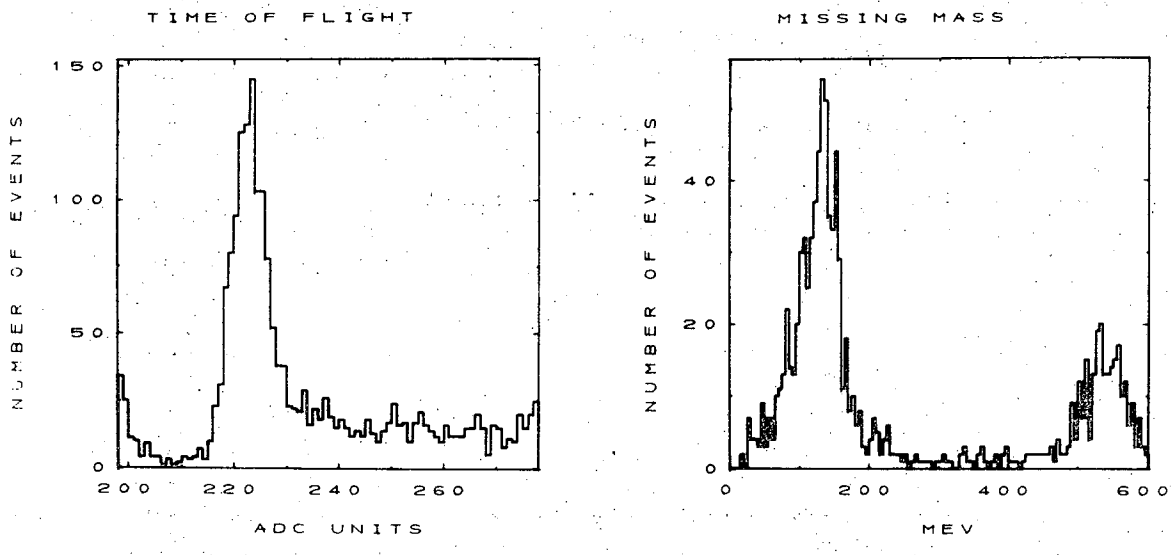

Fig. 15b.

Fig. 15c.

XBL 722-225

Fig. 15a. The opening angle distributions in the c.m. (in degrees) for four and three gamma events fit to the hypothesis $\pi^- p \rightarrow n\gamma\gamma$.

Fig. 15b. The time of flight distribution for two gamma events (no fits). One nsec is equal to 6 ADC units.

Fig. 15c. The $\gamma\gamma$ invariant mass for two gamma events fit to the hypothesis $\pi^- p \rightarrow n\gamma\gamma$. The π^o peak indicates a mass resolution of 20 MeV (half width).

neutron counter coincidence in the spark chamber trigger since these data were taken at much lower intensities (a factor of 10) than the normal trigger data.

Thus no estimate of feed-up per shower could be unambiguously determined from the low gamma multiplicity events. Since it was suspected that some of the feed-up was due to difficulties with the gamma detection counter triggers for high multiplicities the data was not inconsistent with a small feed-up of 0.5% to 1% per shower. This method of the feed-up depending on the shower multiplicities would reflect the fact that higher multiplicities also had a higher probability of triggering the gamma detection counters, being confused with old beam tracks, or appearing as unassociated fragments.

To correct for the feed-up due to non-event associated gammas, the matrix equation was formulated where S_i was the number of observed i-gamma events (after scanning corrections) and T_j was the number of j-gamma events associated with an interaction in the target. The matrix U_{ij} was displayed as

$$U = \begin{bmatrix} 1-(u_1+u_2) & & & & & & \\ u_1 & 1-(u_1+u_2) & & & & 0 & \\ u_2 & u_1 & & & & & \\ & u_2 & & & & & \\ & & \ddots & & & & \\ & & & 1-(u_1+u_2) & & & \\ 0 & & & u_1 & 1-(u_1+u_2) & & \\ & & & u_2 & u_1 & 1-u_1 & \\ & & & & u_2 & u_1 & 1 \end{bmatrix}$$

where u_1 was the probability of an event having one shower too many, while u_2 was the probability of an event having two showers too many.

If it was assumed that there was a non-zero probability per gamma ray that it would be seen as two gammas, then we again obtain the matrix equation

$$S_i = V_{ij} T_j$$

where

$$V = \begin{bmatrix} 1 & & & & & & \\ . & (1 - v) & & & & & 0 \\ . & v & (1 - v)^2 & & & & \\ . & . & 2v(1 - v) & & & & \\ . & . & (1 - v)^3 & & & & \\ & & & . & . & & \\ 0 & & & & & & \\ & & & & & (1 - v)^{n-2} & 0 \\ & & & & & 1 - (1 - v)^{n-2} & 1 \end{bmatrix}$$

The entries in the nth column and $(n + m)$-th row of V is just the mth term of the binomial expansion of $[(1 - v) + v]^{n - 1}$. The final row of V is the sum of the previous entires in the appropriate column subtracted from 1. The term was interpreted as the probability of observing an n-gamma event as an $(n + k)$-gamma event.

Thus by applying the scanning efficiency corrections and the feed-up corrections, the statistical gamma multiplicity distribution of target associated events as really existed in the chambers, could be obtained. However, this did not as yet represent the true gamma-multiplicity distribution produced in the target because of showers not converting in the chambers. Therefore the last correction to be made, was for feed-down of events into lower gamma multiplicity categories.

Two approaches could have been used to determine feed-down. An elaborate Monte Carlo program existed[44] taking into account the spark

chamber geometry and a detailed semi-empirical model for shower production. The program could have been used to determine the amount of feed-down of the various gamma multiplicities.

The second approach assumed that (1) there was some (unknown) average gamma ray detection efficiency, d, and (2) that the probability of a single gamma not being detected, (1 - d), did not depend on what happened to the other gammas. In this case the probability of detecting n gammas when m were produced could be given by

$$D_{nm} = \frac{m!}{(m - n)!n!} d^n(1 - d)^{m - n} \qquad n \leq m$$

$$D_{nm} = 0 \qquad n > m$$

The first assumption always had to be true since it was only the fraction of gamma rays detected. The second, on the other hand, was only approximately true, for if some of the gamma rays were to escape upstream, then the remaining ones would certainly have a smaller probability of doing so. However, if the probability of detection were large, then the relationship for D_{nm} would also be a good approximation for the feed-down correction. The Monte Carlo calculations for feed-down also agreed well with the binomial coefficient estimates.

It was found that the shower detection efficiency could be estimated at 89% per shower agreeing closely with the results obtained in a previous experiment using the same apparatus.[32] It was found however, that for charge exchange ($\pi^- p \rightarrow \pi^o n$) the production distribution of the gammas was sufficiently different from the other higher gamma multiplicity production mechanisms that a feed-down of only 5 to 6% had to be used to explain the observed ratio of two to one shower events. (It should be noted that the shower detection efficiency as calculated by

the Monte Carlo programs was very sensitive to the dynamics of the production mechanism of the gamma rays.)

4. Geometric Reconstruction of the Showers

The film was processed automatically by the SASS system,[37] which digitized the position of all sparks, fiducial lights, and data box lights for each frame, and stored the information on tape via the program FLICKERS.

The program DHARMA-HS used the FLICKERS output tape and the Master List to locate and then reconstruct the shower directions and energies in three space. The reconstruction program associated the scanning information on the Master List with the appropriate record on FLICKERS and then using the grid zone information grouped the digitized spark position into the appropriate showers. Each stereo view was treated independently, and then later combined to yield a complete description.

The conversion point of a gamma ray and hence the initial point of the shower was found by searching for dense disjoint clusters of sparks within an area defined by a square of sides approximately 1 1/2 times the size of one of the scanning grid zones. If one or more such disjoint clusters was found, the one nearest the grid zone center was taken to be the initial part of the shower, and its leading spark--the conversion point of the gamma ray.

In most cases the program was able to locate the conversion point rather readily. However, if the shower converted near the center of chamber five (as do 50% of the showers of multiplicity greater than three), the conversion point was associated with an old beam track rather than the initial point of the shower 10 to 15% of the time. In the rarer case of showers converting in the lucite between chamber edges, the program would systematically pick the point that occurred first in

the SASS scan for that region. Both of these failures contributed to the large error of ± 1 inch for the conversion point that had to be used for the subsequent kinematic fits.

The number of sparks constituting the shower was then found by forming a cone beginning at the gamma conversion point. The axis of the cone was defined by the nominal target center and the conversion point, and the area by a three degree opening angle. The area around the first spark was slightly enlarged to allow more sparks in this region to be allocated to the shower. All sparks lying within the cone were assigned to a single shower defined by the conversion point. Since the spark allocation occurred in the order in which the initial points of the showers were found, in the case of overlapping showers, the second of the two would systematically have fewer sparks assigned to it than nominally required. This depletion of sparks could have led to small biases in the shower directions, since sparks would have been preferentially dropped from certain areas of the shower development. The underestimating or overestimating of the number of sparks per shower also led to the large errors in the determination of the shower energy.

To obtain the direction of the gamma ray, a least squares fit was made to the slope and the initial point of the shower. A set of coordinates u_n and v_n, measured perpendicular and parallel to the chamber face and corrected for first order optical distortions, were obtained for each spark within a shower from FLICKERS output tape information. Then, if any point on the best straight line approximating the direction of the gamma ray was given by (u,v), the distance from a spark (u_i,v_i) to the straight line, as measured parallel to the chamber plates, was obtained to be $(v_i - v) = (v_i - v_o) - m(u_i - u_o)$, (u_o,v_o) being the conversion point. It was assumed that the best estimate for

the direction of the gamma ray was that line which minimized the parallel displacement of each of the sparks in the shower from the central value. A quadratic function of the form

$$\chi^2 = \sum_n \frac{(u_n - v)^2}{\sigma_n^2} = \sum_n \frac{\left[(u_n - v_o) - m(u - u_o)\right]^2}{\sigma_n^2}$$

was constructed and minimized with respect to v_o and m, giving the best fit to the transverse coordinate of the conversion point and the slope of the gamma ray in that view.

Defining

$$A_o = \sum_n \frac{1}{\sigma_n^2}$$

$$A_1 = \sum_n \frac{vn}{\sigma_n^2}$$

$$A_2 = \sum_n \frac{vn^2}{\sigma_n^2}$$

$$B_o = \sum_n \frac{(u_n - u_o)}{\sigma_n^2}$$

$$B_1 = \sum_n \frac{v_n(u_n - u_o)}{\sigma_n^2}$$

$$C_o = \sum_n \frac{(u_n - u_o)^2}{\sigma_n^2}$$

The minimization yielded

$$V_o = \frac{B_1 B_o - A_1 C_o}{B_o^2 - A_o C_o}$$

$$m = \frac{B_1 - B_o v_o}{C_o}$$

with the errors

$$\langle \delta v_o^2 \rangle = \sum_i \left| \frac{\partial v_o}{\partial v_i} \right|^2 \sigma_i^2 = \frac{C_o}{A_o C_o - B_o^2}$$

$$\langle \delta v_o \delta_m \rangle = \sum_i \frac{\partial v_o}{\partial v_i} \sigma_i^2 \frac{\partial m}{\partial v_i} = -\frac{B_o}{A_o C_o - B_o^2}$$

$$\langle \delta_m^2 \rangle = \sum_i \left(\frac{\partial m}{\partial v_i} \right)^2 \sigma_i^2 = \frac{A_o}{A_o C_o - B_o^2}$$

Only the transverse coordinate of the conversion point was allowed to vary in the fit, because, to first order, it was more sensitive in determining the shower direction with respect to the target than was the perpendicular coordinate. This method also had the important attribute, that it maintained the linearity of the fit.

The error for each spark was written as

$$\sigma_n^2 = \sigma_o^2 + \tan^2(\theta_o/2)/\cos^2\phi(u_i - u_o)^2$$

The first term in the sum, σ_o^2, represented a constant error per spark, while the second term diverged as the shower length increased, reflecting the spread of the sparks away from the central value. The angle ϕ measured the obliquity of the shower with respect to the perpendicular to the chamber plates, while θ_o was a measure of the opening angle of the conical spread of the shower. It was found that the best fits were obtained for $\sigma = 0.2$ and $\theta_o = 24$ deg. This large opening angle, θ_o, reflected the fact that the shower direction was most accurately obtained from the first four or five colinear sparks of the shower.

The information from the two views could easily be combined, to obtain the direction cosines

$$\alpha = \pm 1/\rho \qquad \beta = m_1/\rho \qquad \gamma = m_2/\rho$$

where

$$\rho^2 = 1 + m_1^2 + m_2^2$$

and m_1 and m_2 were the slopes of each of the projections of the shower. The errors for the direction cosines for the shower in three space could easily be calculated

$$\langle \delta\alpha^2 \rangle = \frac{1}{\rho^6} \left[m_i^2 \langle \delta m_1^2 \rangle + m_2^2 \langle \delta m_2^2 \rangle \right]$$

$$\langle \delta\beta^2 \rangle = \frac{1}{\rho^6} \left[(1 + m_2^2)^2 \langle \delta m_1^2 \rangle + m_1^2 m_2^2 \langle \delta m_2^2 \rangle \right]$$

$$\langle \delta\gamma^2 \rangle = \frac{1}{\rho^6} \left[m_1^2 m_2^2 \langle \delta m_1^2 \rangle + (1 + m_1^2) \langle \delta m_2^2 \rangle \right]$$

If the same shower was observed in two different chambers (corner shower), its direction cosines, $\underset{\sim}{\alpha}$, were found from the direction cosines $\underset{\sim}{\alpha}_1$ and $\underset{\sim}{\alpha}_2$ of the two shower segments, as determined in the two chambers independently, by standard techniques. If the error matrices for the two sets of direction cosines were E_1 and E_2, while E was the final error matrix, we could write

$$E^{-1} = E_1^{-1} + E_2^{-1}$$

$$E^{-1}\underset{\sim}{\alpha} = E_1^{-1}\underset{\sim}{\alpha}_1 + E_2^{-1}\underset{\sim}{\alpha}_2$$

Since the direction cosines were not linearly independent, the outlined method had to be applied to two of the cosines, while the third was calculated from the other two.

The production version of DHARMA-HS used to measure the data sample did not include many of the features of the fitting process as previously outlined. It did not obtain the best fit to the conversion point, but rather, in turn, set it equal to the coordinates of the first spark in the shower as located by the spark search, the coordinates of the second spark, and the average of the two. The fit was attempted for all three combinations and the slope for the combination having the minimum χ^2 was used. However, the coordinates, retained for the conversion point itself for the kinematic fits, were those of the first spark, and not of the combination that minimized χ^2. This contributed to the large error on the intersection point.

In the fit itself, the errors were set constant so that all sparks

obtained equal weights. This meant that the shower direction was determined by the preponderance of sparks in the rear of the shower, again leading to a larger error for the direction of the showers than necessary. The error itself was displayed as a constant angular error for the shower direction in three space, and was set to b/N_s, where b was a constant and N_s was the number of sparks in the shower (an average of the number of sparks found in the two stereo views). This method eliminated all information on the errors of the independent fits in the two stereo views of the shower and tended to increase the size of the errors on the direction of the showers. In the case of corner showers, since no error was obtained until after the entire shower was reconstructed in three dimensions, the direction cosines for the segments of the shower observed in the two different chambers were approximately averaged, but not combined using a method reflecting the goodness of the fit of each constituent segment. Again this tended to increase the angular error for the shower.

An experimental version of DHARMA-HS was written[45] correcting most of the discrepencies of the production version of the reconstruction program. Once the errors in the experimental version had been optimized, it was found that no severe biases existed in the production version, but that there was a tendency to lose information on the shower and hence increase the error on both the conversion point and the shower direction. These larger errors were reflected in the resolution obtained in the kinematic fits.

In the study of the reaction $\pi^- p \rightarrow \pi^o \pi^o n$ the large directional errors resulting from the reconstruction of the gamma rays affected mainly the resolution of the $(\pi^o n)$ invariant mass. The dipion invariant mass, on the other hand, was determined mainly by the direction and

timing of the detected neutron, so that the large directional errors for the gamma rays were of limited importance in the determination of the π-π scattering cross-section.

5. Kinematic Fitting

The method of least squares with constraints to obtain kinematic fits to data has been well documented.[46] The LBL Group A kinematic fitting program SIOUX[40] was used to generate a set of kinematically compatible four vectors for the reaction $\pi^- p \rightarrow \pi^o \pi^o n$ with the subsequent decay $\pi^o \rightarrow \gamma\gamma$. All the initial and final four vectors of the interaction in question were measured, so that, with the usual assumptions about Gaussian errors for the measured quantities, the subsequent kinematic fit had six constraints (a 6C fit in the jargon). It was also possible, by excluding the neutron information, to do a 3C fit to the data and compare it directly to similarly fitted neutral final state trigger data.

The method of least squares assumes Gaussian errors in the measured quantities, so that special care had to be exercised to ensure that the variable that was used in the fit had a scatter around a central (fitted) value that came closest in approximating a Gaussian distribution.

Since the SIOUX package (including the kinematic fitting program SQAW) was originally written as a bubble chamber data fitting routine, a number of variables that had Gaussian errors in measurements associated with the bubble chamber detection techniques, no longer did so in the present experiment. For instance, within the standard SIOUX program the variable $1/p_\perp$ (where $p_\perp$ is the projection of the momentum perpendicular to the magnetic field in the chamber) was considered to have Gaussian errors, whereas, in the present case, since it was the time of

flight of the neutron that was measured and the energies of the gamma rays that were estimated directly, it was the velocity of the neutron and the momenta of the photons that were considered to be Gaussianly distributed about their central (fitted) values. In all these cases SIOUX was changed accordingly, to correspond to these differences in measurement techniques.[47]

In addition, in this experiment a number of the particle directions were measured by a series of scintillation counters. The particles could have traversed along any trajectory which was compatible with all counters that were triggered by it, but certainly not along any other trajectory. This finite region of allowed trajectories with sharp boundaries, with the trajectories having a flat distribution over the allowed region, seemed at first glance to be incompatible with the use of central trajectories with Gaussian distributions as was required by SQUAW. To overcome this difficulty, all initial values of particle directions as measured by counters, were taken to be the central values compatible with the counters that had triggered. The errors were estimated to be equal to the second moments of a flat probability distribution defined by the size of the counter and zero everywhere else. Thus, for instance, in determining the path of a beam particle through a beam hodoscope element of dimension $\ell \times \ell$ inches, the beam trajectory was estimated to pass through the center of that square with an error of

$$\sigma^2 = \frac{1}{\ell} \int_{-\ell/2}^{\ell/2} x^2 dx = \frac{2}{3} \cdot \frac{1}{\ell} \left(\frac{\ell}{2}\right)^3 = \frac{\ell^2}{12}$$

in the horizontal direction, perpendicular to the beam.

The gamma ray directions and conversion points were obtained by the shower reconstruction program DHARMA-HS as outlined in Sec.II.A.4 and passed on to SIOUX, along with the data box information, on its output

tape.

The SIOUX fit was done in two parts. The shower directions and conversion points from DHARMA-HS, along with the beam trajectory, as determined from the hodoscope information, were employed to obtain the best intersection point (and hence interaction point) of the rays. New directions were then calculated for the gamma rays and the beam trajectory. The showers were constrained to pass through the intersection point and their respective conversion points, while the beam trajectory was defined by the intersection point and a pseudo-stationary point compatible with the beam hodoscope information. If the beam hodoscope information was ambiguous--not enough or too many beam hodoscope counters had triggered-- the initial beam direction was taken to be equal to the average beam direction and not used in the interaction point calculation. It was these directions for the particles, along with the additional energy information that was used in the least squares fit to obtain the particle four vectors.

To obtain the intersection point, the quantity

$$\chi^2 = \sum_s (z_i^s - \lambda^s \ell_i^s) E_{ij}^{s-1} (z_j^s - \lambda^s \ell_j^s)$$

was minimized, where we defined the variables

$z_i^s = x_i^o - x_i^s$

x_i^o = intersection point

x_i^s = conversion point or stationary point on beam trajectory

λ^s = scaling parameter for the length of the shower

χ^2 was minimized with respect to λ^s to obtain

$$\lambda^s = \frac{\ell_i {}^s E_{ij}^{s-1} z_j {}^s}{\ell_i {}^s E_{ij}^{s-1} \ell_j {}^s}$$

and with respect to x_i^o to obtain

$$x_i^o = M_{ij}^{-1} b_j$$

where

$$M_{ij} = \sum_s E_{iK}^{s-1} (\delta_{Kj} - \alpha_K {}^s \alpha_j {}^s)$$

and

$$b_i = \sum_s E_{iK}^{s-1} (\delta_{Kj} - \alpha_K {}^s \alpha_j {}^s) x_j {}^s$$

The error matrix $E_{ij}{}^s$ was obtained by considering

$$\ell_i = \ell \alpha_i$$

Differentiating $\quad \delta \ell_i = \ell \delta \alpha_i + \alpha_i \delta \ell_i$

Squaring, averaging, and assuming that $\langle \delta \ell \delta \beta_i \rangle = 0$

$$E_{ij} = \ell^2 \langle \delta \alpha_i \delta \alpha_j \rangle + \langle \delta \ell^2 \rangle \alpha_i \alpha_j$$
$$= \ell^2 A_{ij} + \Delta^2 \alpha_i \alpha_j$$

By multiplication, if necessary, it could be shown that

$$E_{ij}^{-1} = \ell^{-2} \left[(A_{ij} + \alpha_i \alpha_j)^{-1} - \alpha_i \alpha_j \right] + \Delta^{-2} \alpha_i \alpha_j$$

The error matrix for the intersection point was obtained in the usual manner.

$$E_{ij}{}^0 = \langle \delta x_i {}^0 \delta x_j {}^0 \rangle = \sum_s \frac{\partial x_i {}^o}{\partial \ell^s {}_K} E_{K\,m}{}^s \frac{\partial x^o {}_1}{\partial \ell^s {}_m}$$

In the limit when $\Delta^2 \to \infty$ the expressions simplified considerably to yield

$$X^2 = \sum_s z_i {}^s E_{ij}^{s-1} z_j {}^s$$

$$E_{ij}^{-1} = \ell^{-2} \left[(A_{ij} + \alpha_i \alpha_j)^{-1} - \alpha_i \alpha_j \right]$$

It was in this limit that the intersection point was calculated and its

error matrix obtained.

The previous method of obtaining the intersection point did not include the knowledge that for a good event, the interaction point had to be within the target. Using the usual techniques of averaging, a target averaged intersection point, x_i^a, was obtained. Setting

$$E_{ij}^{a-1} = E_{ij}^{o-1} + E_{ij}^{t-1}$$

and

$$E_{ij}^{a-1} \; x_j^a = E_{ij}^{o-1} \; x_j^o + E_{ij}^{t-1} \; x_j^t$$

where x_j^t was the target center and E_{ij}^t its error matrix. E_{ij}^t was obtained from the second moments of the spatial coordinates for a flat probability distribution over the volume of the target.

As already mentioned, the intersection point calculation required a stationary point on the beam trajectory. If the beam trajectory passed through the two points whose components perpendicular to the beam trajectory were given as (x_1, z_1) and (x_2, z_2), then any other point on the trajectory could be found. Thus by geometry (similar traingles)

$$\frac{z - z_1}{y - y_1} = \frac{z - z_2}{y - y_2}$$

and one obtained

$$z = \frac{1}{y_2 - y_1} \left[(y - y_1)z_2 - (y - y_2)z_1 \right]$$

Making the usual assumptions, and calling z_o the stationary point, while z^t the target center, one obtained

$$\langle \delta z^o \delta z^t \rangle = \frac{1}{(y_2 - y_1)^2} \left[(y_o - y_1)(y_t - y_1)\langle \delta z_1^2 \rangle \right.$$

$$\left. + (y_o - y_1)(y_t - y_2)\langle \delta z_1 \rangle^2 \right]$$

Setting

$$\langle \delta z^o \delta z^t \rangle = 0$$

and solving

$$y_o = \frac{y_1(y_t - y_1)\langle \delta z_2^2 \rangle + y_2(y_t - y_2)\langle \delta z_1^2 \rangle}{(y_t - y_1)\langle \delta z_2^2 \rangle + (y_t - y_2)\langle \delta z_1 \rangle^2}$$

Then x_o and z_o could be calculated from the known slope of the trajectory. The point (x_o, y_o, z_o) was interpreted to be that point which remained stationary while the target center was allowed to move. It was the point used in the intersection point calculation for the stationary point on the beam trajectory.

The least squares fit to the target averaged intersection point was equivalent to a 2n constraint fit, where n was the number of rays used in the fit. The intersection point fit without the target averaging was equivalent to a (2n - 3) constraint fit. Confidence levels were calculated for the fits and were found to exhibit the usual characteristics--a relatively smooth behaviour above the one percent level and a sudden rise in the number of events having a confidence level of less than 1% for the fit. In the data sample used for the analysis of the differential cross-sections, a 1% confidence level cut on the interaction point fit was imposed to obtain a cleaner sample of data.

The interaction point as well as the first spark in each shower were then used to define the gamma ray direction, while the neutron direction was determined by the interaction point and the center of the neutron counter that had fired (if more than one counter had triggered, the event was discarded). The directional errors for the showers were calculated from the errors for the interaction point (n + 2 in.) and for the first spark of each shower ($\pm$ 1 in.), while the errors for the neutron direction were those obtained from the interaction point error and the error introduced by assuming that the neutron had interacted at the center of the scintillator of the neutron detection counter (these

errors were again set equal to the second moments of a flat probability distribution over the volume of the scintillator).

Once the directions of the initial and final state particles had been established, it only remained to obtain their energies. The energy of the incident π^- was obtained from the wire-orbit information, already outlined in Sec. II.B.1. The error in the central value was taken to be equal to the momentum bite of $\Delta p/p = \pm 1.0\%$, while the central value itself was set to 10 MeV below the nominal wire orbit data to account for the energy loss because of the material in the beam, i.e., the scintillation counters, the gaseous freon of the Cerenkov counter, the liquid hydrogen of the target.

The energy of the neutron was obtained from the time of flight measurements, while the gamma ray energies were estimated from the number of sparks observed within a shower. The absolute calibration for the time of flight as well as the relationship of gamma ray energies to the number of sparks in the corresponding shower was obtained from the charge exchange data $\pi^- p \rightarrow \pi^o n$.

The time of flight measurement yielded a number in arbitrary units (ADC units on the data light array) which had to be calibrated to yield true timing information. Essentially one had to obtain two parameters, s and n_o, for each counter to yield the formula

$$t = s(n - n_o) = sn - sn_o$$

The slope, s, was a function of the electronic setup only, and was independently obtained using a light pulser and suitable delays in the cabling connecting the ADC unit to the rest of the electronics. It was found, as expected, that s was the same for all counters. The zero point, sn_o, depended on the geometry. It was found by considering the position of the prompt peak, t_i^{PPK}, for each counter, assuming it

travelled with the speed of light, and calculating the time taken for it to arrive at the neutron counter under question, from the target center. A cross-check of the formula was obtained from fits to the charge exchange data.

The two shower events were fitted using directional information only to a 2C fit for the hypotheses $\pi^- p \rightarrow \pi^o n$ and $\pi^o \rightarrow \gamma\gamma$. Since the neutron velocity for this reaction was a unique function of the laboratory angle, the position of the π^o peak for the passing events determined another point for the calibration of the timing formula. The zero point was adjusted to yield the best value for both the prompt peak and the π^o peak. The position of the calibration points for the timing formula were considered to be sufficiently well determined, that the only error considered in the time of flight measurement was that introduced by electronic jitter ($\pm$ 2/3 nsec). It should be noted that the calculated velocity of the neutron from the timing formula took into account the variation in the position of the interaction point as well as the neutron scattering point in the scintillator of the neutron counter. It even considered the velocity of the light signal in the scintillator that triggered the phototube.

The raw time of flight spectrum of the π^o for charge exchange was displayed in Fig. 15b. This time of flight spectrum was obtained from a previous experiment[32] using the same equipment as the present one, in which all the neutron counters were set at the same neutron production angle.

The charge exchange reaction was also used to obtain a calibration of the gamma ray energies as a function of the number of sparks deposited in the spark chambers by the showers. The spark chamber system was divided into four regions. In the last of these regions,

corresponding to backward going gammas, no spark-energy calibration could be made, since most of these photons deposited their energy in the gamma counters and not within the active part of the chambers. In all other sections a successful fit was made to the empirical two parameter formula

$$E/\cos\theta = (E/\cos\theta)_o \sinh(n/n_o)$$

where E was the energy of the gamma ray as obtained from the charge exchange fit, θ was the obliquity of the gamma ray to the chamber face, and n was the number of sparks in the shower as obtained by DHARMA-HS. The factor of $1/\cos\theta$ appeared in the expression because the gamma rays travelling obliquely to the chamber faces traversed more radiation lengths of lead than those normally incident.

The errors, $\Delta E/E$, obtained for this energy calibration ranged from 40 to 100%, being the largest for the very energetic showers which had a tendency to leave the chambers through the back face.

The resolution of the kinematic fitting was best illustrated by the invariant mass distribution of the $(\gamma\gamma)$ system in the fit to the hypothesis $\pi^- p \rightarrow n\gamma\gamma$ for the two shower events. The $(\gamma\gamma)$ mass spectrum displayed a π^o peak of half width of 20 MeV centered around 135 MeV (see Fig. 15c).

It should be noted that all errors used in the fits, that were not set by the geometry, were optimized using the method of pull quantities[46] so that they represented a consistent set of Gaussian errors.

6. Geometric Acceptance and Kinematic Cuts

The neutron counter geometry distorted the phase space of the final states of the reactions studied. This occurred because each counter subtended a small fraction of the 2π radian interval in azimuth and this fraction varied from counter to counter. Other factors which contri-

buted slightly to the phase space distortion were the variation of the neutron counter detection efficiency with neutron energy, and the neutron timing acceptance gate. In particular

$$\frac{(\text{neutron flux detected by a counter at an angle } \Theta)}{(\text{area of counter}) \cdot (\text{detection efficiency})}$$

$$= \frac{(\text{total neutron flux at an angle } \Theta)}{(\text{area of annular ring intersecting neutron counter})}$$

Defining the symbols (see Fig. 16a)

$F_n(\Theta)$ = neutron flux detected by a counter at an angle

$F_t(\Theta)$ = total neutron flux at an angle

r = distance of counter from the interaction point

D = diameter of the face of the counter

η = neutron counter efficiency

we could rewrite the previous expression as

$$\frac{F_n(\Theta)}{\frac{\pi D^2}{4}\,\eta} = \frac{F_t(\Theta)}{2\pi r \sin\Theta \;\; r\Delta\Theta} \approx \frac{F_t(\Theta)}{2\pi r \sin\Theta \; D}$$

where

$$r\Delta\Theta \approx D$$

Then

$$\frac{8r}{D} \cdot \frac{1}{\eta} \sin\Theta \, F_n(\Theta) = F_t(\Theta)$$

Setting the distance r to 15 ft. and D to 8 in. yielded

$$\frac{180}{\eta} \cdot \sin\Theta \, F_n(\Theta) = F_t(\Theta)$$

The calculation previously outlined, did not account for the fact that the neutron counters were not exactly touching one another and therefore some of the neutrons could be lost in the small spaces between the counters. Another effect not included, which was also small, was the variation of the ratio of the neutron counter area to that of the annular ring over the face of the counter. A complete Monte Carlo integration for the neutron counter geometry yielded

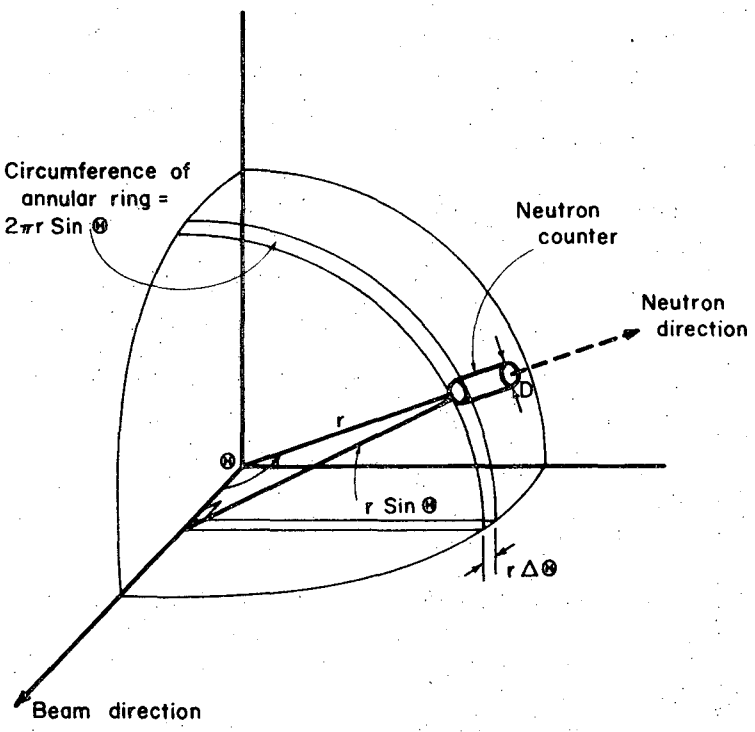

Fig. 16a. The neutron counter geometry i the laboratory.

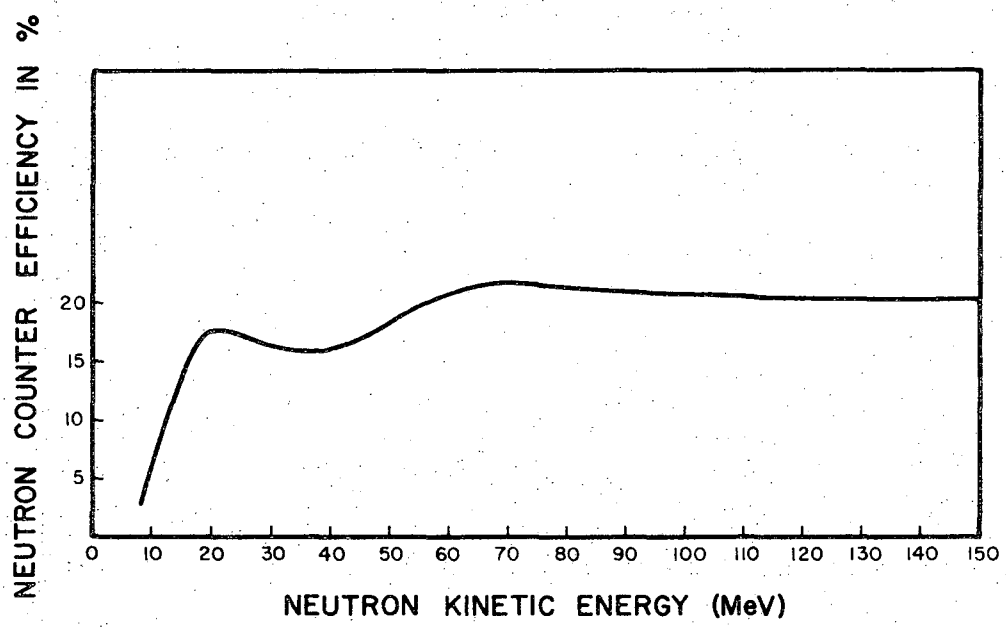

XBL 722-135

Fig. 16b. The neutron counter detection efficiency as a function of the neutron kinetic energy.

$$\frac{212}{\eta} \sin\Theta \, F_n(\Theta) = F_t(\Theta)$$

Thus $(\frac{212}{\eta}) \sin\Theta$ was the geometric acceptance correction factor expressed as a function of the neutron production angle in the laboratory frame.

In addition to the distortions introduced by the geometric acceptance, events with both small and very large neutron kinetic energies were lost.

The neutron counters had an efficiency, η, of 20% for the detection of neutrons of kinetic energies above 20 MeV (see Fig. 16b). However, below this energy cutoff, the efficiencies dropped rapidly so that very few neutrons could be observed of small kinetic energies. To prevent uncertainties in the data that could be introduced by the uncertainty in the rapid variation in detection efficiency, a cutoff in the timing gate was set so that no neutrons of $\beta < 0.17$ could be observed. For the interaction under study, $\pi^- p \rightarrow \pi^o \pi^o n$, the momentum transfer to the nucleon was directly related to the neutron kinetic energy in the laboratory, so that a cutoff in the neutron kinetic energy would also yield a cutoff in the momentum transfer. The cutoff would also distort the dipion mass spectrum accepted by the system. The β cutoff did not affect the fits to the theoretical distributions, since it could be taken into account in the fitting process. It did, however, have a small affect on the calculation of the $\pi^-\pi$ scattering cross-section.

The Prompt Peak Killer (PPK) timing cut to eliminate $\beta = 1$ particles, also eliminated a number of fast neutrons associated with the interaction $\pi^- p \rightarrow \pi^o \pi^o n$. This timing cut did not affect the dipion mass spectrum of interest, since only peripheral events (corresponding to slow neutrons) were under study. However, it did have an affect on the total number of detected events and hence on the absolute normalization

of the π-π scattering cross-sections.

Fig. 17a displays the neutron kinematics in the c.m. and lab frames as a function of the dipion mass for a π^- momentum of 2.4 GeV/c. In the figure the neutron c.m. angle was measured with respect to the proton direction. In particular, it could be seen that the timing cut restricting the neutron velocities to $\beta > 0.17$ distorted the low end of the dipion mass spectrum, whereas the PPK cut did not appear to have much of an affect. In addition the polar angular region subtending 12 to 72 in the laboratory restricted the observation of the high end of the mass spectrum. Since phase space for the reaction, even at 2.4 GeV/c, was rapidly falling in this region, the cut did not cause much distortion in the shape of the spectrum.

7. Neutron Scattering Corrections

The neutron produced in the hydrogen target by a π^- interaction, at a laboratory angle of Θ, had to traverse the lead and aluminum plates of the spark chambers before they could be detected by the neutron detection counters. This meant that part of the neutron flux seen by the counters was scattered because of neutron-Pb and neutron-Al interactions. The ratio of unscattered neutrons, N, detected at an angle Θ, to the total number of neutrons produced at that angle, and for a neutron kinetic energy E, was then

$$\frac{N(\Theta,E)}{N_o(\Theta,E)} = e^{-a_{Pb}x_{Pb}(\Theta)\sigma_{Pb}(E)} \; e^{-a_{Al}x_{Al}(\Theta)\sigma_{Al}(E)}$$

where $x_{Pb}(\Theta)$ and $x_{Al}(\Theta)$ were the amounts of lead and aluminum, respectively, at an angle Θ between the interaction point and the neutron detection counter; while $\sigma_{Pb}(E)$ and $\sigma_{Al}(e)$ were the neutron scattering cross-sections as a function of the incident neutron kinetic energy. Since $\sigma_{Pb}(E)$ and $\sigma_{Al}(E)$ both increase by approximately a factor of two

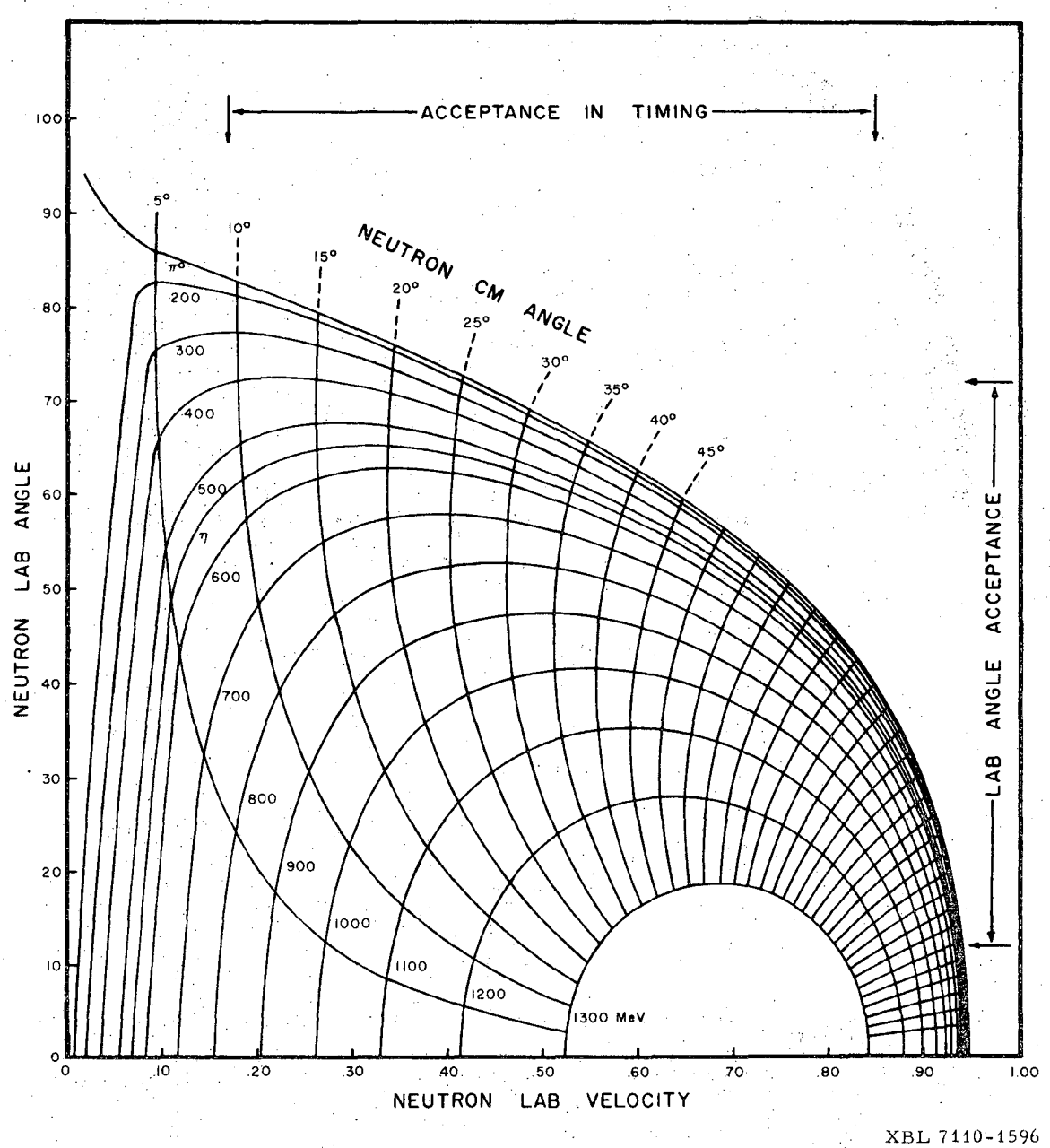

XBL 7110-1596

Fig. 17a. Kinematics for the reaction $\pi^- p \rightarrow nX$ at an incident π^- momentum of 2.4 GeV/c.

as E decreases from 100 MeV to 20 MeV, the scattering corrections were highly energy dependent below 100 MeV. On the other hand, above 100 MeV of neutron kinetic energy, the cross-sections remain relatively flat, and the corrections depended only on the neutron laboratory production angle.[47] (See Fig. 17b.) We could write

$$\frac{N}{N_o} = e^{-a_{Pb}x_{Pb}(\Theta)\sigma_{Pb}(E_o)}\left[\frac{\sigma_{Pb}(E)}{\sigma_{Pb}(E_o)}\right] e^{-a_{Al}x_{Al}(\Theta)\sigma_{Al}(E_o)}\left[\frac{\sigma_{Al}(E)}{\sigma_{Al}(E_o)}\right]$$

$$= e^{-\ell_{Pb}(\Theta)\, s_{Pb}(E)}\, e^{-\ell_{Al}(\Theta)\, s_{Al}(e)}, \qquad E_o = 100 \text{ MeV}$$

where

$$\ell(\Theta) = ax(\Theta)\sigma(E_o)$$

and

$$s(E) = \sigma(E)/\sigma(E_o)$$

Hence

$$N_o = Ne^{\ell_{Pb}(\Theta)s_{Pb}(E)}\, e^{\ell_{Al}(\Theta)s_{Al}(E)}$$

where $s_{Al}(E) = 1$ for E greater than 100 MeV.

Figure 17c displays the ratio N_o/N as a function of the neutron production angle, Θ, for both 100 MeV and 30 MeV neutron kinetic energies.

The number of neutrons detected, however, increased, rather than decreased because of the neutron scatters in the spark chambers. A neutron inelastically scattered by a heavy nucleus, would often have a number of relatively energetic neutrons and protons in the final state. In fact the number of neutrons produced of similar kinetic energies in n-Pb and n-Al interactions ranged from one to three as the incident neutron kinetic energies ranged from 20 MeV to 700 MeV.[48] Any one of these neutrons could trigger the neutron counters, so that the number of triggers was larger than it would have been if no neutron inelastic scattering had occurred.

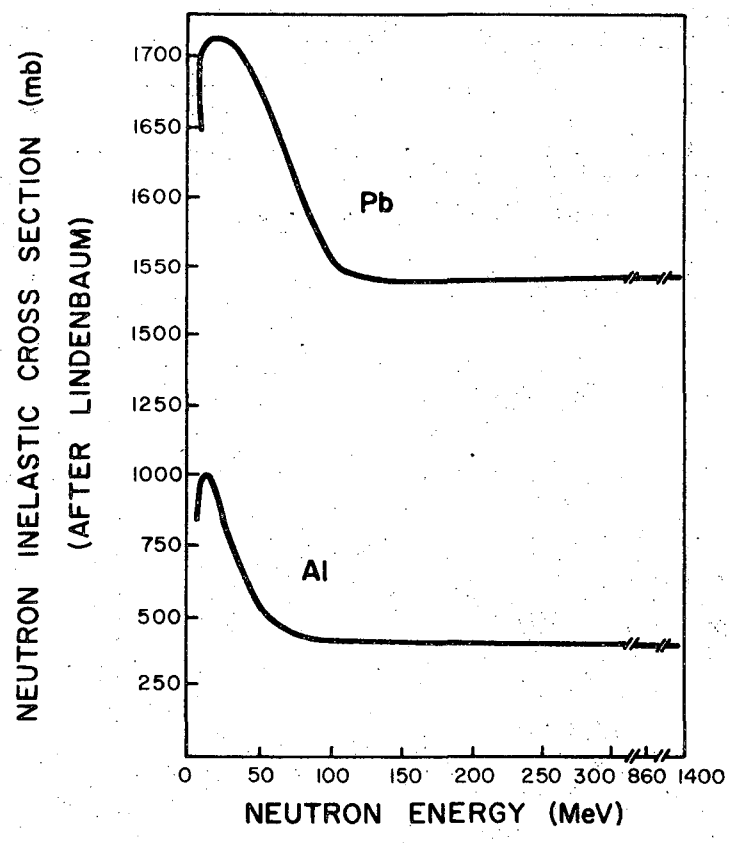

(b)

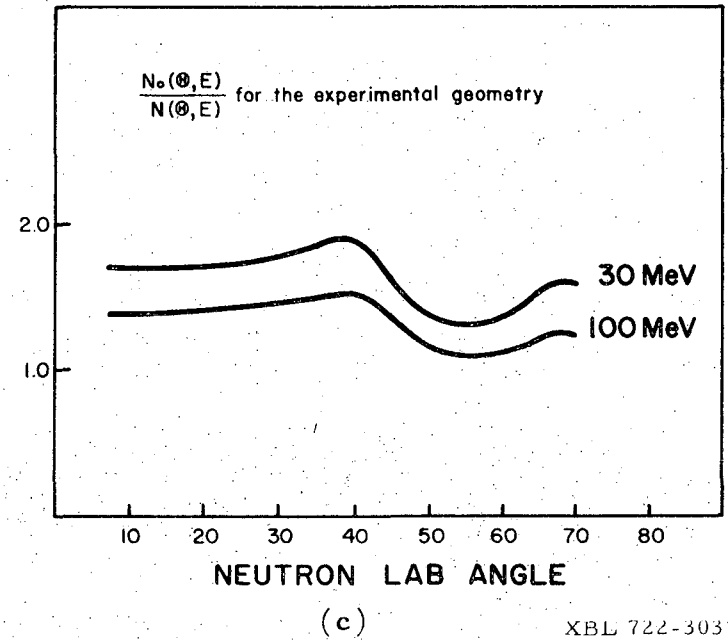

(c)

XBL 722-303

Fig. 17. (b) Neutron inelastic cross-sections.
(c) The ratio of neutrons produced at an angle Θ and an energy E to the number not scattered for the same Θ and E.

The predicted amount of neutron scattering in the chambers was consistent with the observed data. For the incident π^- momentum of 1040 MeV, the two shower events fit to the hypothesis $\pi^- p = n\pi^o$, were compared for both triggering modes (normal and without the neutron coincidence in the final trigger) as a function of the laboratory angle Θ for the first 10 neutron counters. Once the normal trigger mode data had been corrected for the geometric acceptance and neutron counter efficiency, and the data without the neutron coincidence in the trigger had been subjected to the timing cuts of the normal date, the two sample of events, normalized to the same number of incident beam particles, agreed within 5% in predicting the neutron scattering correction. This confirmed the expectation that the neutron scatters were reasonably well understood.

IV. TOTAL CROSS SECTIONS

The data for which there was no neutron coincidence in the trigger were used to calculate the total neutron cross-sections and also the partial cross-sections for $\pi^- p \rightarrow n + \gamma$'s. The four gamma production cross-section was then taken to be that of $\pi^- p \rightarrow n\pi^o\pi^o$, since this was the only neutral final state that could be produced as a neutron and four gamma rays. (Recent measurements of the decay mode $\eta \rightarrow \pi^o\gamma\gamma$ had shown that it was consistent with zero.[32])

The data without the neutron coincidence in the trigger were used to determine the cross-sections since they did not have the drawback of the geometric and kinematic cuts that were imposed on the normal trigger data. Furthermore every final state was of interest and the cross-sections could be obtained by counting events of a particular gamma ray multiplicity and applying known corrections to it. These corrections could be easily summarized:

a. Not all the gamma events resulted from the interaction of the beam with the liquid hydrogen. Some number of the beam particles interacted with the target casing. This number was measured by taking data with the target empty for a certain number of incident beam particles at each momentum, and normalizing it to the number of incident beam particles of the target full data.

b. The number of observed m-gamma events, $m_{m\gamma}$, had to be corrected for scanning efficiency and gamma detection efficiency.

c. The neutral final state requirement in the trigger vetoed some legitimate events because some of the particles associated with the primary reaction $\pi^- p \rightarrow$ (neutrals) occasionally underwent an additional scatter with charged particles in the target or target casing. These scattered charged particles would then cause the event to be vetoed.

The corrections in this case were small and well understood.

In Secs. III.A.2 and III.A.3 we obtained the scanning efficiency matrix, E; the probability matrix, U, of observing one or two additional showers per event because of the long active time of the spark chambers; and the probability matrix, D, of a single gamma not converting or being lost upstream. (The probability of observing a single gamma ray as two gammas was set to zero, since no concrete evidence could be found in the data of this form of feedup.) If $m_{m\gamma}$ was the number of m-gamma events after the target empty subtraction, we had

$$\underset{\sim}{m\gamma}' = D^{-1}U^{-1}E^{-1}\ \underset{\sim}{m\gamma}$$

Since the correction matrices did not commute, the order of applying the correction matrices had to be considered. The matrices D^{-1} and U^{-1} corrected for either losing or gaining gamma rays because of the physical characteristics of the spark chambers, so that (UDm') was the number of gamma rays that should have been observed in the spark chambers. On the other hand the matrix E^{-1} corrected the number that was observed to the number that should have been observed. Thus the order as indicated above was correct. The number of gamma events that were not vetoed by the neutral final state trigger was then $\underset{\sim}{m}_{\gamma}'$. However, a number of legitimate events were lost because of the anticounters surrounding the target.

a. The gamma rays of the neutral final state converted in the target, the target casing, or the anti-counters, vetoing the event. This correction is of the order of 0.9% per gamma ray in the final state.

b. The incident π^- which interacted to produce a neutral final state also produced at least one delta ray energetic enough not to be stopped within the hydrogen target and was instrumental in the vetoing of the event. A Monte Carlo study of this possibility yielded a

correction of 1.5% for the hydrogen target geometry of this experiment.

c. The final state neutron elastically scattered with another proton within the target, which then escaped and vetoed the event. This problem was also resolved using a Monte Carlo method, and was found to yield a correction of 1%.

d. Each π^o produced in the final state decayed by the mode $\pi^o \rightarrow e^+e^-\gamma$ 1.16% of the time, so that the observed cross-section had to be corrected by 0.0116 for each π^o in the final state.

Tables IVa through IVe showed the number of scanned events and the corrections as they were applied to the data. The gamma multiplicities were obtained from four rolls of film for each momentum. They were then corrected for non-hydrogen associated events by normalizing the target empty data to correspond to the same number of incident beam particles as the target full data, and subtracting the extraneous events.

The uncertainties in the number of events for each gamma multiplicity as presented in Tables IVa through IVe were purely statistical resulting from the statistical fluctuation in the number of observed events as well as those in the sample being used in the scanning efficiency correction matrix. If the conversion efficiency was misestimated by 1%, an error 1 1/2 times as large as the one presented in the tables was introduced. However, even a large error in the feedup estimation (~ 50%) did not change the errors as presented in the tables significantly. Thus the error in the number of events in each gamma multiplicity category was due to the statistical fluctuation of the observed events as well as the error in the estimation of the conversion efficiency. The error used in the cross-section calculations was 1 1/2 times the statistical error presented in the tables.

The cross-sections for $\pi^- p \rightarrow n + m\gamma$'s could be easily calculated,

by setting

$$\sigma_{m\gamma} = \frac{n_{m\gamma}}{n_o} \frac{1}{\ell \rho N} \cdot \frac{1}{\kappa}$$

where n_o = total number of incident π^-s = $(1 - q_1)n_b$

q_o = the fraction of μ^- and e^- contamination in the beam

n_b = the number of incident beam particles

ℓ = the effective length of the hydrogen target (19.75 cm)

ρ = density of liquid hydrogen at boiling (0.0708 g cm^{-3})

N = number of particles per mole (6.02×10^{23})

κ = factor to correct for events lost due to the anticounters

The number n_m was just the number of m-gamma events obtained from the number scanned after the target empty subtraction, and the scanning efficiency and gamma detection efficiency corrections. In addition

$$\kappa = (1 - q_3)(1 - q_3)(1 - mq_4)$$

where

q_2 = fraction of events vetoed due to energetic delta ray production (0.015)

q_3 = fraction of events vetoed due to the scattering of the final state neutron in the liquid hydrogen (0.01)

q_4 = conversion probability for a single gamma ray in the target, target casing, and anticounter scintillator (0.009)

Hence for the four shower events the cross-sections were given by

$$\sigma_{4\gamma} = \frac{n_{4\gamma}}{n_B(1 - q_1)} \frac{1}{(1975)(0.0708)(6.02 \times 10^{23})} \cdot \frac{1}{0.985} \cdot \frac{1}{0.99} \cdot \frac{1}{0.964}$$

The scanning and gamma detection efficiency corrections were applied next. The scanning efficiency matrix, as displayed in Sec. was inverted and applied to the gamma multiplicity vector. No feedup correction on a shower by shower basis was applied since no clearcut evidence existed to substantiate its use. A non-event associated

feedup of a 4% probability for an additional gamma, and a 1% probability for an addition two gammas was used. This reflected the ratio that was obtained by experimental means and incorporated a magnitude that had been found reasonable in a previous calibration of the detection efficiency.[32] The probability for a gamma ray converting in the chambers was then taken to be 89% per gamma ray. This was the best value consistent for all momenta and also agreed closely with a previous calibration of the chambers for lower energy gammas that obtained 87%.[32] It was found by Monte Carlo studies, and also optimization of the gamma multiplicites of the data that a larger conversion probability of 94% had to be taken for the two shower events because of the very specialized topology of the two body kinematics producing them. Both these numbers were incorporated in the detection efficiency corrections.

Table V shows the cross-sections for $\pi^- p \rightarrow n + m\gamma$'s as well as the beam contamination at each momentum. There was a 10% error in the beam contamination measurements.) For $\sigma_{9\gamma}$ the correction for gamma conversion in the target and the surrounding anticounters was taken to be that for nine gamma rays in the final state.

To obtain the total neutrals cross-sections the cross-sections obtained above had to be corrected for the probability of Dalitz pair production from the decay in the final state. In all cases, except for the case of the two gamma events, it was assumed that the number of π's in the final state was equal to the maximum number compatible with the gamma multiplicity, i.e., even number of gammas were assumed to have $m/2\pi^o$'s in the final state; while the small odd number of gammas, $(m - 1)/2\pi^o$'s in the final state. The two shower events were produced both from π^o decay and η decay, where the mode $\eta \rightarrow e^+e^-\gamma$ was negligible. Since about 75% of the two shower events were π^o's the correction to

Table IVa. Gamma multiplicites at 1590 MeV/c.

No. of incident beam particles for target full = 3.4×10^6

No. of incident beam particles for target empty = 0.464×10^6

# of gammas	# of events target full	# of events target empty	Hydrogen associated events	# of events after scanning efficiency corrections	# of events after feed-up corrections	# of events after feed-down corrections
0	190	12	102	62±15	65±17	50±17
1	815	27	617	528±41	553±43	-86±52
2	5262	67	4771	4803±82	5032±87	5356±114
3	1696	33	1454	1401±63	1257±68	524±121
4	2123	33	1881	1901±59	1895±63	2789±145
5	681	13	585	554-54	490±58	-25±165
6	668	12	580	706±50	703±53	1389±187
7	151	3	129	117±43	88±47	-13±166
8	97	1	89	124±29	119±31	181±117
9	37	0	37	48±16	42±17	121±48

Table IVb. Gamma multiplicities at 1790 MeV/c.

No. of incident beam particles for target full = 3.8×10^6

No. of incident beam particles for target empty = 0.504×10^6

# of gammas	# of events target full	# of events target empty	Hydrogen associated events	# of events after scanning efficiency corrections	# of events after feed-up corrections	# of events after feed-down corrections
0	164	15	50	13±12	14±13	2±13
1	640	20	489	412±35	433±37	-84±44
2	4571	80	3967	3901±76	4088±80	4145±107
3	1997	29	1778	1771±69	1687±74	904±134
4	2577	35	2313	2310±68	2317±72	3140±168
5	841	8	780	832±64	761±69	675±187
6	689	14	583	618±52	594±56	934±211
7	208	0	208	250±53	230±58	165±211
8	119	0	119	179±37	170±40	375±145
9	36	1	28	30±17	21±18	59±52

Table IVc. Gamma multiplicities at 1990 MeV/c.

No. of incident beam particles for target full = 4.08×10^6

No. of incident beam particles for target empty = 0.596×10^6

# of gammas	# of events target full	# of events target empty	Hydrogen associated events	# of events after scanning efficiency corrections	# of events after feed-up corrections	# of events after feed-down corrections
0	148	13	59	23±12	24±13	12±13
1	530	10	461	394±33	413±35	-47±42
2	4064	69	3592	3502±72	3669±76	3719±103
3	2015	33	1789	1747±70	1680±75	583±140
4	2946	37	2692	2720±74	2754±79	3884±185
5	966	13	877	898±70	811±79	407±209
6	803	10	734	860±60	842±64	1503±227
7	230	7	182	194±53	160±58	161±203
8	135	4	107	136±34	127±37	134±139
9	75	3	54	74±20	67±21	191±59

Table IVd. Gamma multiplicites at 2190 MeV/c.

No. of incident beam particles for target full = 5.0×10^6

No. of incident beam particles for target empty = 0.661×10^6

# of gammas	# of events target full	# of events target empty	Hydrogen associated events	# of events after scanning efficiency corrections	# of events after feed-up corrections	# of events after feed-down corrections
0	153	11	69	36±12	38±13	33±13
1	446	12	355	275±30	289±31	-159±38
2	3937	59	3490	3372±71	3537±76	3562±104
3	2234	34	1976	1900±75	1848±80	409±154
4	3609	41	3298	3337±84	3398±90	4762±214
5	1244	19	1100	1129±83	1026±90	560±251
6	1044	15	930	1052±72	1029±77	1865±288
7	344	8	283	277±71	237±76	55±294
8	239	2	223	302±55	294±59	349±231
9	113	0	113	155±34	141±35	402±101

Table IVe. Gamma multiplicities for 2390 MeV/c.

No. of incident beam particles for target full = 5.2×10^6

No. of incident beam particles for target empty = 0.737×10^6

# of gammas	# of events target full	# of events target empty	Hydrogen associated events	# of events after scanning efficiency corrections	# of events after feed-up corrections	# of events after feed-down corrections
0	175	2	160	134±16	141±17	134±17
1	477	20	335	274±27	282±30	-74±35
2	3278	59	2861	2723±65	2853±68	2797±95
3	2059	31	1840	1790±71	1761±76	461±145
4	3275	37	3013	3053±79	3110±84	4409±201
5	1164	24	994	995±78	898±85	417±238
6	948	8	891	1003±69	985±74	1680±278
7	331	7	281	308±69	273±75	210±278
8	230	6	187	252±50	241±53	316±204
9	102	2	87	117±29	105±30	299±85

compensate for the production of Dalitz pairs was taken to be $1.0/[0.75 \times (1 - 0.0116)]$ for these events. The total neutrals cross-sections were presented in Table VI.

The total neutrals cross-sections could be obtained by summing all the events after the target empty subtraction, regardless of which shower multiplicity category they belong to. Also, all corrections except for gamma conversion in the target and Dalitz pair production could be made without knowing the gamma multiplicities. Thus the error in the total neutrals cross-section arose only from the statistics of the whole sample and not from the errors introduced by scanning efficiency corrections and gamma detection efficiency corrections, except for the error introduced by the final correction depending on the shower multiplicity.

Table VII displays the total neutrals cross-section without and with the corrections depending on the shower multiplicites.

The errors for the total cross-sections corrected for gamma ray conversion in the target area and Dalitz pair production were then obtained by writing

$$\sigma = \frac{1}{n_o \rho \ell N(1 - q_2)(1 - q_3)} \sum_m \frac{n_{m\gamma}}{(1 - m\ 0.009)(1 - \frac{m}{2}\ 0.0116)}$$

$$\sigma \approx \frac{1}{n_o \rho \ell N(1 - q_2)(1 - q_3)} \sum_m \frac{n_{m\gamma}}{(1 - m\ 0.0198)}$$

$$\approx \frac{1}{n_o \rho \ell N(1 - q_1)(1 - q_3)} \sum_m {}_{m\gamma}(1 + m\ 0.0148)$$

$$= \sigma_o + \frac{(0.0148)}{n_o \rho \ell N(1 - q_1)(1 - q_2)} \sum_m m n_{m\gamma}$$

Then

$$\delta\sigma^2 = \delta\sigma_o^2 + \frac{(0.0148)^2}{[n_o \rho \ell N(1 - q_1)(1 - q_2)]^2} \sum_{k\ell} k < \delta n_{k\gamma} \delta n_{\ell\gamma} > \ell$$

Table V. Cross-sections for $\pi^- p \rightarrow n + m\gamma$'s in mb.

Beam momentum	1590 MeV/c	1790 MeV/c	1990 MeV/c	2190 MeV/c	2390 MeV/c
Beam contamination	.111	.076	.066	.038	.028
No. of gammas					
0	0.020±.010	0.001±.006	0.004±.006	0.009±.005	0.032±.006
1	-0.035±.031	-0.029±.023	0.015±.020	-0.040±.014	-0.018±.012
2	2.158±.069	1.438±.056	0.189±.049	0.902±.039	0.674±.034
3	0.211±.073	0.314±.069	0.186±.067	0.103±.059	0.111±.052
4	1.124±.088	1.089±.088	1.241±.089	1.206±.081	1.062±.072
5	-0.010±.099	0.234±.097	0.130±.100	0.142±.095	0.100±.086
6	0.543±.113	0.324±.109	0.480±.109	0.472±.109	0.403±.101
7	-0.005±.101	0.057±.110	0.052±.097	0.014±.112	0.051±.100
8	0.073±.071	0.130±.075	0.093±.067	0.088±.088	0.076±.074
≥ 9	0.049±.029	0.020±.027	0.061±.028	0.102±.038	0.072±.030

Table VI. The partial cross-sections for $\pi^- p \rightarrow$ (neutrals) in mb.

Beam momentum	1590 MeV/c	1790 MeV/c	1990 MeV/c	2190 MeV/c	2790 MeV/c
No. of gamma rays in corresponding m-gamma final state					
0	0.020±.010	0.007±.006	0.003±.006	0.008±.005	0.032±.006
1	-0.036±.032	-0.030±.023	-0.015±.023	-0.041±.014	-0.018±.013
2	2.244±.717	1.495±.058	1.236±.051	0.938±.041	0.701±.036
3	0.224±.077	0.331±.074	0.198±.071	0.110±.062	0.118±.056
4	1.204±.094	1.168±.093	1.330±.099	1.292±.087	1.139±.078
5	-0.011±.109	0.256±.106	0.142±.110	0.155±.104	0.110±.094
6	0.601±.125	0.358±.121	0.531±.120	0.522±.121	0.448±.111
7	-0.006±.114	0.064±.123	0.058±.110	0.016±.126	0.057±.113
8	0.083±.081	0.148±.085	0.049±.076	0.101±.100	0.087±.084
≥ 9	0.057±.034	0.023±.031	0.071±.033	0.119±.045	0.084±.037

Table VII. Total cross sections $\pi^- p \rightarrow$ (neutrals) in mb.

Beam Momentum	1590 MeV/c	1790 MeV/c	1990 MeV/c	2190 MeV/c	2390 MeV/c
Total cross-sections with out corrections depending on γ multiplicities	4.13±.096	3.56±0.076	3.45±0.072	2.99±0.060	2.56±0.051
Total cross-sections incorporating all corrections	4.38±0.103	3.82±0.082	3.60±0.076	3.22±0.066	2.76±0.056

A comparison of the data on the total cross-sections for this experiment and other experiments has been presented in Fig. 18. It could be seen that within errors the results of the present experiment agree with a number of previous ones. The data of Carroll et al.[49], Crouch et al.[50] Bizard et al.[51] and Feldman et al.[52] have been presented. Since a number of the points had to be obtained from graphical presentations in published works they may not be as accurate as could be desired.

It should be noted that the total cross-sections of Feldman et al. have the strange particle production cross-sections subtracted from the data. The main modes of strange particle production are $\pi^- p \rightarrow \Lambda K^o$ and $\pi^- p \rightarrow \Sigma^o K^o$. The cross-sections for $\pi^- p \rightarrow \Lambda K^o$ range from 200 μb to 175 μb in the energy region of the experiment, while those for $\pi^- p \rightarrow \Sigma^o K^o$ range from 175 μb to 110 μb in this same energy range.[53] The subsequent neutral decays of the produced strange particles that could contribute to the trigger are only ~ 30% of the final state, so that ~ 3 to 4% of the data taken in the present experiment was of strange particle production. In addition none of the decays of the strange particles could contribute to the cross-section of events produced as four gammas in the final state, so that the corrected four shower cross-section is also the cross section for the reaction $\pi^- p \rightarrow n\pi^o\pi^o$.

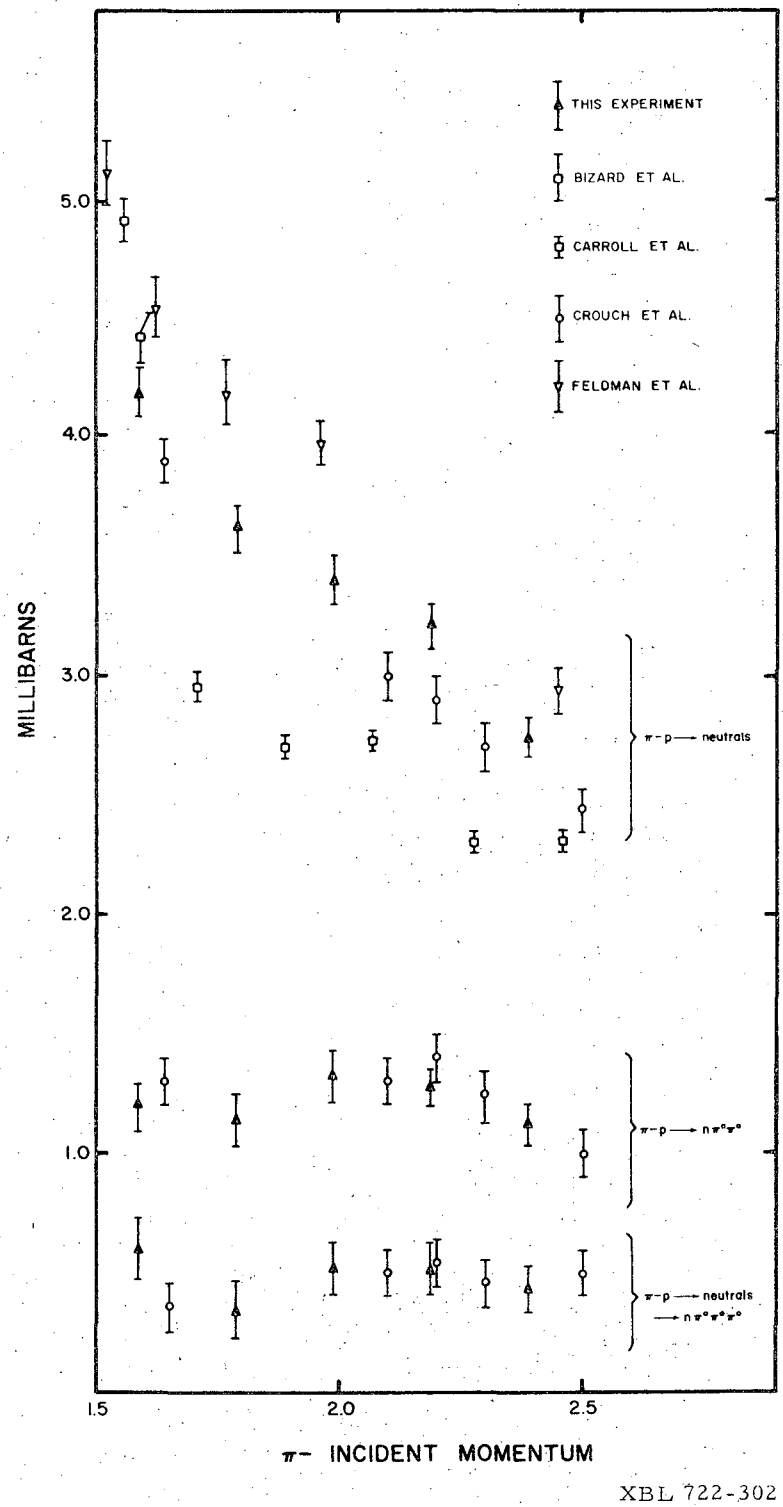

Fig. 18. Total cross-sections.

V. PROPERTIES OF THE $\pi^o\pi^o n$ FINAL STATE

The gamma events for the data with the neutron counter coincidence in the spark chamber trigger were fit to the hypothesis $\pi^- p \rightarrow \pi^o\pi^o n$ (a 6c fit). (A sample of the data without the neutron coincidence in the trigger was fit to the same hypothesis as a check on the normal trigger data. The resolution for this sample was worse than for the normal trigger data so that most of the analysis was done on the data taken with the normal trigger.) A 1% confidence level cut was made on the intersection point fit, as well as the overall kinematic fit. For the kinematic fit, the confidence level distribution was flat above the 5% point, had a gentle slope between the 5% and 1% level and then had the usual large increase in events below the 1% confidence level point. The data were examined both with the 5% confidence level cut and the 1% confidence level cut, without any significant differences being found in the resulting description of the $\pi^o\pi^o n$ final state. Thus to increase the statistics the 1% confidence level cut was chosen, although in the region of 1 to 5% there was a slight deviation from the desired flat distribution.

Examination of the $\pi^o\pi^o n$ final state distributions revealed that the dipion was produced peripherally and that a considerable enhancement existed in the $(n\text{-}\pi^o)$ mass spectrum in the $\Delta(1238)$ region. Thus to isolate the π-π interaction a peripheral cut was made so that the cosine of the dipion production angle in the c.m. was greater than 0.8, and a cut was also made on the $(n - \pi^o)$ invariant mass in the region 1100 to 1300 MeV to eliminate the $\Delta(1238)$ contribution to the final state. To isolate the $I = 0$, $J = 0$ π-π interaction, the dipion mass was restricted to invariant $(\pi\text{-}\pi)$ masses below 1 GeV, since a strong d-wave contribution to the data was observed in the region above dipion masses of

1 GeV.

Table VIII displays the number of events remaining of the data sample as a function of the various cuts. Each column of the table includes all of the previous cuts, in addition to the one specified. It should be noted that the events are not normalized to the same number of incident beam particles.

The table indicates that 25% of the passing events failed the intersection point cut, indicating that the directions of the gamma rays and the beam particles were not well determined. The large number of failures in this category were mainly due to the reconstruction program DHARMA-HS. Another 25% of the passing events failed the confidence level cut for the kinematic fit itself.

To understand the 75% failure rate of the four shower events an attempt was made to enumerate the possible types of failures and compare them to the number of passing events. The total number of events was constrained to total 36,000.

Passing events	~ 11,000
DHARMA-HS failures (10% of passing events)	~ 1,000
SIOUX failures (5% of passing events)	~ 500
Neutron scattering (50% of passing events)	~ 5,500
Mis-scanning (15% of all events)	~ 5,500
Gamma detection inefficiency (10% of all events)	~ 3,500
Bad neutron tracks (5% of all events)	~ 1,500
Non-hydrogen associated events (10% of all events)	~ 3,500
Randoms (10% of all data	~ 3,500
Others	~ 500

The neutron scattering estimate was based on 25% of the total passing

Table VIII. Four shower data fit information.

Nominal momentum	Total number of 4 gamma events	Passing events for fit to the hypothesis $\pi^- p \rightarrow \pi^o \pi^o n$				
		Total	Interaction point cut	Confidence level cut	Peripheral cut	$\Delta(1238)$ invariant-mass cut
1.6	4812	1614	1293	893	220	64
1.8	5641	1184	882	552	183	85
2.0	7029	2325	1642	1086	419	186
2.2	8320	2481	1751	1152	485	219
2.4	10459	3056	2099	1334	521	244
	36261	10720	7667	5017	1828	798

rate multiplied by an estimated average multiplicity of neutrons in the final state of two. The bad neutron tracks consisted of double neutron counter triggers which were mainly attributed to soft gammas. The randoms were estimated from the pre-prompt peak timing data and again were attributed to a room background of neutrons.

1. The Data.

If the study of the production experiment $\pi^- p \rightarrow \pi^o \pi^o n$ were to yield any information on the π-π charge exchange scattering parameters, it should have certain general features consistent with some modified form of the one-pion exchange model. This implied that the dipion should be peripherally produced or that most of the observed events were observed at small momentum transfer values. Secondly, if one were particularly interested in s-wave effects in the interaction, then, in the dipion rest frame, the π-π angular distributions should be consistent with isotropy. Additional care should also be taken to ensure that otherpossible effects in the final state did not dominate and obscure the $\pi\pi$ interaction. Thus various n-π enhancements and resonances had to be isolated and their effects minimized. In particular the effect of the $\Delta(1238)$ had to be understood.

The momentum transfer distribution $\left[t = (p_n - p_n)^2 \right]$ for the reaction $\pi^- p \rightarrow \pi^o \pi^o n$ for all momenta combined is shown in Fig. 19, both for data corrected and uncorrected for neutron inelastic scattering effects. The distribution peaks sharply at small t values, indicating that the reaction is indeed peripheral. Figure 20a displays the dipion invariant mass (again for all momenta) for dipion c.m. production angles having cosines greater than 0.8. This cut restricts the events to the peripheral region enhancing the π-π interaction. A phase space curve normalized to the total number of events and reflecting the neutron counter geometric

(a)

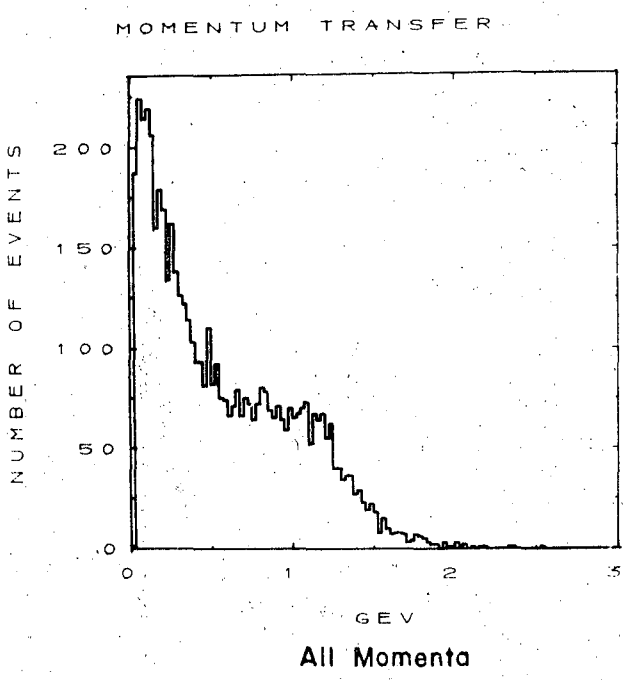

(b)

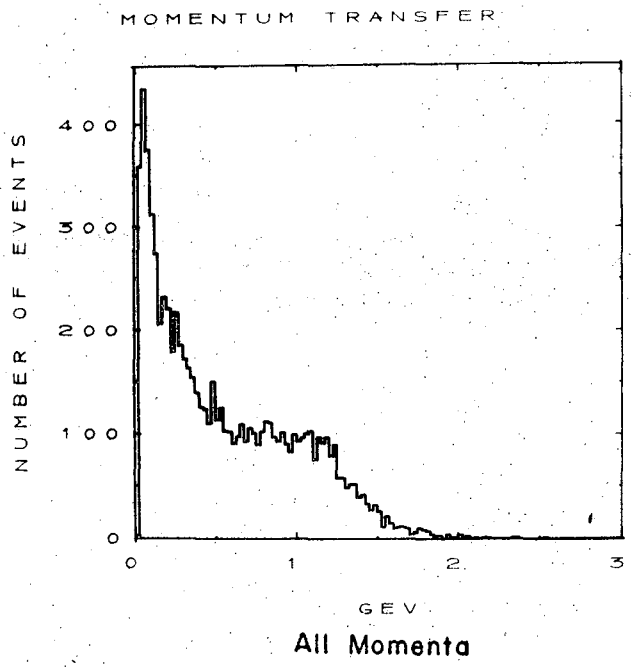

XBL 722-230

Fig. 19a. The momentum transfer distribution for all momenta combined (no corrections).

Fig. 19b. The momentum transfer distribution for all momenta combined corrected on an event by event basis for neutron scattering and nonuniformity of the neutron detection efficiency.

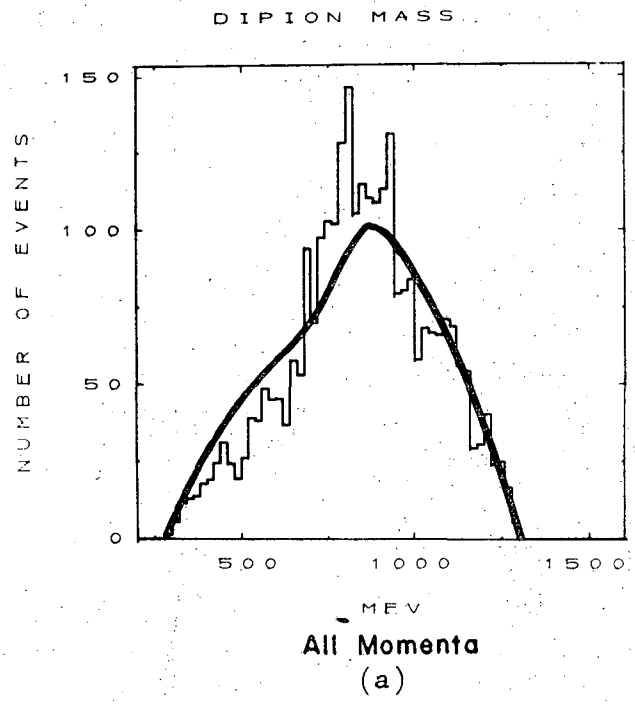

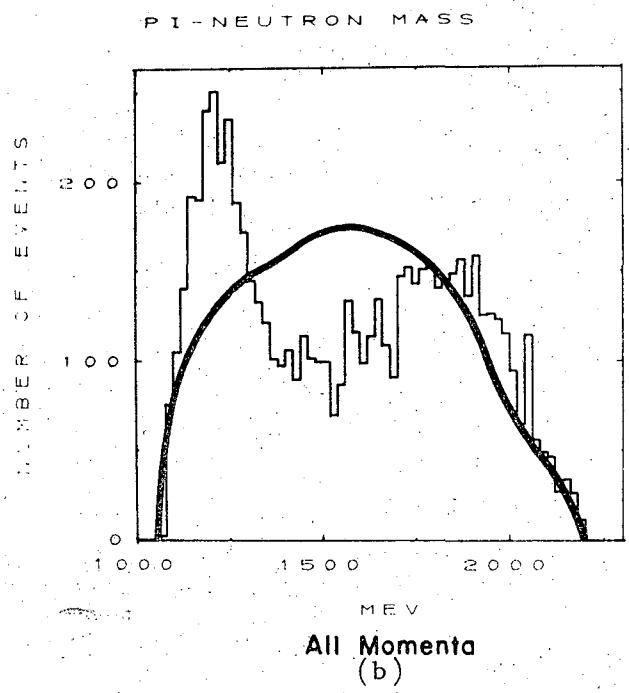

XBL 722-307

Fig. 20. (a) Dipion mass (corrected data) with phase space curve superimposed.
(b) Invariant mass of (π^on) showing both combinations of π^on, with phase space curve superimposed (corrected data).

acceptance has been superimposed. Figure 20b shows the n-π^o invariant mass, again for the peripheral region, and indicates a strong $\Delta(1238)$ contribution. To isolate the π-π interaction in the further study of the data, a cut was made on the n-π^o invariant mass from 1.1 GeV to 1.3 GeV. All data were investigated with and without this cut.

The cosine of the neutron production angle in the c.m. with respect to the proton direction is displayed in Fig. 21, while the t and $(t - t_{min})$ where t_{min} was the minimum momentum transfer possible for a given dipion mass, distributions are displayed in Figs. 22 and 23 respectively. Separate distributions are shown for each of the incident beam momenta, as well as the totality of all the data. A strong peaking is observed for small t, and neutron production angles close to zero degrees, indicating that the one-pion exchange model had some degree of validity in describing the reaction. In Fig. 24 is displayed the t-distribution after a cut had been made on the invariant mass of the $(n\text{-}\pi)$ system. This cut removed those events for which either combination of the $(n\text{-}\pi)$ invariant mass was between 1100 and 1300 MeV. The data still exhibits its peripheral behaviour after this cut.

Figure 25 shows the t distribution for the corrected data as a function of the π-π mass for all momenta. It was noted that under 1 GeV of the $\pi\pi$ mass the distributions appeared similar, while above 1 GeV the distribution has a much less peripheral behaviour. The t distribution for all events having a $\pi\pi$ mass below 1 GeV is displayed in Fig. 25f. Figure 26 shows the same data with a cut in the n-π invariant mass straddling the $\Delta(1238)$ region.

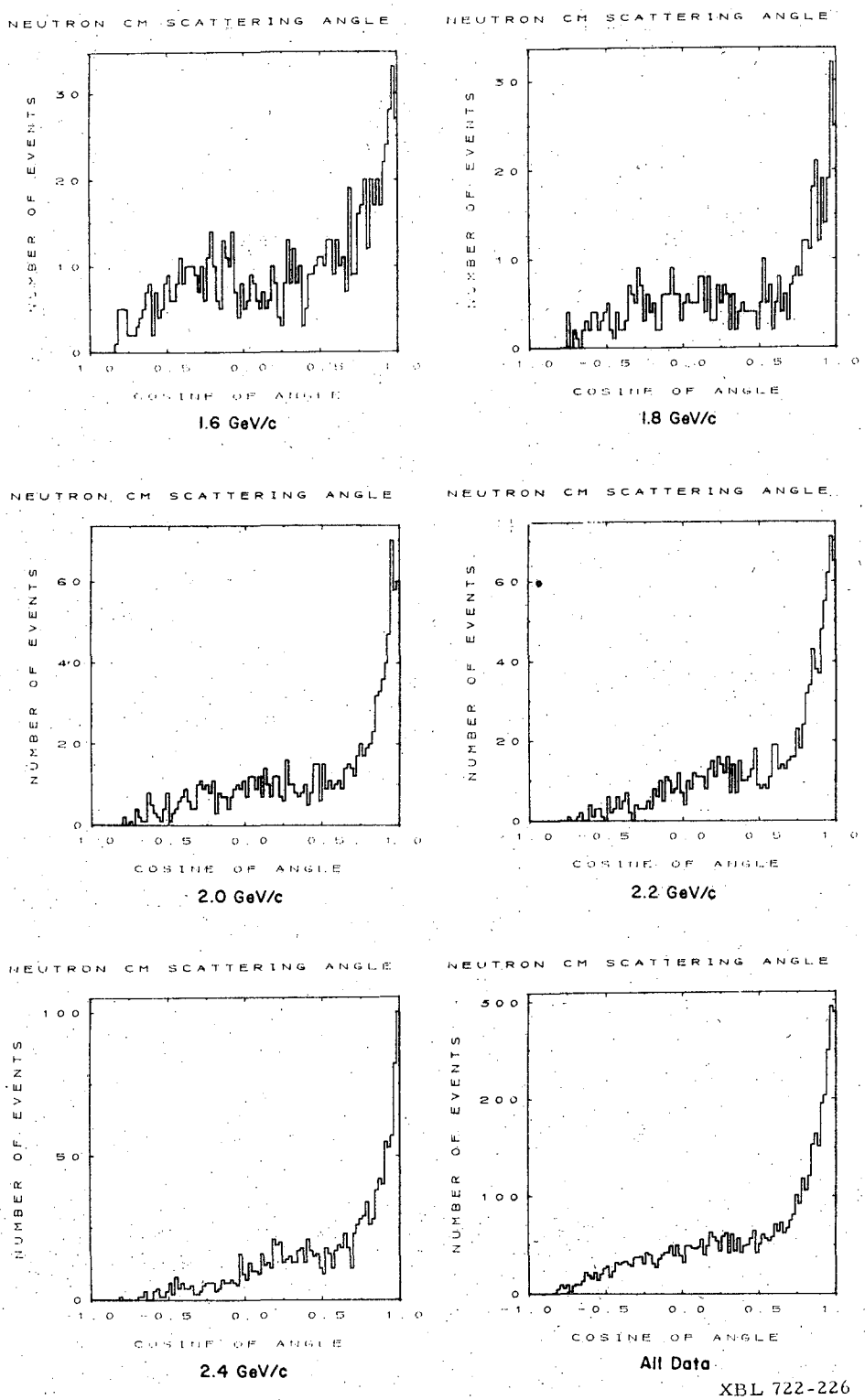

Fig. 21a. Neutron c.m. scattering angle with respect to the proton direction (uncorrected data).

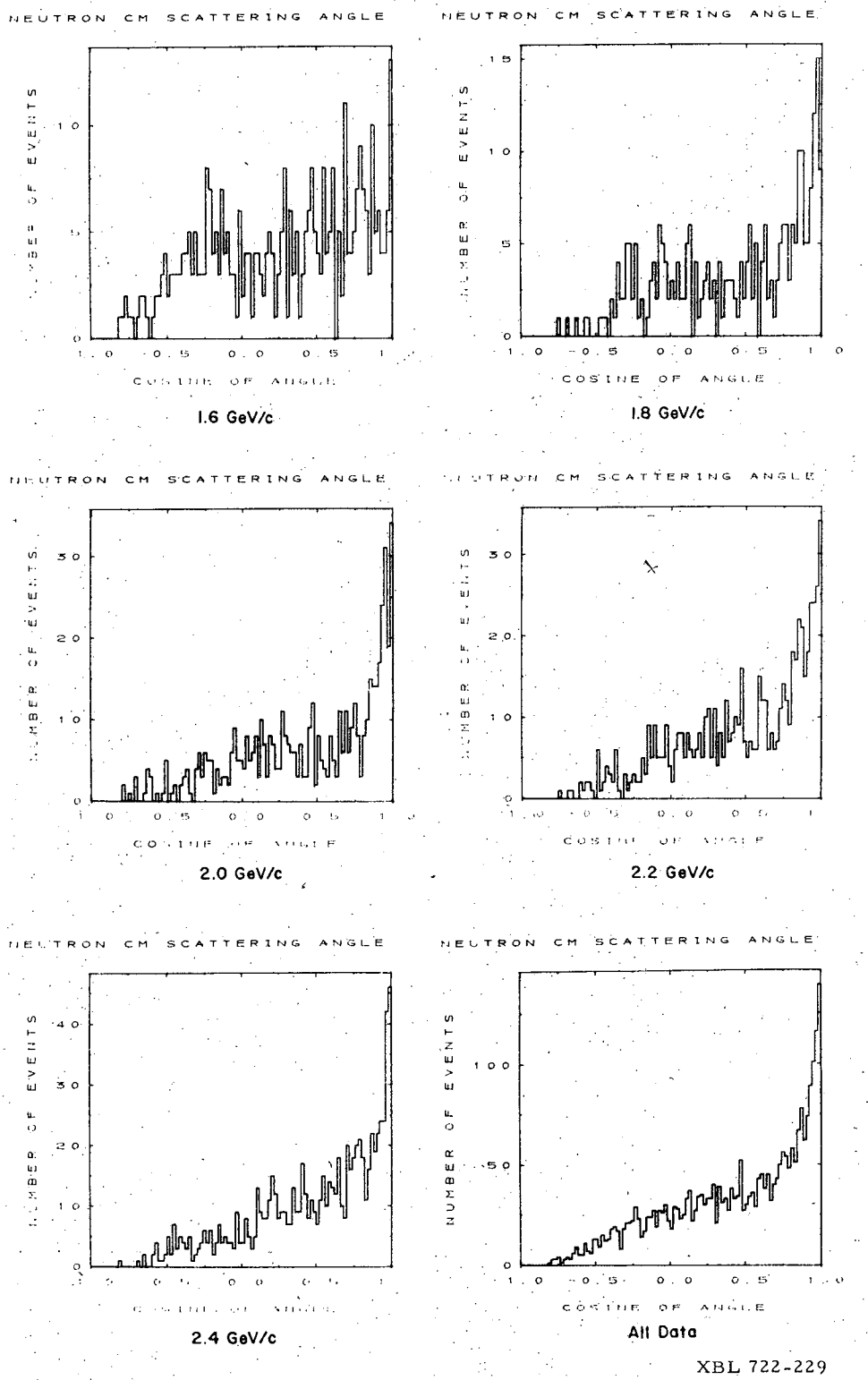

Fig. 21b. Neutron c.m. scattering angle with respect to the proton direction after the $\Delta(1238)$ cut.

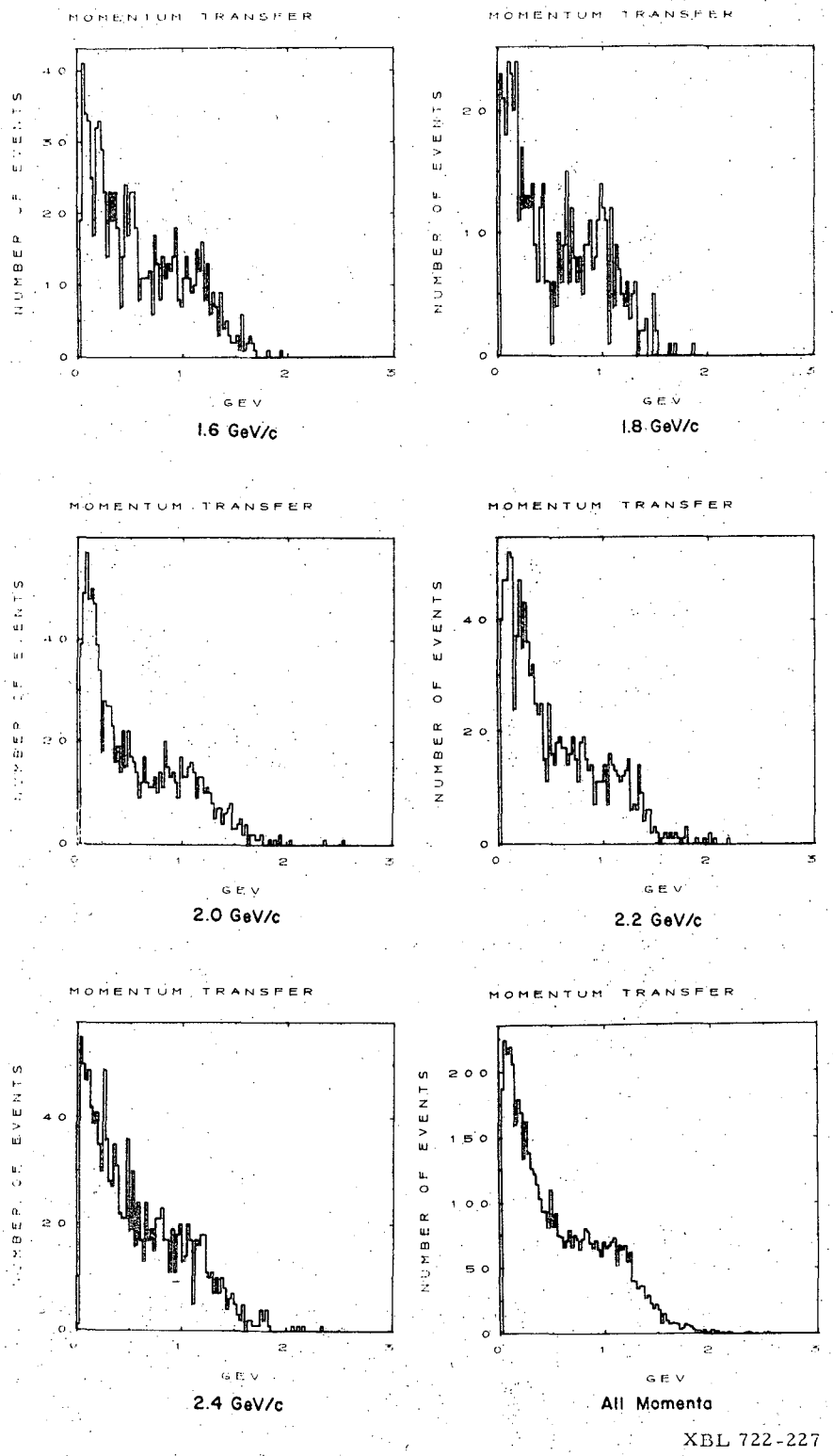

Fig. 22. Momentum transfer distributions (uncorrected data).

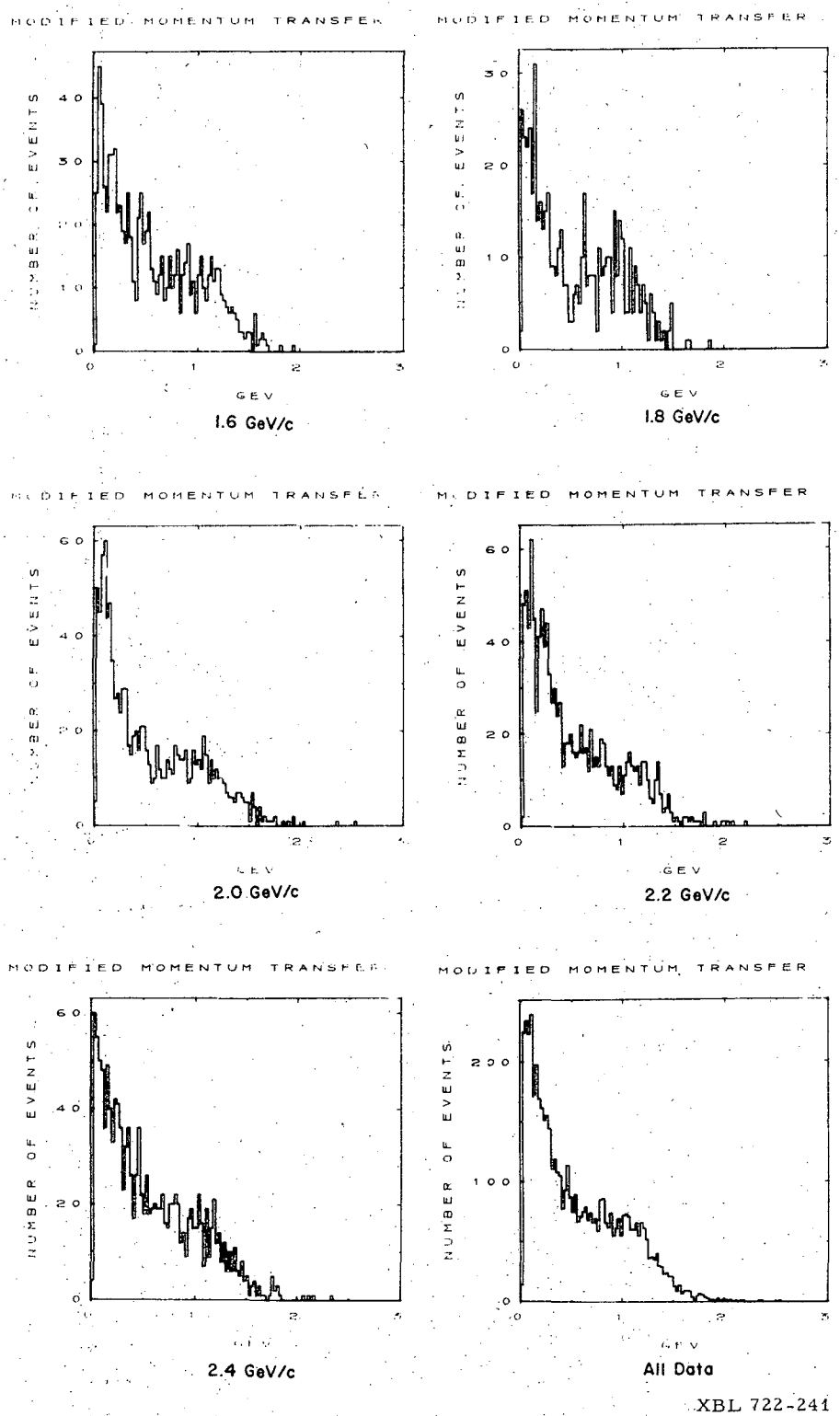

Fig. 23. Distribution of events for $(t - t_{min})$(uncorrected data).

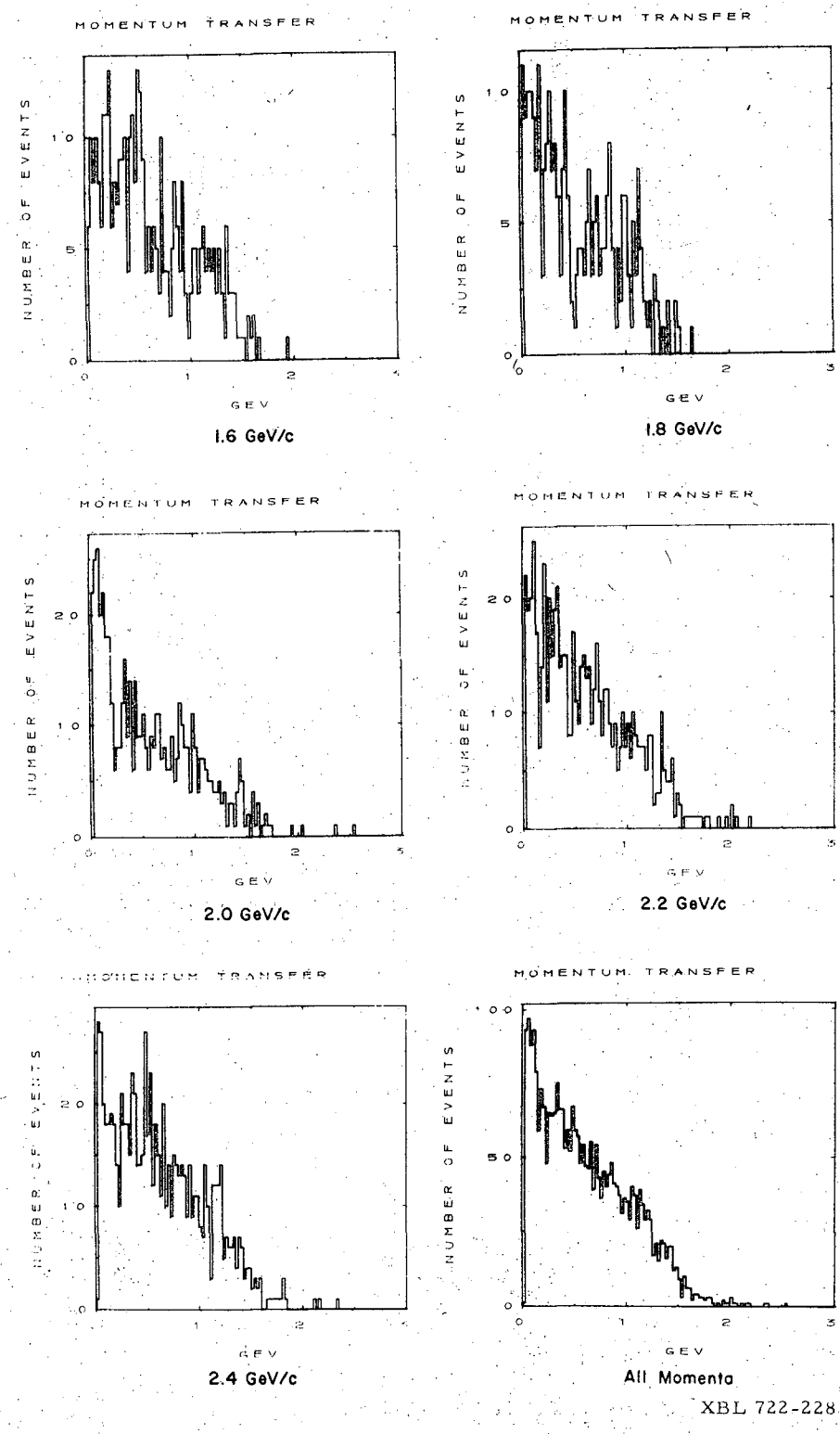

Fig. 24a. The momentum transfer distributions after a $\Delta(1238)$ cut (uncorrected data).

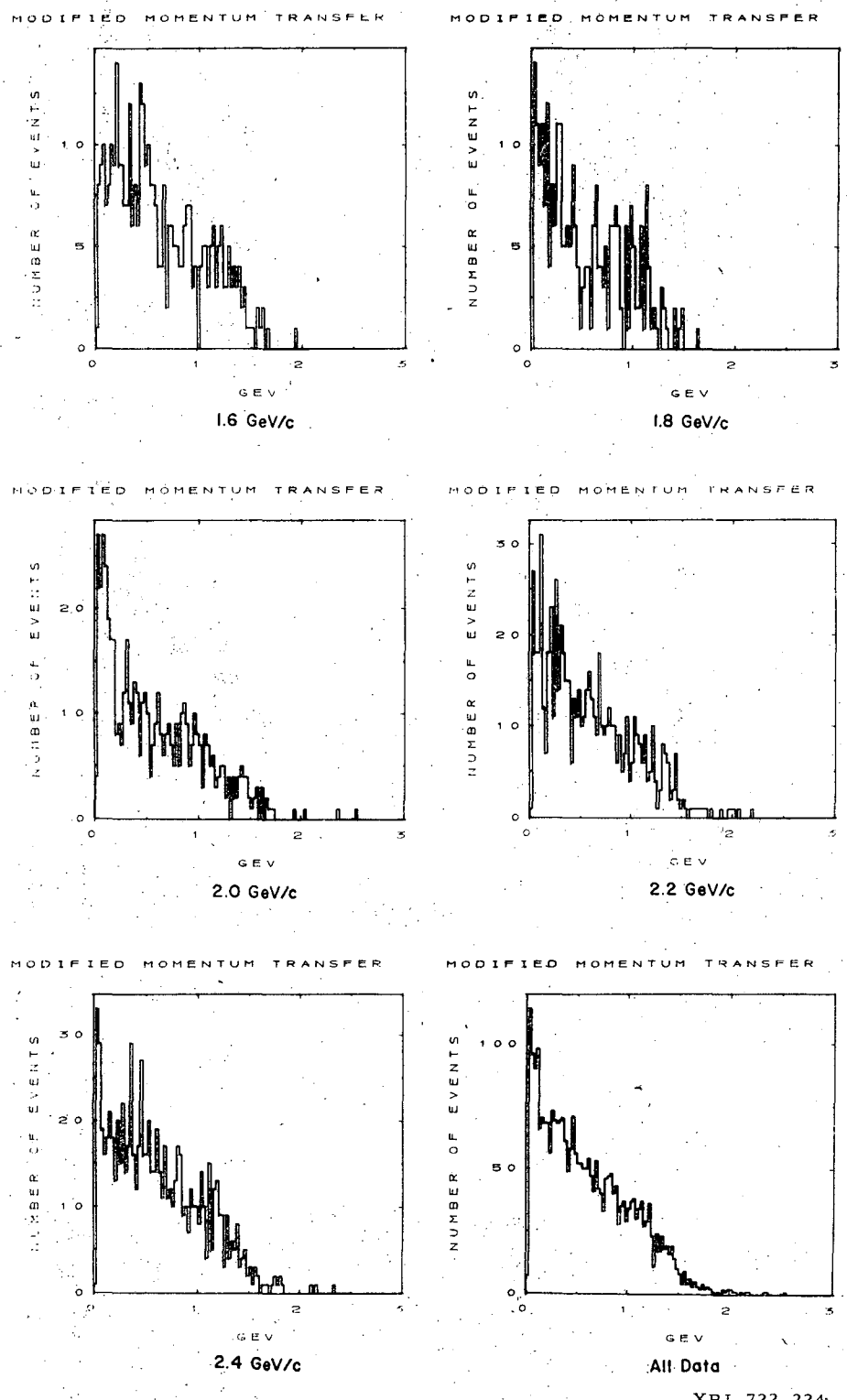

XBL 722-224

Fig. 24b. Distribution of events in $(t - t_{min})$ after a $\Delta(1238)$ cut (uncorrected data).

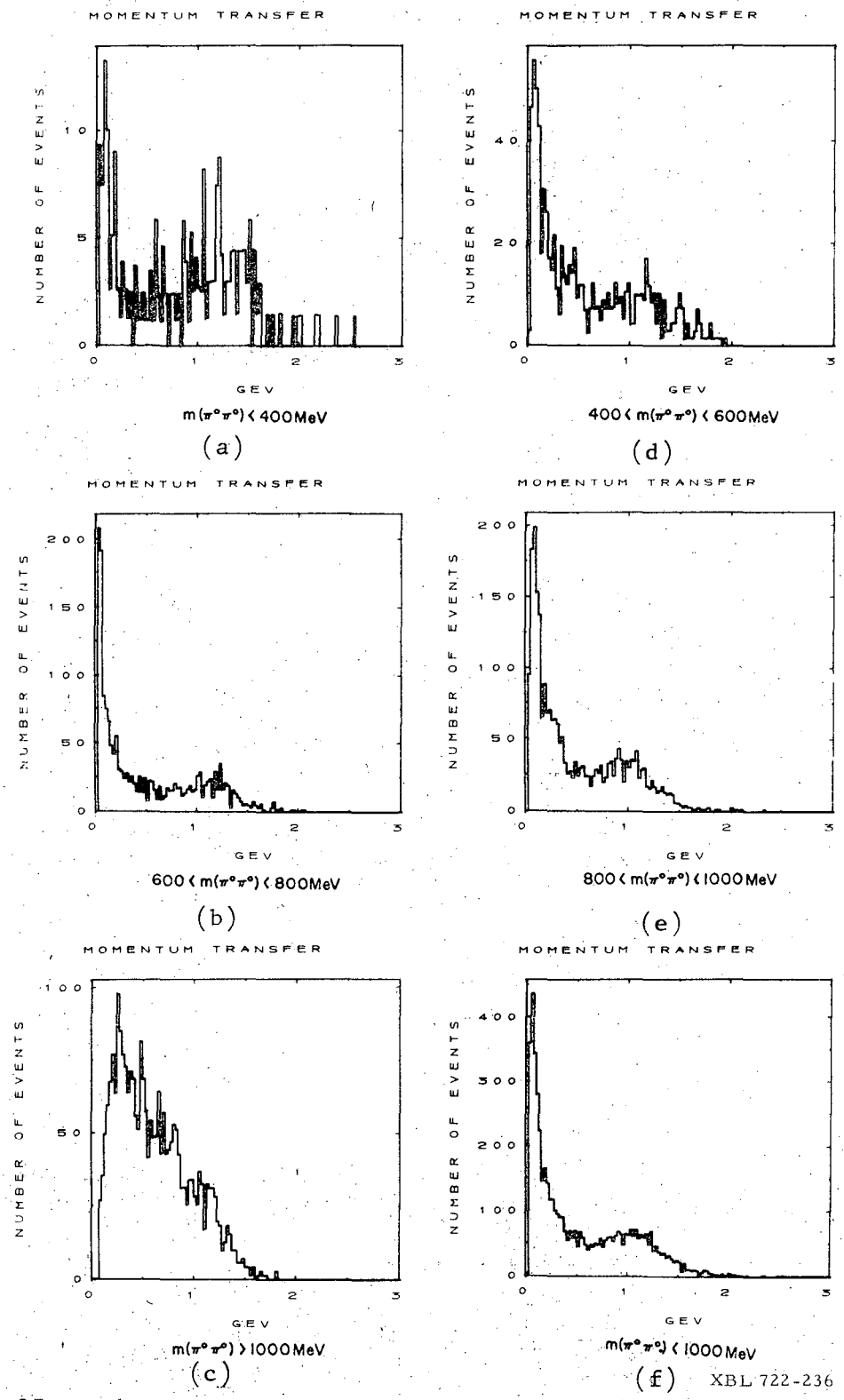

XBL 722-236

Fig. 25. The momentum transfer distributions as a function of the dipion mass (corrected data).

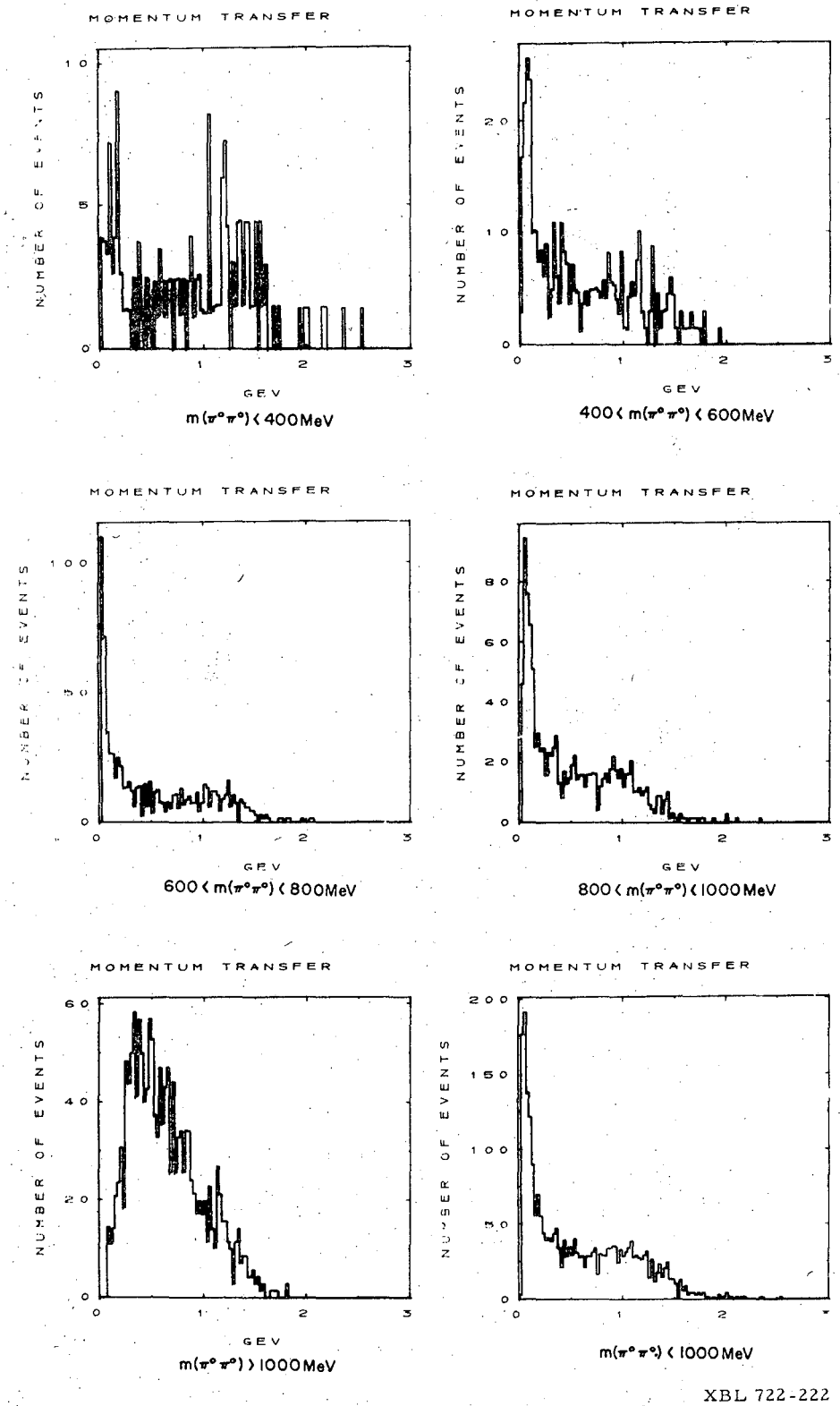

Fig. 26. The momentum transfer distributions as a function of the dipion mass after a $\Delta(1238)$ cut (corrected data).

The data displayed a definite change in the production angle behaviour for the cosine of the neutron production angle in the 0.8 region. Hence a cut was made to enhance the peripheral nature of the data at this point.

The dipion mass in the peripheral region is shown in Fig. 27 for each of the incident momenta as well as for all momenta combined. The same distributions are shown in Fig. 28 with the $\Delta(1238)$ mass region removed. It should be noted that the π-π phase space peaks for large dipion masses because of the geometric acceptance factor. Thus any enhancements in the dipion spectrum should be considered with this in mind. Figure 29 shows the mass spectrum for all momenta with and without the neutron scattering and neutron counter efficiency corrections. Figure 30 shows the same mass spectrum also corrected for the angular acceptance.

The n-π invariant mass for the peripheral region is displayed in Fig. 31 for each individual momentum, as well as all momenta combined. Figure 32 displays the (n-π) invariant mass spectrum for all momenta with and without the neutron scattering and neutron counter efficiency corrections. A strong enhancement can be observed in the n-π invariant mass spectrum at the mass of the $\Delta(1238)$ indicating that roughly 50% of the final state proceeded via the interaction $\pi^- p \rightarrow \Delta^0 \pi^0 \rightarrow (n\pi^0)\pi^0$. The presence of the strong $\Delta(1238)$ signal made the study of the π-π interaction more difficult.

Figure 33 shows the dipion decay distribution in the dipion rest frame corrected for neutron scattering and neutron counter efficiency. Figure 34 shows the same distributions with the $\Delta(1238)$ mass cut. From Fig. 34 it was apparent that up to dipion masses of 1 GeV the angular distributions were isotropic and that the enhancements in the uncut data

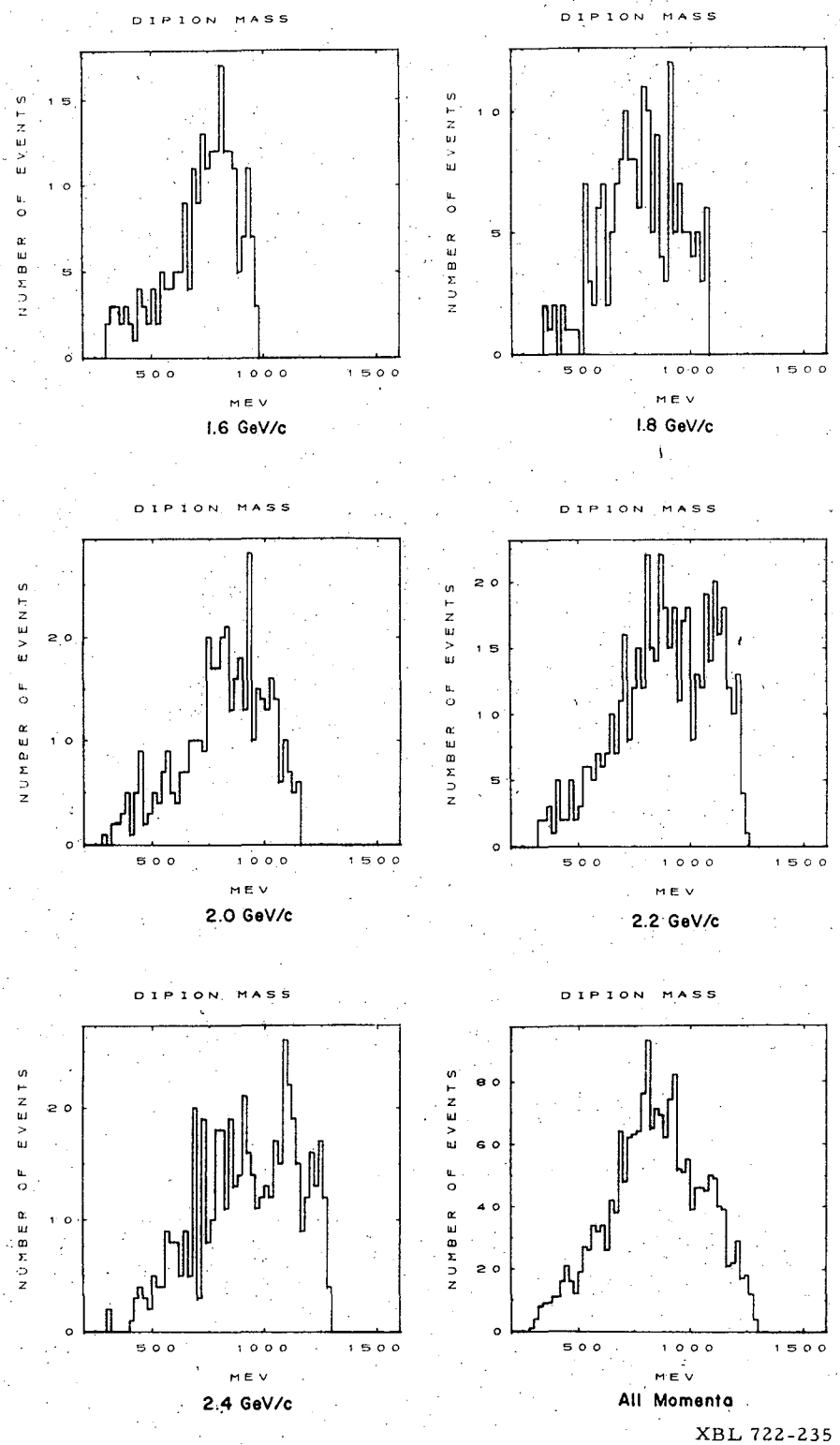

Fig. 27. Dipion mass for the peripheral region (uncorrected data).

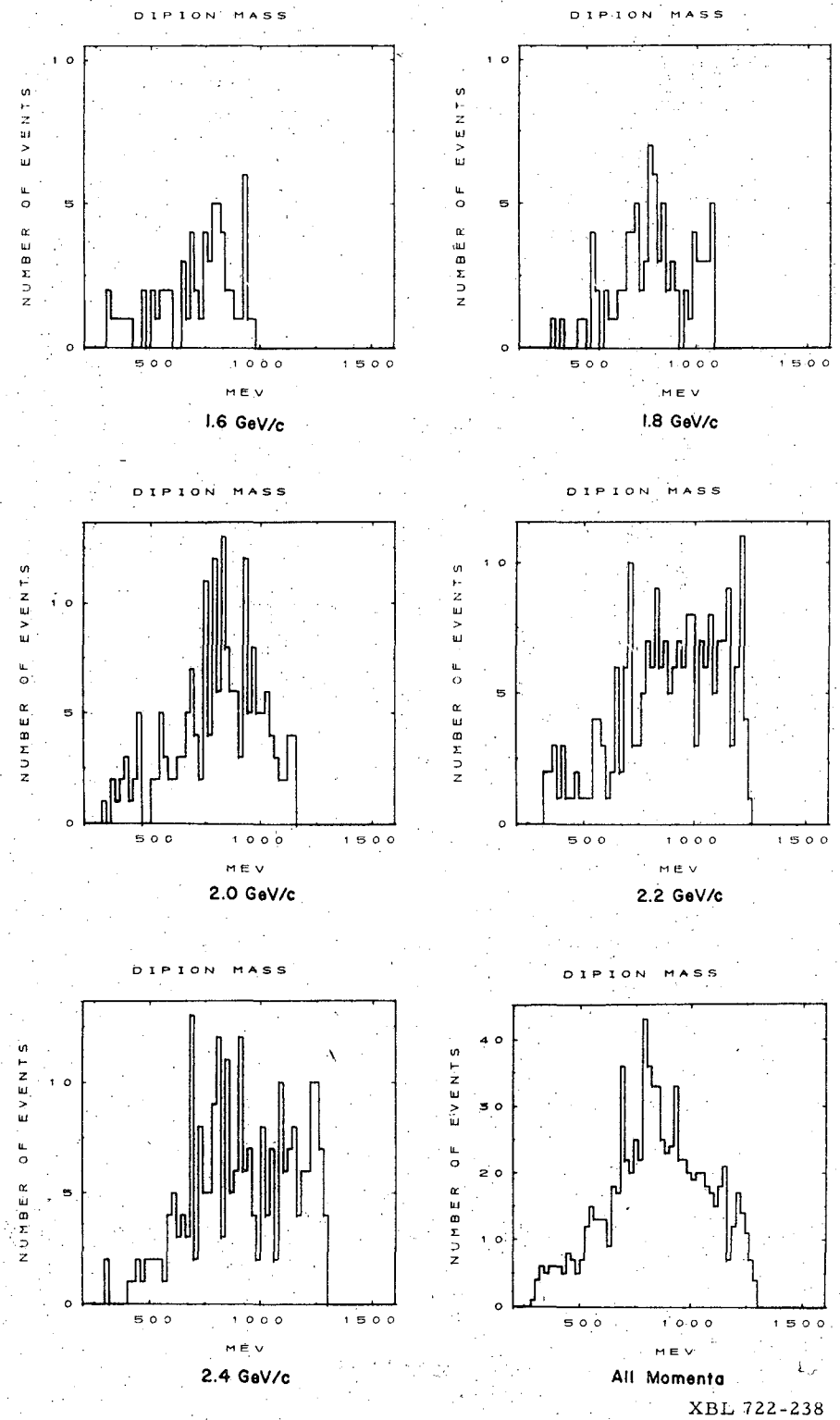

Fig. 28. Dipion mass distributions for the peripheral region after the $\Delta(1238)$ cut (uncorrected data).

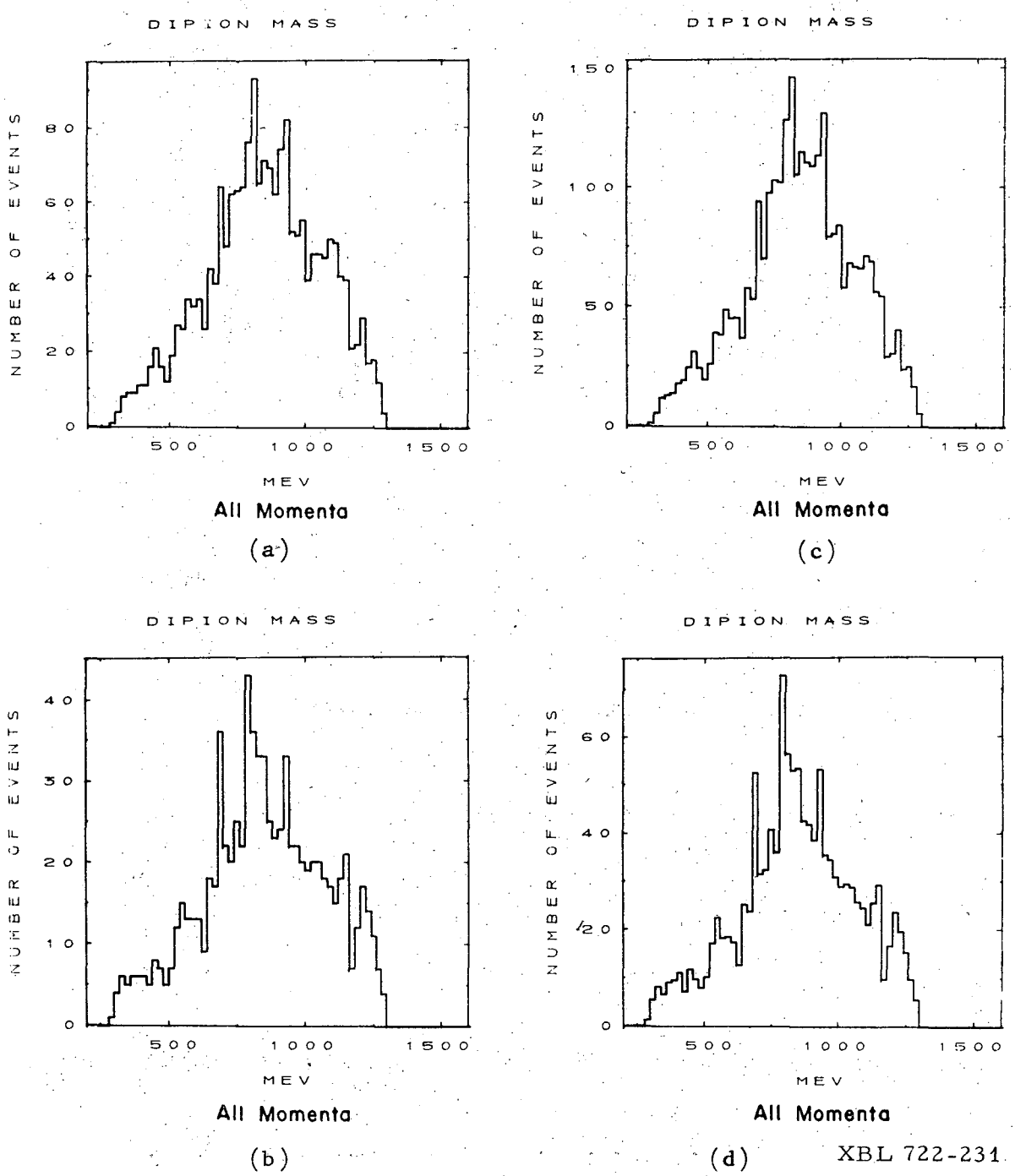

Fig. 29. (a) Dipion mass for all data in the peripheral region (uncorrected)
(b) Dipion mass after the $\Delta(1238)$ cut (uncorrected data)
(c) Dipion mass (corrected data)
(d) Dipion mass after the $\Delta(1238)$ cut (corrected data)

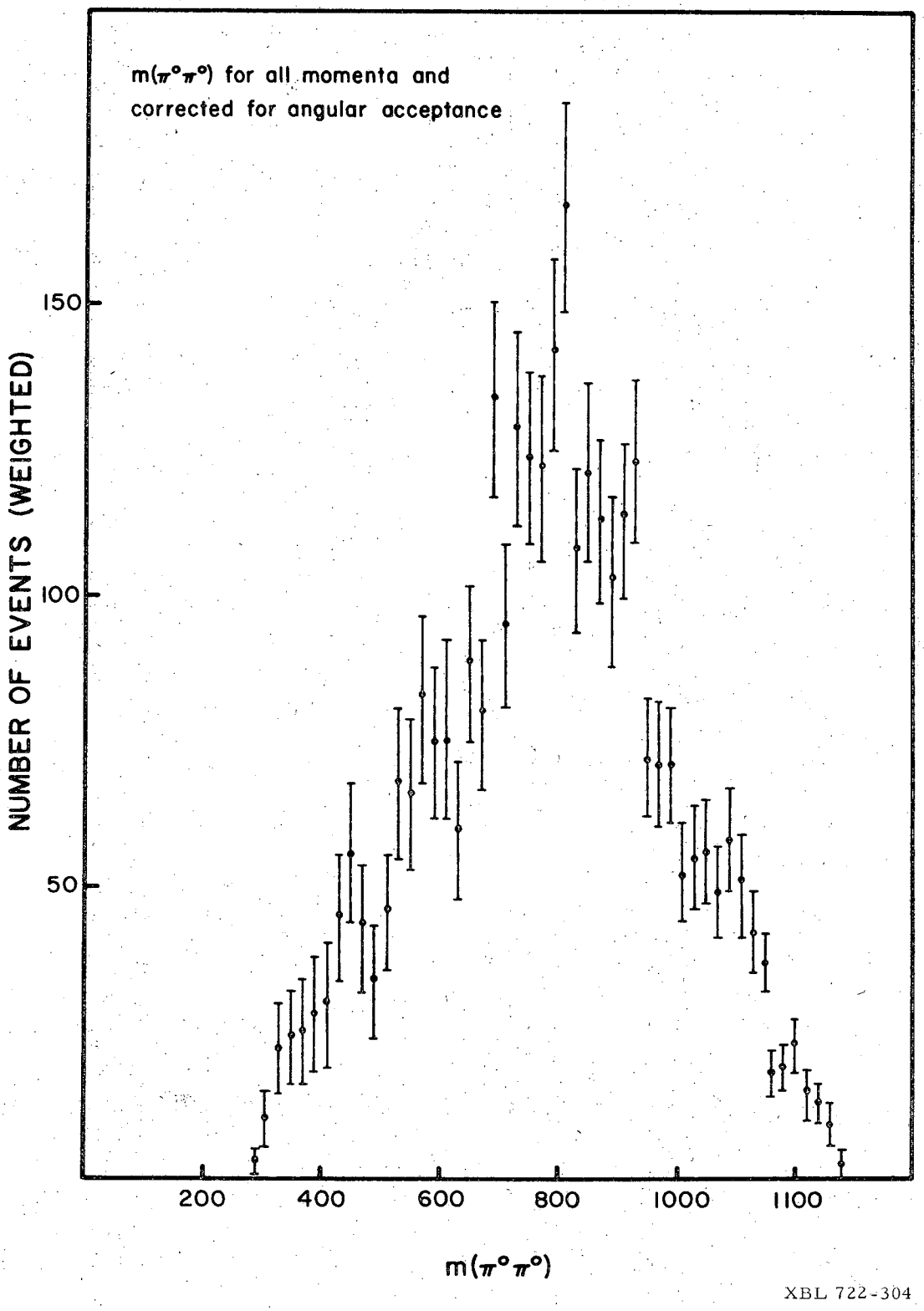

Fig. 30. Dipion mass spectrum (corrected for angular acceptance as well as neutron scattering).

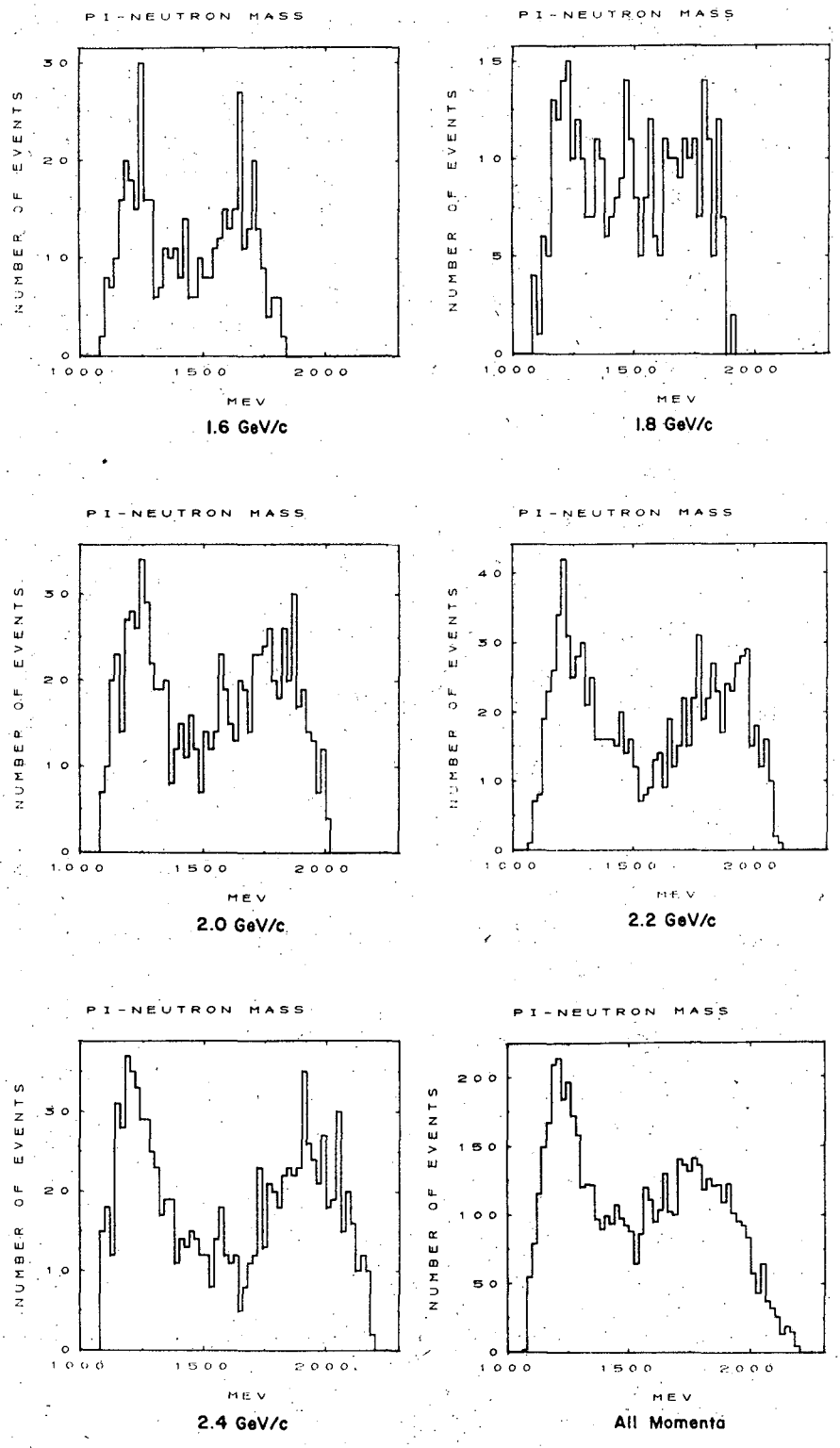

Fig. 31. The invariant mass of $(n\pi^{o})$(uncorrected data).

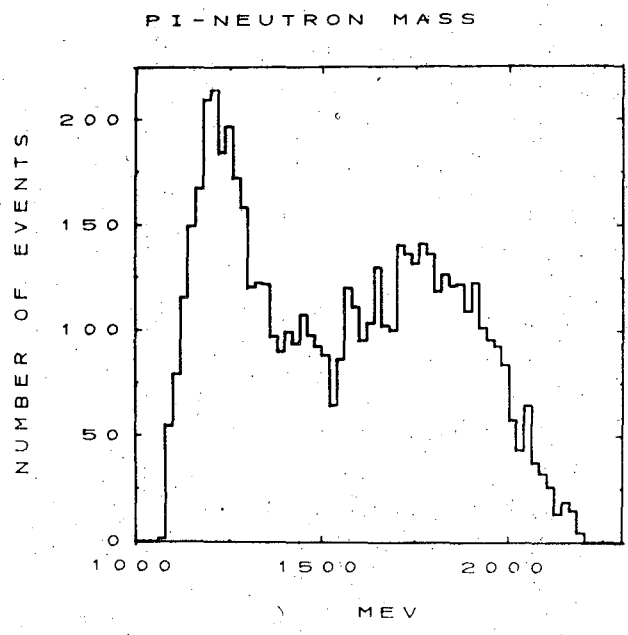

(a)

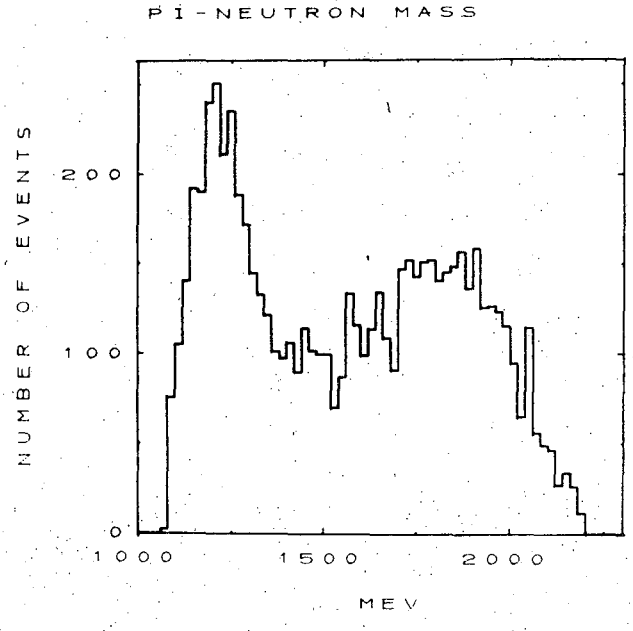

(b)

XBL 722-233

Fig. 32. (a) The invariant mass of the $(n\pi^o)$ for the uncorrected data.
(b) The invariant mass of the $(n\pi^o)$ for the corrected data.

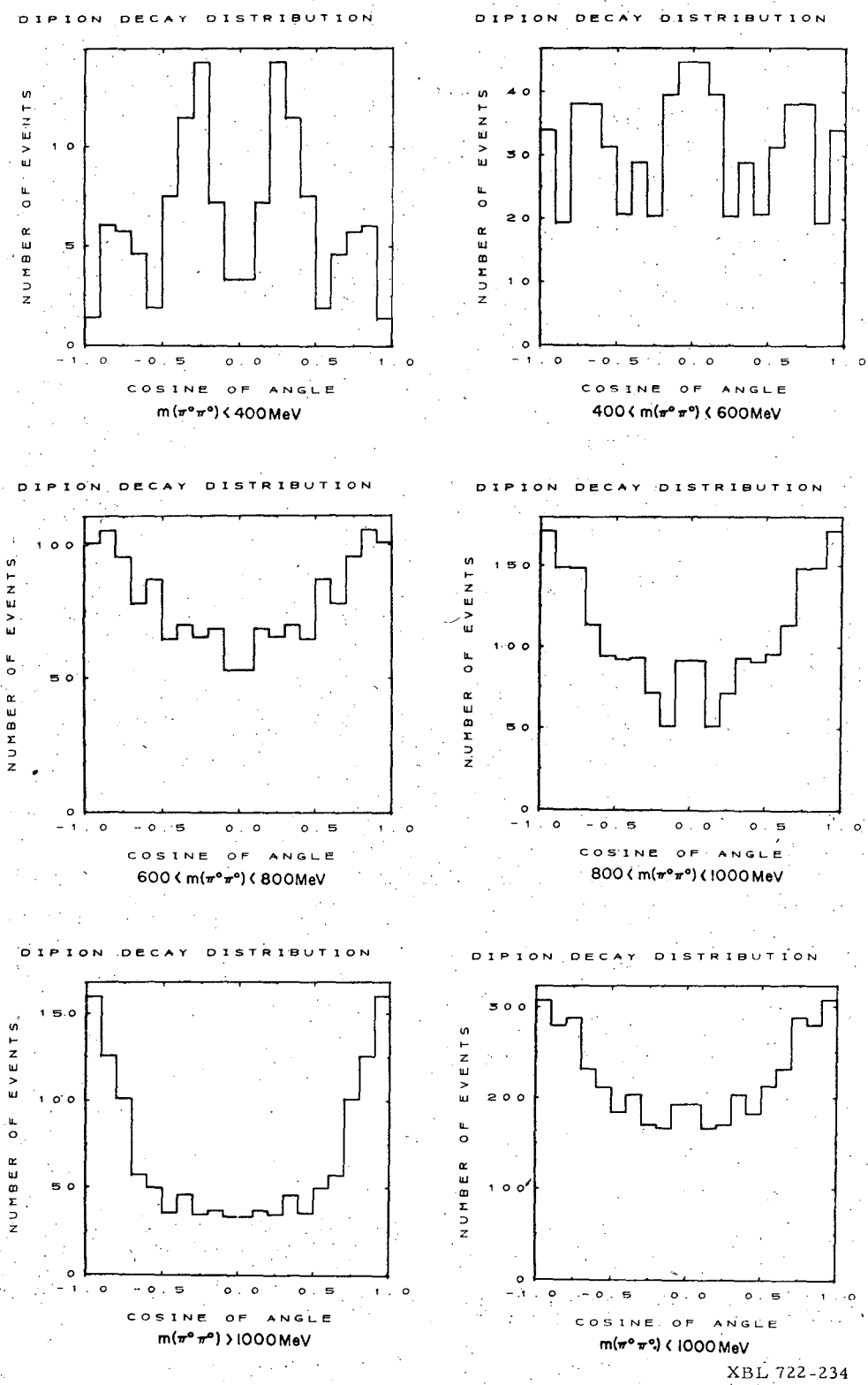

XBL 722-234

Fig. 33. Dipion decay distribution (corrected data).

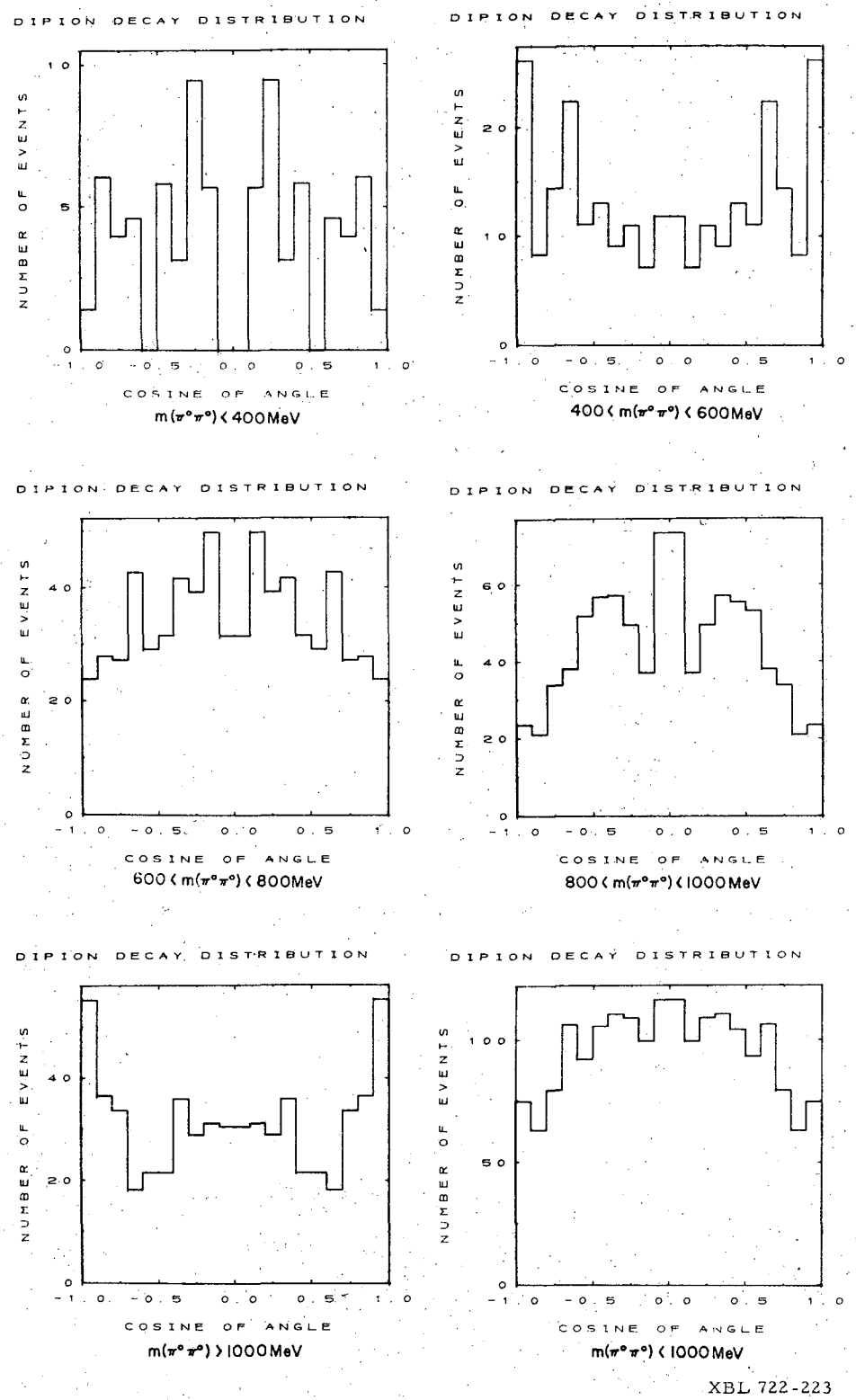

Fig. 34. Dipion decay distributions after the $\Delta(1238)$ cut (corrected data).

for decay angles near zero degrees were due to the $\Delta(1238)$ background. It should be noted that after the $\Delta(1238)$ cut isotropy in the π-π decay angles does not imply a flat angular distribution, but rather one that is depleted for angles near zero degrees. However, above 1 GeV the angular distributions maintain a strong enhancement near dipion decay angles of zero degrees, even after the $\Delta(1238)$ cut indicating a strong d-wave component. This was to be expected, since the $f^{o}(1220)$, a spin 2 particle, begins to dominate the π-π spectrum in this region.

2. Parametrization of the Momentum Transfer Distributions

The data was parametrized in terms of the one pion exchange model. The differential cross-section was written following Eq. (32) as

$$\frac{d^3\sigma}{dtdsd\Omega_{\pi\pi}} = \frac{1}{(4\pi)^2}\,\frac{1}{2}\,\frac{1}{M^2P^2_{lab}}\sqrt{s}\,|q|\,g^2\mu^2\,\frac{f(t,s)}{(t-\mu^2)^2}\,\frac{d\sigma}{d\Omega_{\pi\pi}}$$

and a maximum likelihood fit to the data was obtained for the form factor defined as

$$f(t) = \frac{|t|}{\mu^2}\,e^{\,a(t-\mu^2)}$$

where the factor $|t|/\mu^2$ originated from the p-n coupling in the one pion exchange model, and $e^{a(t-\mu^2)}$ was introduced to account for absorption in an approximate way.

As already stated, it was observed that the $n\pi^o\pi^o$ final state contained a large $\Delta(1238)$ signal which also appeared to be strongly peaked for small $t = (p_n - p_p)^2$ values. To obtain the one pion exchange parameters uncontaminated by the Δ background a cut was imposed on the $(n\pi^o)$ invariant mass before a fit was made to the t distributions. In addition since only the $\pi\pi$ scattering parameters were desired, the fit was obtained for the peripheral region only restricting the events to the momentum transfer region for which $-0.2 < t < t_{cut\text{-}off}$, where $t_{cut\text{-}off} = -0.029$ GeV, and was due to the timing cuts.

The LBL Group A maximum likelihood fitting routine OPTIME was used to obtain the fits. The program did a fit on an event by event basis comparing the data to a set of Monte Carlo four vectors for the $n\pi^o\pi^o$ final state incorporating all the geometric and kinematic cuts of the data. In this way if the Monte Carlo events correctly reflected the kinematics of the data no biases were introduced into the fits as a consequence of the neutron counter acceptance and efficiency as well as the timing gate cuts. Similarly the $(n\text{-}\pi)$ mass cut and the momentum

transfer cut did not bias the fit if the Monte Carlo integration points were subject to the same cuts.

Fits were made to the data in three different t regions

a. $-0.27 < t < t_c$

b. $-0.19 < t < t_c$

c. $-0.10 < t < t_c$

and the results were compared. It was found that for regions b and c they were quite similar, while for region a they differed from those of b and c. In addition it was found that good fits to the momentum transfer distribution h(t), where $h(t) = f(t)/(t - \mu^2)^2$ were obtained only in the region below 1 GeV of the dipion mass, while for dipion masses larger than 1 GeV fits could be obtained to the functional form $h'(t) = e^{a(t - \mu^2)}$, where the dipion pole term had been excluded. The fact that the momentum transfer distribution changed above 1 GeV indicated that the one-pion exchange model was starting to lose its validity in this region, where the available kinetic energy was getting smaller and peripheral production was not necessarily expected to be valid. The results of the fit are shown in Table IX.

Table IX. Fit parameters for the t distributions.

t region	m < 1000 MeV $h(t) = \frac{e^{a(t - u^2)}}{(t - u^2)^2} \frac{\lvert t \rvert}{\mu^2}$	m > 1000 MeV $h(t) = e^{a(t - u^2)}$
$-0.27 - t_c$	$a = 3.5 \pm 0.6$	
$-0.19 - t_c$	$a = 5.68 \pm 1.0$	
$-0.10 - t_c$	$a = 5.55 \pm 1.0$	$a = 1.06 \pm 0.2$

The fit was done for all momenta combined, and then the resulting fit compared for each individual momentum for normalization and for the goodness of the fit.

The results of the fit have been displayed in Figs. 35 through 36.

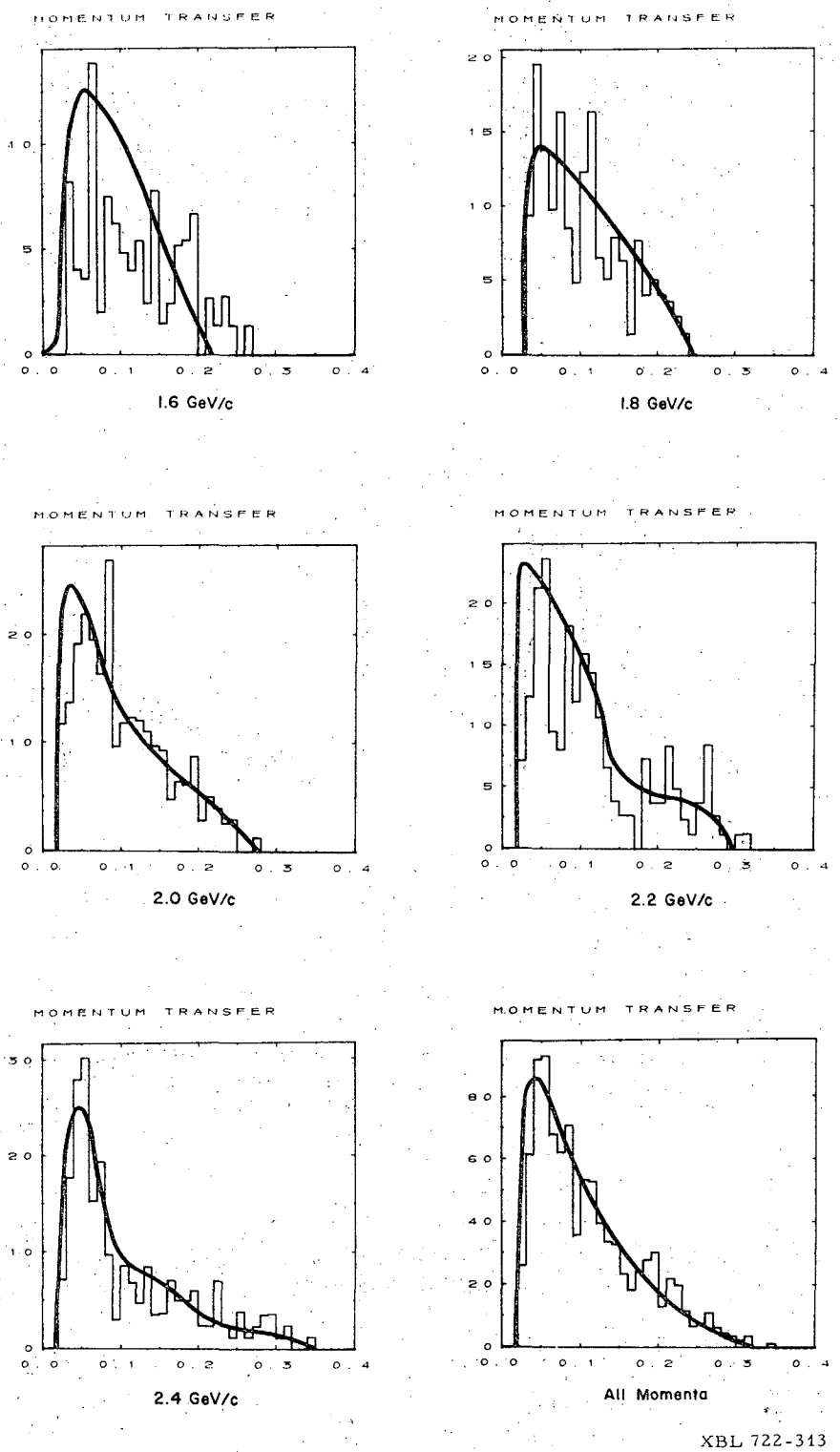

XBL 722-313

Fig. 35. Fits to the t distributions. The data is for those events having a dipion production angle whose cosine is greater than 0.8. The parameters for the form factors were obtained in the fit to the t region ($-.19 < t < -.029$) and then the resulting curves using Monte Carlo points corresponding to the histogram data were integrated and normalized to the number of events in each histogram.

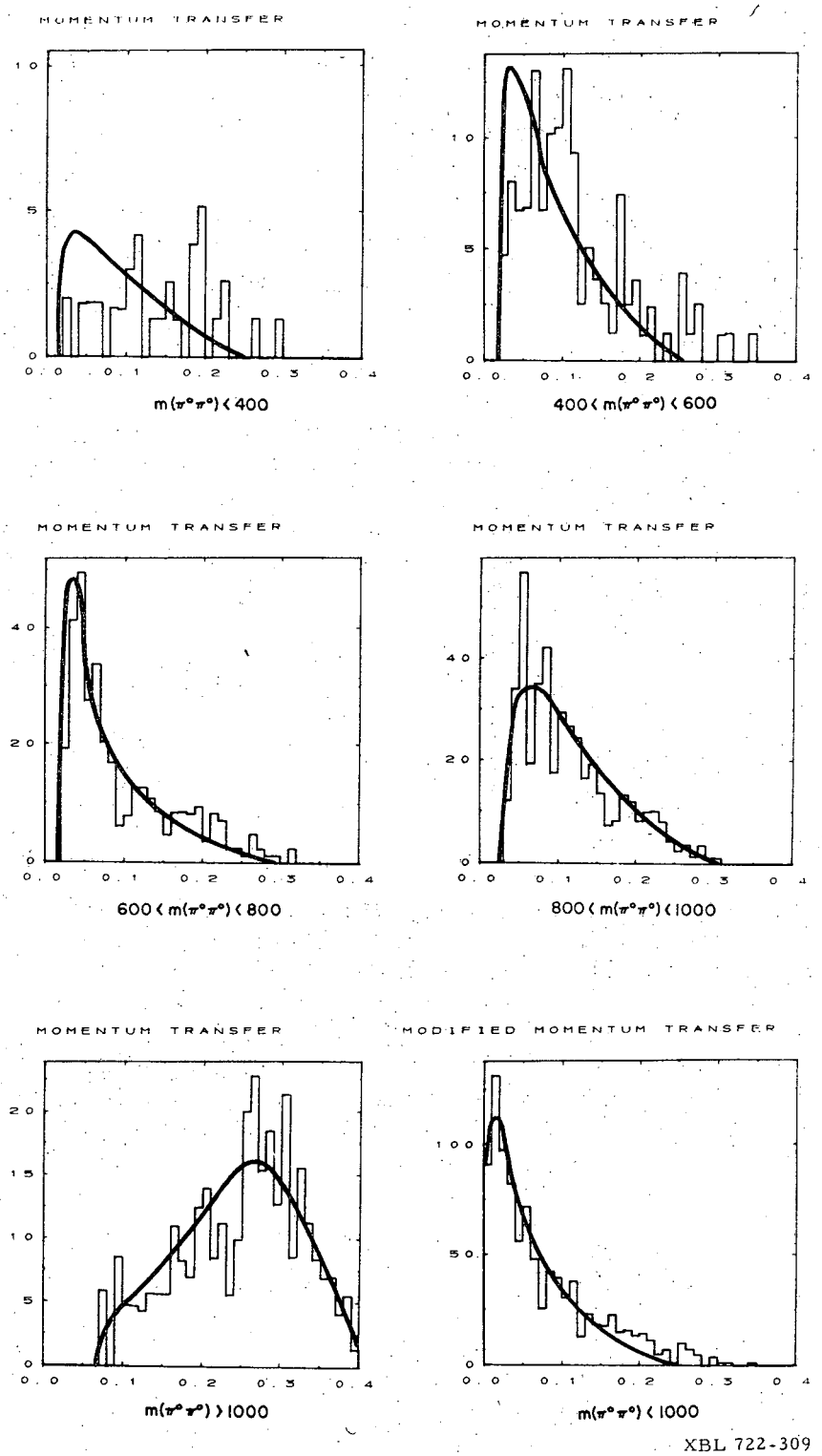

Fig. 36. Fits to the t distributions. The data is for those events having a dipion production angle whose cosine is greater than 0.8. The parameters for the form factors were obtained in the fit to the t region ($-.19 < t < -.029$) and then the resulting curves using Monte Carlo points corresponding to the histogram data were integrated and normalized to the number of events in each histogram. The figure on the lower right-hand side shows the $|t - t_{min}|$ distribution.

For these figures, the parametrization of the t distribution obtained for the t region ($-0.19 < t < t_c$) have been superimposed on a data sample corresponding to a larger t interval, namely data having a dipion production angle whose cosine was greater than 0.8. The points for the curves were obtained by a Monte Carlo integration of the momentum transfer functions obtained in the fit, and a smooth curve estimated from the Monte Carlo points.

The overall fit of $h(t) = \frac{e^{a(t - u^2)}}{(t - u^2)^2} (\frac{-t}{\mu^2})$ to the t distribution is shown in Fig. 35, the fit as a function of the incident π^- momentum. Figure 36 shows the fit as a function of the dipion mass. For masses greater than 1 GeV, Fig. 36 shows the fit for the form factor $e^{a(t - u^2)}$, with a set to 1.06. The $t' = (t - t_{min})$ distribution also was fit adequately by the same parametrization. The fits for this variable are shown in Fig. 36.

3. The π-π Scattering Cross-Sections

The π-π scattering matrix element and phase shifts were obtained using the form factors found for $m_{\pi^o\pi^o} < 1$ GeV for the peripheral region. This did not represent the production distribution above 1 GeV very well, but since the t cut imposed to extract the I = 0, J = 0 scattering cross-sections eliminated most of the high mass region, any discrepancies introduced by using the form factors for the region below 1 GeV were considered to be minimal.

Integrating Eq. (32) over the solid angle, and accounting for the Bose statistics symmetry, one obtains

$$\frac{\partial^2\sigma}{\partial t \partial s} = \frac{1}{(4\pi)^2} \cdot \frac{1}{2} \cdot \frac{1}{M^2 P^2_{lab}} \cdot \sqrt{s}\, |q|\, g^2 \mu^2 \frac{f(t,s)}{(t - u^2)^2}$$

$$\times \frac{4\pi}{|q'|^2} \frac{2}{9} \sin^2 (\delta^o_o - \delta^2_o)$$

$$\sin^2(\delta_o^o - \delta_o^2) = \frac{36\pi}{2} \cdot 2 \cdot \frac{1}{\frac{g^2}{M^2}\frac{\mu^2}{M^2}} \cdot \frac{|q'|^2}{\sqrt{s}} \frac{|p_{lab}|^2}{|q|} \frac{(t - \mu^2)^2}{f(t,s)} \frac{d^2\sigma}{dsdt}$$

and setting

$$ds = 2\sqrt{s}\, dm \qquad (\text{where } m = m_{\pi^o\pi^o})$$

yields

$$\sin^2(\delta_o^o - \delta_o^2) = 18\pi \frac{1}{g^2 \frac{\mu^2}{M^2}} \frac{|q'|^2 |p_{lab}|^2}{s\,|q|} \frac{(t - u^2)^2}{f(t,s)} \frac{d^2\sigma}{dm_{\pi\pi}\partial t}$$

Furthermore

$$\frac{\partial^2\sigma}{\partial m_{\pi\pi}\partial t} = \sigma_{total} \lim_{\substack{\Delta m \to 0 \\ \Delta t \to 0}} \frac{1}{n_{total}} \left\{ \frac{n(m + \Delta m,\ t + \Delta t) - n(m,t)}{\Delta m \Delta t} \right\}$$

where $n(m,t)$ is the number of events with mass m, and momentum transfer t; while n_{total} is the total number of events observed in the reaction at a given momentum.

Hence

$$\sin^2(\delta_o^o - \delta_o^2) = \frac{9}{16} \frac{1}{\frac{g^2}{32\pi}\frac{u^2}{M^2}} \frac{|q'|^2}{s} \frac{|p_{lab}|^2}{|q|} \frac{(t - u^2)}{f(t,s)} \frac{\sigma_{total}}{n_{total}} \left\{ \lim_{\substack{\Delta m \to 0 \\ \Delta t \to 0}} \frac{\Delta n(m,t)}{\Delta m \Delta t} \right\}$$

and changing the order of taking the limit, and setting

$$\frac{g^2 u^2}{32\pi M^2} = f^2, \qquad (f^2 = 0.0822)$$

$$\sin^2(\delta_o^o - \delta_o^2) = \frac{9}{16} \cdot \frac{1}{f^2} \frac{\sigma_{total}}{m_{total}} \lim_{\substack{\Delta m_i \to 0 \\ \Delta t_j \to 0}}$$

$$\left\{ \frac{1}{\Delta m_i \Delta t_j} \sum_{\substack{\text{events in} \\ \Delta m \Delta t}} \frac{|q'|^2 |p_{lab}|^2}{s|q|} \frac{(t - u^2)^2}{f(t,s)} \right\}$$

where we summed over all events in ith mass bin and the jth momentum transfer bin. Then an average value of $\sin^2(\delta_o^o - \delta_o^2)$ in the region $\left\{(m_i, t_j),\ (m_i + \Delta m,\ t_j + \Delta t)\right\}$ could be obtained by removing the limit.

$$\sin^2(\delta_o^o - \delta_o^2)_{ij} = \frac{9}{16}\frac{1}{f^2} \cdot \frac{\sigma_{total}}{n_{total}} \frac{\Delta^2 d_{ij}(m,t)}{\Delta m_i \Delta t_j}$$

where

$$\Delta^2 d_{ij}(m,t) = \sum \frac{|q'|^2 |p_{lab}|^2}{s\,|q|} \frac{(t - \mu^2)^2}{f(t,s)}$$

The data with the neutron counter coincidence in the spark chamber trigger was used to calculate the π-π scattering cross-sections. As already outlined this data excluded certain categories of events:

a. neutrons with $\beta < 0.17$

b. neutrons with $\beta > 0.85$ (the PPK timing cut)

c. neutrons with production angles outside the angular region subtended by the neutron counters (12 deg to 72 deg in the lab)

In addition events were excluded because of

d. neutron inelastic scattering in the spark chambers

e. geometric acceptance of the neutron counters

f. efficiency for the detection of neutrons by the neutron counters.

Finally a cut was imposed on the data corresponding to the $\Delta(1238)$ region

g. if the invariant mass of either combination of n-π^o was in the region 1.1 to 1.3 GeV the event was not considered.

Since the confidence level cuts (see Sec. V) eliminated a large sample of the events passing the kinematic fitting routine SIOUX, it was felt that the absolute normalization of the data taken in the normal trigger mode was unreliable. However, since the total cross-section for $\pi p \rightarrow \pi^o \pi^o n$ had already been obtained (see Sec. IV) it was felt that the data could be normalized to this measurement.

To account for the timing cuts and angular cuts corresponding to a, b, and c the total cross-section was normalized to the fraction of events with these cuts imposed. This was done by taking the kinematic-

ally fitted sample of the data without the neutron counter coincidence. in the trigger which did not include these cuts (after the 1% confidence level cuts for this data) to obtain the ratio of events with these cuts imposed to those without the cuts. It was felt that, although the events, without the neutron parameters being determined, had poor resolution, the data was still accurate enough to yield the required ratio to ~ 5%. We set

$$\frac{\text{number of events (velocity and timing cuts, angular cuts)}}{\text{number of events (no cuts)}} = \frac{\text{NFS(cuts)}}{\text{NFS(no cuts)}}$$

To correct for neutron scattering, geometric acceptance, and neutron counter efficiency, the number of events was written as the sum of the weights

$$n_{total} = \sum_i \left(\frac{212}{\eta}\right) \sin\Theta \, \omega^{sc}$$

where i ranged over all the data with the neutron counter coincidence included in the trigger, and where

η = the neutron counter efficiency

$\omega^{sc} = \frac{N_o(\Theta,E)}{N(\Theta,E)}$ = the ratio of events produced at a neutron lab angle of Θ and energy E, to those unscattered for the same Θ and E.

Hence

$$\sin^2(\delta_o^o - \delta_o^2) = \frac{9}{16} \cdot \frac{1}{f^2} \sigma_{total} \frac{\text{NFS(cuts)}}{\text{NFS(no cuts)}} \cdot \frac{1}{n_{total}} \times \frac{\Delta d_{ij}}{\Delta m_i \Delta t_{ij}} \frac{M_{ij}(\text{no cuts})}{M_{ij}(\text{cuts})}$$

$$\Delta d_{ij} = \sum_{\substack{\Delta m_i \\ \Delta t_j^i}} \frac{|q'|^2 |P_{lab}|^2}{s\,|q|} \frac{(t-\mu^2)^2}{f(t,s)} \frac{212}{\eta} \sin\theta \omega^{sc}$$

where Δd_{ij} included an (n-π^o) cuts as well as the timing cuts and the angular cuts imposed by the geometry and the electronics. The repopulation of the number of events in each $\Delta m_i \, \Delta t_j$ bin to account for the

$(n\pi^o)$ cut, the timing cuts and the angular cuts, was obtained from the Monte Carlo events by considering the sums

$$M_{ij}(m,t) = \sum_{\Delta m_i \Delta t_j} \frac{|q'|^2 |P_{lab}|^2}{s\,|q|} \sin\theta$$

with and without the $(n\pi^o)$ cut and the timing cuts imposed. (The angular cut was not considered since it mainly affected the high mass region, which was of little interest in the analysis.)

The expression for $\sin^2(\delta_o^o - \delta_o^2)$ obtained by the method outlined above, was correct for each individual momentum. To obtain a weighted average for all the momenta combined one took the average

$$\sin^2(\delta_o^o - \delta_o^2) = \frac{\sum n_{ip} \sin^2(\delta_o^o - \delta_o^2)_{ip}}{\sum n_{ip}}$$

where the numbers n_{ip} were the number of weighted events at each momentum for the normal trigger data.

The error in $\sin^2(\delta_o^o - \delta_o^2)$ arose from the error in σ_{total} and the statistical fluctuations of the various sums forming the resulting matrix element calculation. In particular, because of the normalization to the data without the neutron counter coincidence in the trigger, the error due to the neutron counter efficiency was not present. This resulted from the assumption that the errors in the efficiency arose mainly from the calculation, which was not detailed enough, and not from the method in which the neutron counters were calibrated. Thus the errors scaled in the same manner for all counters and could be eliminated by division in the determination of $\sin^2(\delta_o^o - \delta_o^2)$.

The square of the matrix element was obtained using a single t region for the calculation for each mass bin of 40 MeV, since there was not enough statistics in the final sample for a good extrapolation to

the pion pole ($t = \mu^2$). The calculation was done for $\Delta t = (-0.19, t_c)$ and $\Delta t = (-0.1, t_c)$ with the same form factor, $e^{a(t - \mu^2)}$, $a = 5.57$. It was found that the resulting square of the matrix element agreed closely for both calculations indicating that if an extrapolation could be made, it would probably yield similar results. Table X displays $\sin^2(\delta_o^o - \delta_o^2)$ as calculated for both Δt intervals, while the results have been graphically presented in Fig. 37.

Figure 38 compares the present solution with that of Sonderegger et al.[26] and Shibata et al.[24] It can be seen that the square of the matrix element does not reach the unitarity limit, but does agree with these previous solutions for the given form factors used in the derivation above 750 MeV of the dipion mass.

If it was assumed that the unitarity limit was not achieved because of the limitations of the form factor model, and that it was but a mere scale factor that prevented the unitarity limit from being attained, a correction could be made by multiplying each point of the matrix element by a constant factor. The resulting phase shifts could then be compared to the solutions of Gutay et al.[19] and Schlein et al.[21] The solution for δ_o^o is presented in Fig. 39 and should be compared to the results presented in Fig. 3. It can be seen after the normalization (which is difficult to justify) the $\pi^o\pi^o$ spectrum is compatible with the down-up solution as shown in Fig. 3.

Figure 40 displays the function $\frac{e^{a(t - \mu^2)}}{(t - \mu^2)^2} \left|\frac{-t}{\mu^2}\right| \sin^2(\delta_o^o - \delta_o^2)$ normalized to the dipion mass spectrum at each incident π^- momentum for those events having a dipion production angle whose cosine is greater

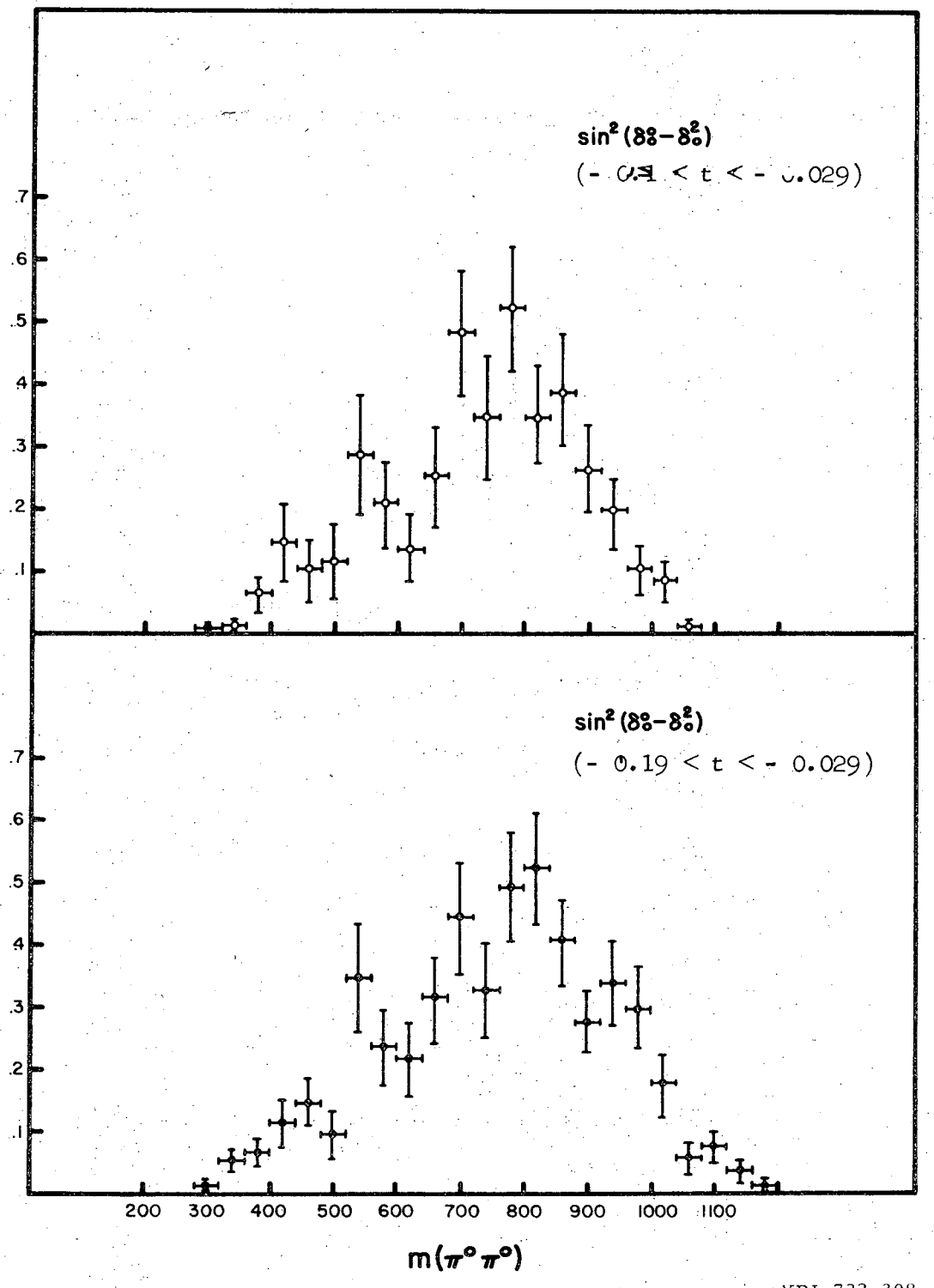

XBL 722-308

Fig. 37. $\sin^2(\delta_0^0 - \delta_0^2)$ as a function of the dipion mass for two different Δt regions.

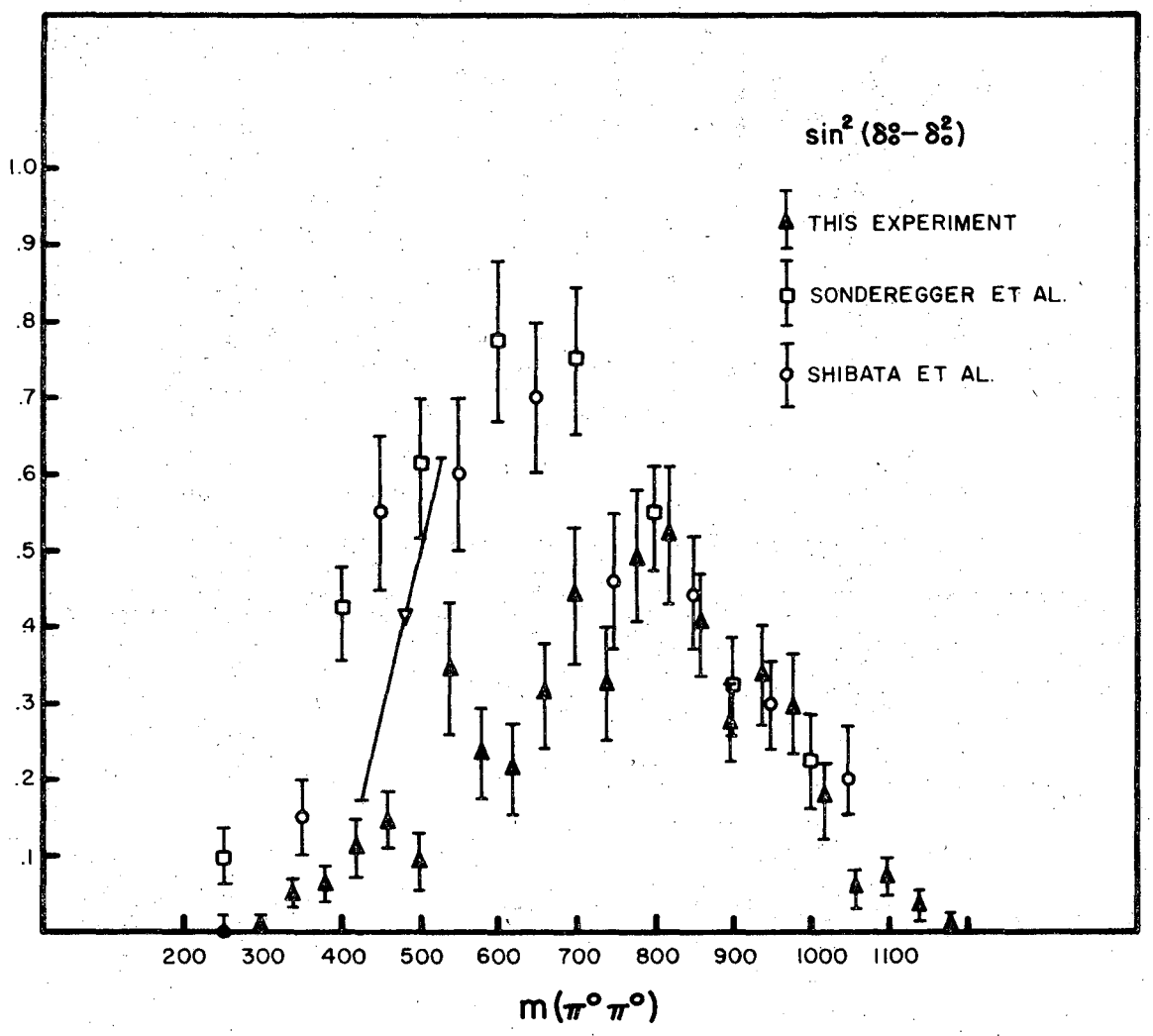

XBL 722-312

Fig. 38. Comparison of $\sin^2(\delta_0^0 - \delta_0^2)$ as obtained in this experiment with other experimental results. (The point with the large error bars at the K mass has been obtained from K^0 decay.)

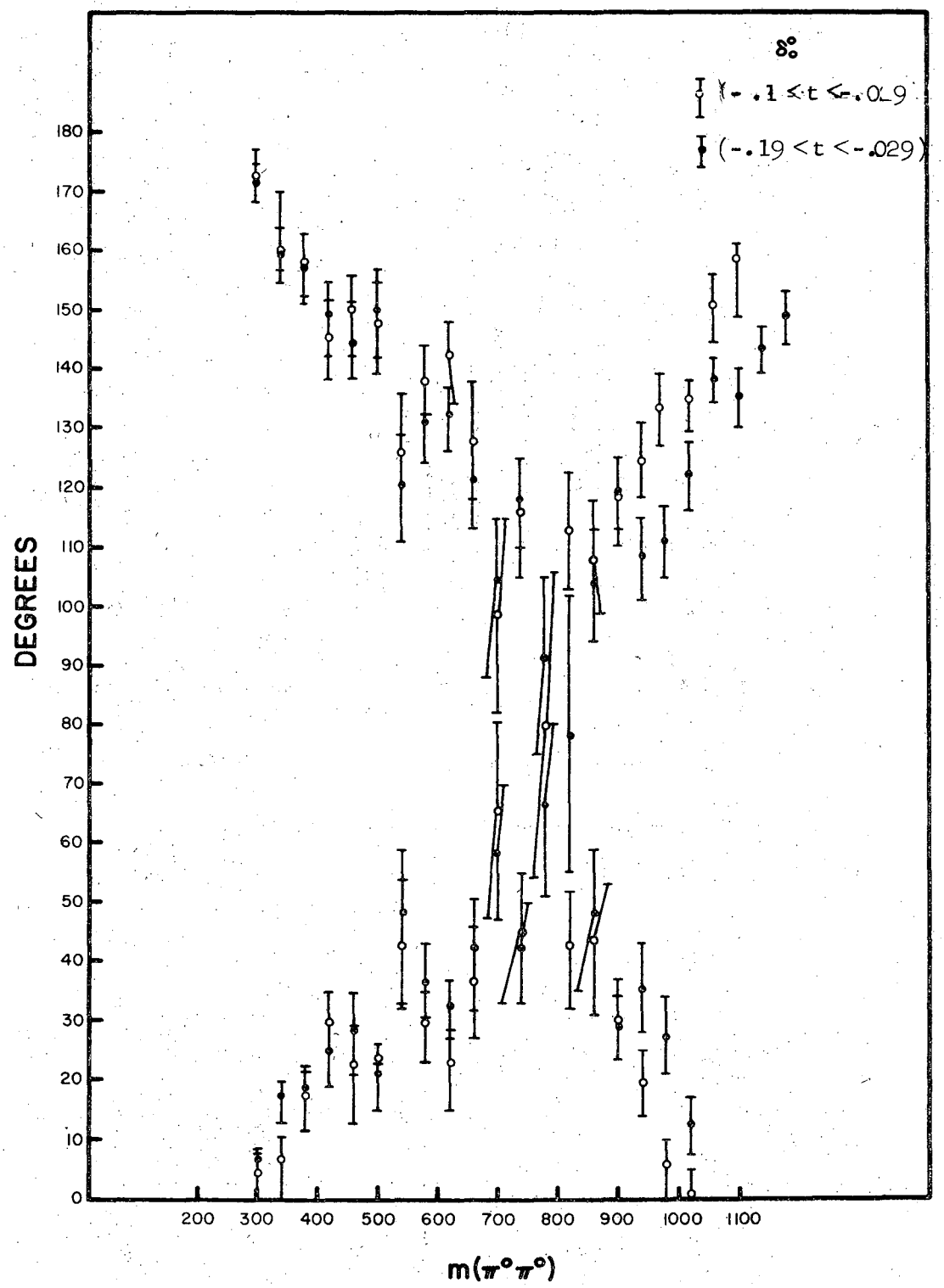

XBL 722-305

Fig. 39. δ_o^o obtained as a function of the dipion mass after scalingt e $\sin^2(\delta_o^o - \delta_o^2)$ of this experiment to the unitarity limit.

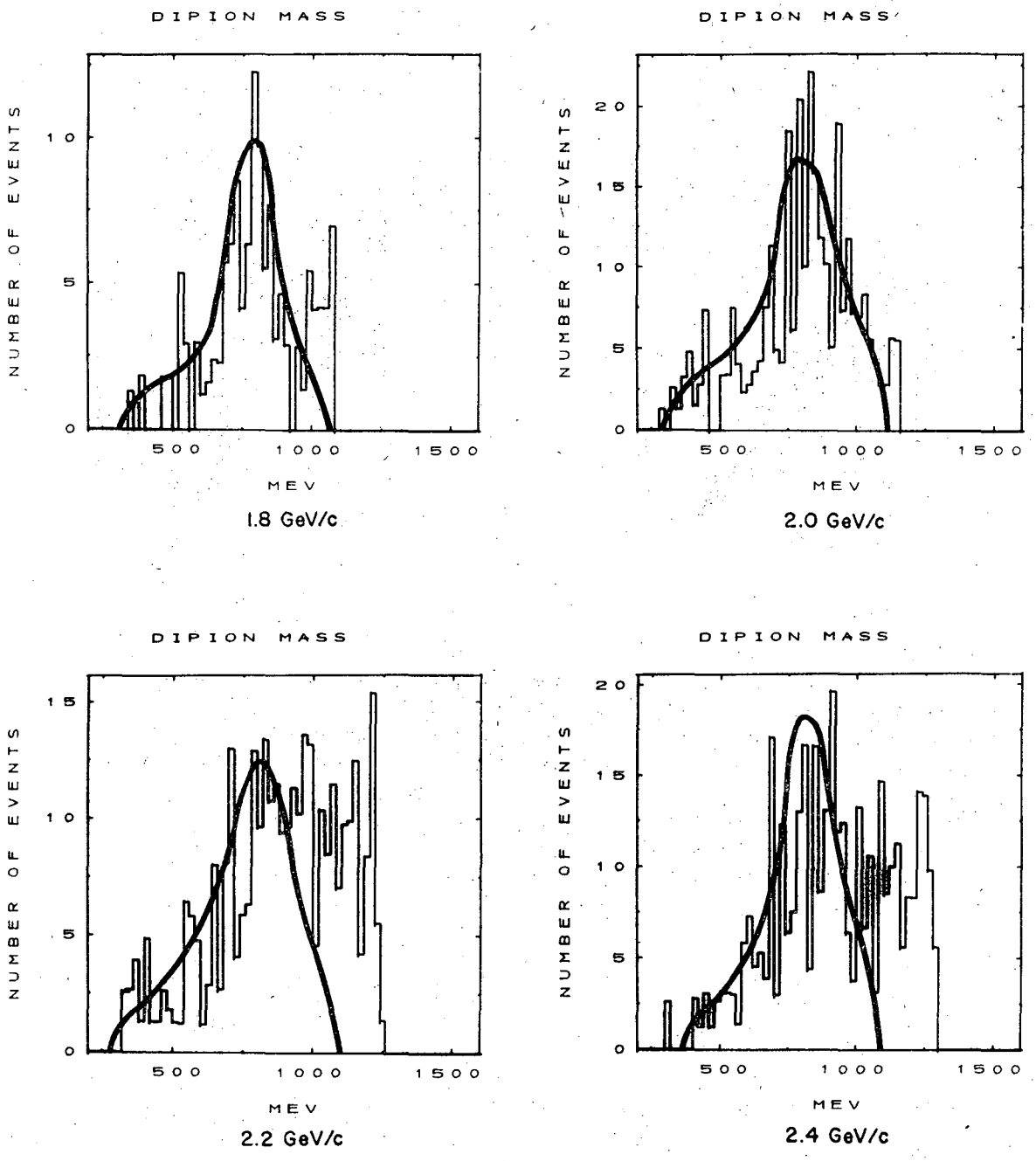

XBL 722-306

Fig. 40. Fits to the dipion mass spectrum (after a $\Delta(1238)$ cut). The data is for those events having a dipion production angle whose cosine is greater than 0.8. The parametrization for the fit was obtained from the calculation in the t region ($-0.19 < t < -0.029$) and then normalized to the appropriate region of the mass distributions. Note that the fit does not include the high mass region since all of these events lie outside the t cut.

Table X. $\sin^2(\delta_o^o - \delta_o^2)$ as a function of $m_{\pi^o\pi^o}$

$m_{\pi^o\pi^o}$	$\sin^2(\delta_o^o - \delta_o^2)$ for $\Delta t = (-1.0, -0.02)$	$\sin^2(\delta_o^o - \delta_o^2$ for $\Delta t = (-1.9, -0.02)$
280	.0059±0.0060	.0093±0.0061
320	.0114±0.0115	.0551±0.0210
360	.0615±0.0320	.0341±0.0242
400	.1463±0.0641	.1152±0.0428
440	.1007±0.0532	.1466±0.0485
480	.1157±0.0562	.0943±0.0361
520	.2858±0.0970	.3416±0.0853
560	.2064±0.0674	.2386±0.0637
600	.1346±0.0560	.2137±0.0605
640	.2562±0.0817	.3120±0.0774
680	.4841±0.1103	.4423±0.0898
720	.3452±0.0877	.3271±0.0704
760	.5229±0.1109	.4978±0.0913
800	.3476±0.0818	.5232±0.0939
840	.3734±0.0864	.4035±0.0755
880	.2617±0.0696	.2627±0.0559
920	.1942±0.0588	.3377±0.0692
960	.1021±0.0377	.2913±0.0635
1000	.0799±0.0361	.1766±0.0472
1040	.0059±0.0064	.0589±0.0225
1080	.0 ±0.0	.0759±0.0288
		.0332±0.0150
		.0127±0.0098

than 0.8. It will be observed that the curves do not extend past 1080 MeV in the dipion mass, since this region lies outside the Δt binning region used to obtain the $\pi\pi$ scattering parameters.

4. The $\Delta(1238)$ Contribution to the Final State

Once the parametrization of the π-π scattering vertex had been obtained for the reaction $\pi^- p \rightarrow \pi^o \pi^o n$, a fit was made, using the maximum likelihood fitting routine OPTIME to all the peripheral data [including the $\Delta(1238)$] band to the square of the matrix element

$$|s|^2 = af_1 + bf_2$$

where

$$f_1 = \frac{1}{\left[\frac{2(m - m_o)}{t}\right]^2 + 1} \qquad f_2 = \frac{e^{a(t - u^2)}}{(t - u^2)^2}\left(\frac{-t}{\mu^2}\right)\sin^2\left(\delta_o^o(s) - \delta_o^2(s)\right)$$

and f_1 was just a Breit-Wigner for the $\Delta(1238)$ of mass 1220 MeV and full width of 130 MeV, while f_2 was the parametrization of the $\pi\pi$ scattering as established in the present experiment. Good fits were obtained and the relative fractions of each process calculated. The partial rates were found for each momentum from the Monte Carlo integration of the fit to the data of $|s|^2$, by considering the integrals

$$s_1 = a \sum f_1 \qquad s_2 = b \sum f_2$$

and from the fractions

$$\alpha = \frac{s_1}{s_1 + s_2} \qquad \beta = \frac{s_2}{2_1 + s_2}$$

The results have been tabulated in Table XI.

Figures 41 and 42 show the results of this fit to the $n\pi^o$ invariant mass distributions and the dipion mass distributions, respectively, both for the peripheral region.

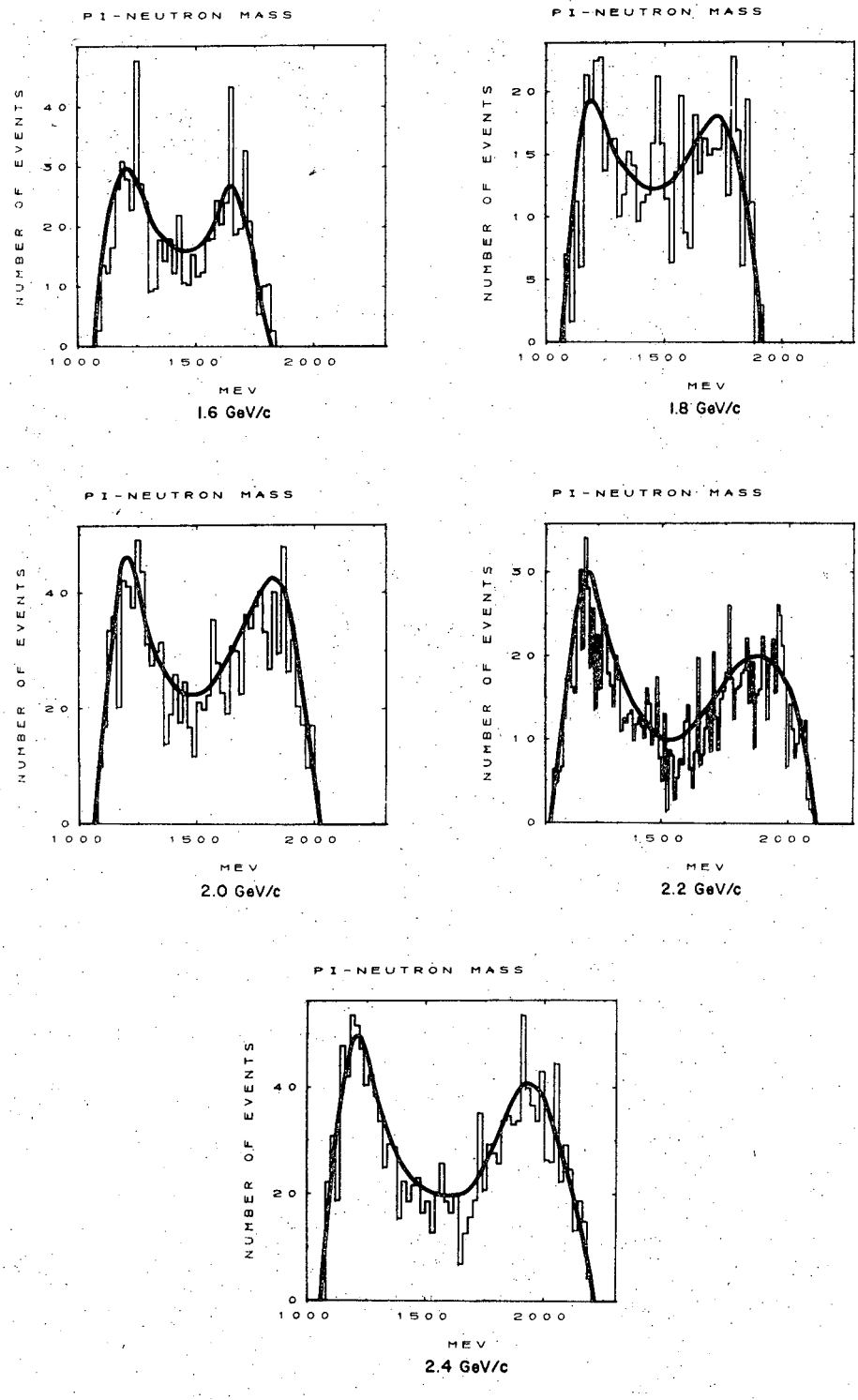

XBL 722-311

Fig. 41. Fits to the ($n\pi^o$) invariant mass spectrum. The data is for those events having a dipion production angle whose cosine is greater than 0.8. The parametrization for the fit was obtained from the calculations in the t region ($-0.19 < t < -0.029$) and then normalized to the appropriate region of the mass distributions.

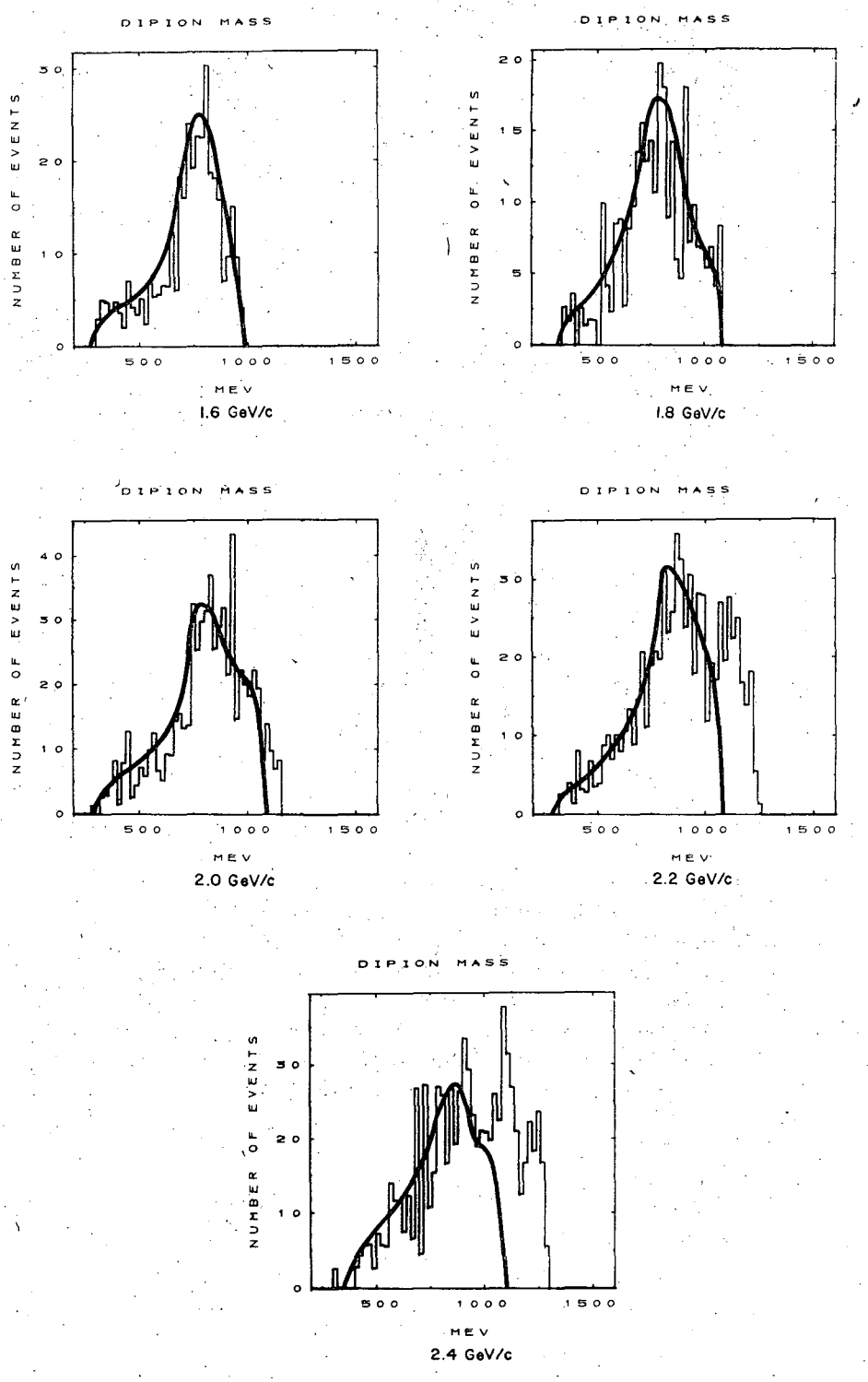

XBL 722-310

Fig. 42. Fits to the dipion mass spectrum. The data is for those events having a dipion production angle whose cosine is greater than 0.8. The parametrization for the fit was obtained from the calculation in the t region $(-0.19 < t < -0.029)$ and then normalized to the appropriate region of the mass distributions. Note that the fit does not include the high mass region since all of those events lie outside the t cut.

Table XI. Fraction of $\Delta(1238)$ produced in $\pi^- p \rightarrow \pi^o \pi^o n$

Momentum (GeV/c)	Fraction of $\Delta(1238)$	Fraction of $(\pi\pi)$
1.6	0.47±0.06	0.53±0.06
1.8	0.42±0.07	0.58±0.07
2.0	0.45±0.04	0.55±0.04
2.2	0.66±0.03	0.34±0.03
2.4	0.62±0.03	0.38±0.03

VI. CONCLUSIONS

The total cross-sections for the reaction $\pi^- p \rightarrow \pi^o \pi^o n$ at incident π^- momenta of 1590, 1790, 1990, 2190, and 2390 MeV/c were found to be 4.38±0.103, 3.82±0.082, 3.60±0.076, 3.22±0.066, 2.76±0.056 mb respectively.

It was found that the dipions were more peripherally produced than indicated by the one pion exchange model and that ~ 50% of the events in the region ($-0.2 < t < -0.029$) were the decay products of the intermediate state $\Delta^o \pi^o$, i.e., $\pi^- p \rightarrow \Delta^o \pi^o \rightarrow n\pi^o\pi^o$. The dipion production distribution was parametrized and a fit obtained for the distribution of the form

$$\frac{|t|}{\mu^2} \quad \frac{e^{a(t - \mu^2)}}{(t - \mu^2)^2} \quad \text{(with } a = 5.68 \pm 1.0\text{)}.$$

Subsequently using the parametrization of the t distribution the off-mass shell matrix element for scattering was calculated. It was found that using this modified one pion exchange model the $\pi\pi$ matrix element did not achieve unitarity. It, however, did exhibit a very rapid fall above 850 MeV and, if interpreted in terms of $\pi\pi$ phase shifts, indicated a rapid variation of the I = 0, J = 0 phase shift in this region. The fact that the solution presented here fell below the unitarity limit may be indicative that the present model for off-mass shell $\pi\pi$ scattering is inadequate to describe the on-mass shell reaction. It may also reflect a possible overall normalization problem in the data, which would alter the absolute value of the square of the matrix element, but not its shape as a function of the $\pi\pi$ mass.

ACKNOWLEDGEMENTS

I would like to thank Professor A. C. Helmholz for serving as the chairman of my dissertation committee, and for the guidance and assistance he has rendered while heading the research group with which I was associated at LBL.

I am especially grateful to Drs. O. I. Dahl, R. W. Kenney, M. Pripstein, and M. Wahlig for their guidance during both the data taking and the data analysis modes of the experiment.

My fellow graduate students Roger Chaffee, Ivan Linscott, Jerry Nelson, and Dr. T. B. Risser also aided and added much to my understanding of the experiment.

Miss Ellen Epstein, and R. Hogrefe did much to organize the scanning and measuring and the extensive production running of the data analysis. I thank them both as well as their staff for their patience.

I would like to thank the Bevatron crew without whose cooperation and help this experiment would not have been done.

Finally, I would like to thank Miss Miriam Machlis for typing this manuscript and Tim Daly who did much of the graphics for it.

This work was done under the auspices of the U. S. Atomic Energy Commission.

1. G. Takeda, Phys. Rev. 100, 440 (1955)

2. W. R. Frazer and J. R. Fulco, Phys. Rev. Letters 2, 365 (1959); 117, 1609 (1960).

3. Y. Nambu, G. F. Chew, M. L. Goldberger and F. E. Low, Phys. Rev. 106, 1337 (1957).

4. D. J. Crennell, V. P. Hough, G. R. Kalbfleisch, K. W. Lai, J. M. Scan, T. G. Schumann, I. O. Skillcorn, R. C. Strand, M. S. Webster, P. Baumel, A. H. Bachmann, and R. M. Lea, Phys. Rev. Letters 18, 323 (1967).

5. W. Selove, V. Hagopian, H. Brody, A. Baker, and E. Leboy, Phys. Rev. Letters 9, 273 (1962); T. T. Veillet, T. Hennessy, H. Bingham, M. Bloch, D. Drijard, A. Laganigue, P. Mittner, A. Rousset, G. Bellini, M. diCorato, E. Fiorini, P. Negri, Phys. Rev. Letters 10 29 (1963).

6. L. T. Gutay, P. B. Johnson, F. S. Loeffler, R. L. McIlwain, D. H. Miller, R. B. Willman, P. L. Csonka, Phys. Rev. Letters 18, 142 (1967); W. D. Walker, J. Carroll, A. Garfinkel, B. Y. Oh, Phys. Rev. Letters 18, 630 (1967); P. E. Schlein, Phys. Rev. Letters 19, 1052 (1967).

7. See references 24 through 29.

8. M. Jacob and O. C. Wick, Ann. of Physics (NY) 7, 404 (1959).

9. G. F. Chew and F. E. Low, Phys. Rev. 113, 1640 (1959).

10. The exposition in this section closely follows that of S. Gasiorowicz Elementary Particle Physics (John Wiley and Sons, New York, 1967) page 453 ff.

11. ibid.

12. R. E. Cutkosky and B. B. Deo, Phys. Rev. 174, 1859 (1968).

13. J. Pisut and M. Roos, Nuclear Phys. B6, 325 (1968); G. Wolf, Phys.

Rev. Letters 19, 925 (1967); J. P. Baton, G. Laurens, and J. Reignier, Phys. Letters 33B, 525 (1970).

14. H. P. Dürr and H. Pilkuhn, Nuovo Cimento XLA, 899 (1965).

15. G. L. Kane and M. Ross, Phys. Rev. 177, 2353 (1969).

16. J. P. Baton, G. Laurens, and J. Reignier, Phys. Letters B25, 419 (1967).

17. J. E. Augustin, J. C. Bizot, J.Buon, J. Haissinski, D. Lalanne, P. Main, H. Nguyen Ngoc, J. Perez-Y-Jorba, F. Rumpf, E.Silva, and S. Tavenier, Phys. Letters 28B, 508 (1969).

18. D. Cline, K. J. Braun, and V. R. Scherer, Nuc. Physics B18, 77 (1970)

19 L. J. Gutay, P. B. Johnson, F. J. Loeffler, R. L. McIlwain, D. H. Miller, R. B. Willman and P. L. Csonka, Phys. Rev. Letters 18, 142 (1967).

20. P. B. Johnson, L. J. Futay, R. L. Eisner, P. R. Klein, R. E. Peters, R. J. Sahni, W. L. Yen, G. W. Tautfest, Phys. Rev. 163, 1947 (1967).

21. E. Malamud and P. E. Schlein, Phys. Rev. Letters 19, 1056 (1967).

22. E. Malamud, P. E. Schlein, T. G. Trippe, D. Brown and G. Gidal, Proc. Inter. Conf. Elementary Particles, Heidelberg, Germany (1967).

23. See, for example, G. Källen, Elementary Particle Physics, (Addison-Wesley, 1964) page 29 ff.

24. E. I.Shibata, D. H. Frisch and M. A. Wahlig, Phys. Rev. Letters 25, 1227 (1970).

25. I. F. Corbett, C. J. S. Damerell, N. Middlemas, D. Newton, A. B. Clegg, W. S. C. Williams, A.S. Carroll, Phys. Rev. 156, 1451 (1967).

26. P. Sonderegger and P. Bonamy, Lund Inter. Conf. on Elementary Particles (June 28 - July 1, 1969)

27. S. Buniatov, E. Zavatini, W. Deinet, H. Müller, D. Schmitt, and H. Staudenaier, Phys. Letters 25B, 560 (1967).

28. M. Feldman, W. Frati, J. Halpern, A. Kanofoky, M. Nussbaum, J. Rickert, P. Yamin, A. Choudry, S. Devons, J. Grunhaus, Phys. Rev. Letters 14, 869 (1965); M. Feldman, W. Frati, R. Gleeson, J. Halpern, M. Nussbaum, and S. Richert, Phys. Rev. Letters 22, 316 (1969).

29. J. R. Bensinger, A. R. Erwin, M. A. Thompson, W. D. Walker, Phys. Letters 36B, 134 (1971).

30. O. I. Dahl, T. B. Day, F. T. Solmitz and N. L. Gould, Group A Programming note No. P-126 (unpublished).

31. P. H. Eberhard and W. O. Koellner, University of California Lawrence Radiation Laboratory Report No. UCRL-20159 (1970); UCRL-20160 (1971).

32. T. B. Risser (Ph. D. Thesis) University of California Lawrence Radiation Laboratory Report UCRL-20039 (1970).

33. T. J. Devlin, University of California Lawrence Radiation Laboratory Report UCRL-9727 (1961) and R. Chaffee (private communication).

34. R. J. Cence, B. D. Jones, V. Z. Peterson, V. J. Stenger, J. Wilson, D. Cheng, R. D. Eandi, R. W. Kenney, I. Linscott, W. P. Oliver, S. Parker, and C. Rey, Phys. Rev. Letters 22, 1210 (1969)

35. C. A. Rey and S. I. Parker, Nucl. Instr. Meth. 54, 314 (1967); 43, 361 (1966).

36. R. J. Kurz, University of California Lawrence Radiation Laboratory Report No. UCRL-11339 (1964).

37. A. R. Clark, L. T. Kerth, Proc. 1966 Inter. Conf. on Instrumentation for High Energy Physics, Stanford, California (1966) page 355.

38. M. Leavitt, LBL Group A programming note P-188 (unpublished).

39. I. Linscott and M. Leavitt (private communication).

40. O. I. Dahl, T. B. Day, F. T. Solmitz, and N. L. Gould, Group A programming note No. P-126 (unpublished).

41. C. O. Gimber, M. Leavitt and R. Chaffee, LBL Group A programming note, No. P-194 (unpublished).

42. P. H. Eberhard and W. O. Koellner, University of California Lawrence Radiation Laboratory Report No. UCRL-20160 (1971).

43. R. Hogrefe, η,N* N$\pi\pi$ Experiment Scanning Instructions (1971) (unpublished).

44. R. Chaffee (private communication).

45. O. I. Dahl and A. Skuja (private communication).

46. F. T. Solmitz, Ann. Rev. Nuc. Sci. 14, 375 (1964)

47. O. I. Dahl (private communication).

48. S. J. Lindenbaum, Ann. Rev. Nuc. Sci. 11, 213 (1961); N. Metropolis, R. Binns, M. Storm, J. M. Miller, G. Friedlander, Phys. Rev. 110, 204 (1958).

49. A. S. Carroll, I. F. Corbett, C. J. S Damerell, N. Middlemas, D. Newton, A. B. Clegg and W. S. C. Williams, Phys. Rev. Letters 16, 288 (1966).

50. H. R. Crouch, Jr., R. Hargraves, R. E. Lanou, Jr., J. T. Massimo, A. E. Pifer, A. M. Shapiro, M. Widgott, A. E. Brenner, M. Ioffredo, F. D. Rudnick, G. Calvelli, F. Gasparini, L. Guerriero, G. A. Salandin, A. Tomasin, C. Voci, F. Waldner, Y. Eisenberg, E. E. Ronat, and S. Toaff, P. Bastien, B. Brabson, B. T. Feld, V. Kistiakowski, Y. Goldschmidt-Clermont, D. Miller, I. A. Pless, A. Rogers, L. Rosenson, L. Ventura, T. L. Watts, and R. K. Yamamoto, Phys. Rev. Letters 21, 845 (1968).

51. G. Bizard, Y. Declais, J. Duchon, J. L. Laville, J. Seguinot, C. Bricman, J. M. Peireau, C. Valladas, Phys. Letters 31B, 481 (1970)

52. M. Feldman, W. Frati, J. Halpern, A. Kankofsky, M. Nussbaum, S. Richert, P. Yanin, A. Choudry, S. Devons and J. Grunhaus, Nuovo Cimento LA 89 (1967).

53. O. I. Dahl, L. M. Hardy, R. I. Hess, J. Kirz, D. H. Miller, and J. A. Schwartz, Phys. Rev. 163, 1430 (1967).

TECHNICAL INFORMATION DIVISION
LAWRENCE BERKELEY LABORATORY
UNIVERSITY OF CALIFORNIA
BERKELEY, CALIFORNIA 94720